

# Development of Earth Abundant $\text{ZnSnN}_2$ for Solar Cell Applications

Vetle Øversjøen



Thesis submitted for the degree of  
Master of Science in  
Materials Science for Energy and Nanotechnology  
60 credits

DEPARTMENT OF CHEMISTRY  
FACULTY OF MATHEMATICS AND NATURAL SCIENCES

UNIVERSITY OF OSLO

Spring 2021

© 2021, Vetle Øversjøen

Development of Earth Abundant  $\text{ZnSnN}_2$  for Solar Cell Applications

<http://www.duo.uio.no/>

Printed: Representralen, University of Oslo

# Abstract

Zn-IV-nitride semiconductors with IV = Si, Ge or Sn, and their alloys constitute a novel and promising group of materials that resemble the already commercially established III-nitrides. The predicted band gaps of the Zn-IV-nitrides and their alloys cover the visible region of the electromagnetic spectrum, making them an earth-abundant alternative to the III-nitride semiconductors. ZnSnN<sub>2</sub> in particular, although relatively unexplored compared to its ZnSiN<sub>2</sub> and ZnGeN<sub>2</sub> counterparts, has a predicted band gap close to the optimal for a top cell in a tandem solar cell structure with Si as a bottom cell. However, a high as-grown carrier density of the stoichiometric ZnSnN<sub>2</sub>, typically  $>10^{20}$  cm<sup>-3</sup>, limits the functionality of the material, and also further complicates the determination of fundamental properties, such as the optical band gap.

In this work, the ZnSnN<sub>2</sub> material has been thoroughly investigated, and different strategies have been applied to control structural, optical and electrical properties. Stoichiometric ZnSnN<sub>2</sub> thin films have been grown on (0002) ZnO substrates by reactive co-sputtering of metallic Zn- and Sn-targets by high-power impulse magnetron sputtering (HiPIMS) and RF magnetron sputtering in a nitrogen atmosphere. Single crystalline hexagonal wurtzite ZnSnN<sub>2</sub> was grown, as evaluated by x-ray diffraction (XRD). The optical band gap was estimated to 1.64 eV - 1.70 eV for stoichiometric ZnSnN<sub>2</sub>, employing transmission and diffuse reflectance measurements. Room temperature Hall effect measurements confirmed carrier densities from  $\sim 3 \times 10^{20}$  cm<sup>-3</sup> to  $\sim 5 \times 10^{20}$  cm<sup>-3</sup>, with affiliated mobilities of  $\sim 12$  cm<sup>2</sup>/(Vs) for all samples, indicating the optical band gap to be affected by a Burstein-Moss shift.

Non-stoichiometric ZnSnN<sub>2</sub> thin films, i.e. Zn-rich ZnSnN<sub>2</sub>, were grown in order to reduce the carrier density due to an effective decrease in Sn<sub>Zn</sub>/Zn<sub>Sn</sub> antisite (intrinsic donor/acceptor) ratio. Indeed, an electron concentration as low as  $1.7 \times 10^{19}$  cm<sup>-3</sup> was achieved, with carrier mobility of 58 cm<sup>2</sup>/(Vs) at room temperature. A systematic reduction in absorption onset was observed following the reduced carrier concentrations, further indicating that the Burstein-Moss effect significantly affects the optical band gap of ZnSnN<sub>2</sub>. However, the increased Zn-content resulted in a degradation of the crystalline quality, and thus the evolution in carrier density, mobility and optical band gap may also have been affected.

Introduction of acceptors, by Li-doping of both stoichiometric and non-stoichiometric ZnSnN<sub>2</sub> during growth, was explored as a potential carrier suppressing strategy. XRD measurements of the doped series revealed a Bragg reflection not observed by any of the

undoped samples discussed in this work, which might suggest a change in growth direction caused by the Li incorporation. Room temperature- and temperature-dependent Hall effect measurements confirmed a carrier reducing effect in the doped films, down to  $5 \times 10^{18} \text{ cm}^{-3}$ . Tauc analysis of transmittance and direct reflectance data yielded an estimated  $E_g \sim 1.6 \text{ eV}$ , also lower than for the undoped stoichiometric samples, which may be attributed to the decrease in carrier concentration.

The growth of stoichiometric, non-stoichiometric and Li-doped  $\text{ZnSnN}_2$  by HiPIMS, show that  $\text{ZnSnN}_2$  can be grown with single-crystalline quality, and the electrical properties of the material can be controlled. As such,  $\text{ZnSnN}_2$  may be developed further to compete with the III-nitrides in solar cell applications.

# Acknowledgments

I would like to offer my warmest thanks to my supervisor, Prof. Lasse Vines, for introducing me to the field of semiconductor physics and for allowing me to work on this project. I will also convey my sincerest gratitude to my co-supervisor, Dr. Vegard S. Olsen, for the countless hours you have invested in me. Whether it be lab training, proof reading, calculations or two-minute discussions at the office, you have always been patient and approachable, and for that I am thoroughly appreciative.

Thank you to Viktor Bobal for ion-implantations, Prof. Lasse Vines and Christoph Seiffert for SIMS measurements, Prof. Augustinas Galeckas for conducting PL- and diffuse reflectance-measurements, and Jon Borgersen for teaching me how to operate the Hall effect-, AFM-, and SEM EDS-equipment at MiNaLab. Your contributions to this work are very much appreciated.

To my fellow students at LENS, these past few years would not have been as much fun without you. Being able to laugh about unexpected results, equipment failure and short deadlines together has been somewhat therapeutic.

I would like to thank my friends and family for all their encouragement and unconditional support throughout my years as a student. Finally, thank you Nanna, for your good advice, patience and understanding these past few months.



# Contents

<b>Abstract</b>	<b>iii</b>
<b>Acknowledgments</b>	<b>v</b>
<b>1 Introduction</b>	<b>1</b>
<b>2 Theory</b>	<b>3</b>
2.1 Crystal Structures . . . . .	3
2.2 Semiconductors . . . . .	5
2.2.1 Electron Energies and Band Structure . . . . .	6
2.2.2 Charge Carriers . . . . .	7
2.3 Thin Film Growth . . . . .	10
2.4 ZnSnN <sub>2</sub> . . . . .	11
2.4.1 Crystal Structure . . . . .	12
2.4.2 Electrical Properties, Defects and Optical Band Gap . . . . .	13
2.4.3 Crystal Quality and its Relation to Solar Cell Applications . . . . .	13
2.5 The pn-Junction . . . . .	14
2.6 Working Principles of Solar Cells . . . . .	16
2.6.1 Tandem Solar Cells . . . . .	17
<b>3 Experimental Methods</b>	<b>19</b>
3.1 Sputter Deposition . . . . .	20
3.1.1 Sputtering . . . . .	20
3.1.2 Sputtering and Plasma Characteristics . . . . .	21
3.1.3 Sputter yield and deposition rate . . . . .	21
3.1.4 RF Sputtering . . . . .	22
3.1.5 Reactive Sputtering . . . . .	22
3.1.6 High-power Impulse Magnetron Sputtering . . . . .	23
3.2 X-Ray Diffraction . . . . .	24
3.2.1 $\theta/2\theta$ Scan . . . . .	25
3.2.2 Rocking Curve Scan . . . . .	26
3.2.3 Phi Scan . . . . .	27
3.3 Hall Effect Measurement . . . . .	28
3.3.1 Hall Effect Theory . . . . .	28
3.3.2 The van der Pauw Method . . . . .	29

---

3.4	SEM EDS . . . . .	31
3.4.1	Energy Dispersive X-Ray Spectroscopy . . . . .	31
3.5	Atomic Force Microscopy . . . . .	32
3.6	UV-VIS Spectrophotometry . . . . .	34
3.6.1	Tauc Analysis . . . . .	35
3.7	Photoluminescence Spectroscopy . . . . .	35
3.8	SIMS . . . . .	36
3.9	Ion-Implantation . . . . .	37
<b>4</b>	<b>Process Development</b>	<b>39</b>
4.1	Reducing Oxygen Incorporation . . . . .	41
4.2	Non-stoichiometric Growth . . . . .	42
4.3	Development of Li-doped ZnSnN <sub>2</sub> . . . . .	43
<b>5</b>	<b>Results and Discussion</b>	<b>45</b>
5.1	Stoichiometric Thin Films . . . . .	45
5.1.1	Structural Analysis of Stoichiometric Films . . . . .	45
5.1.2	Electrical Properties of Stoichiometric Films . . . . .	50
5.1.3	Optical Properties . . . . .	51
5.2	Off-Stoichiometric ZnSnN <sub>2</sub> Growth . . . . .	53
5.2.1	Structural Analysis . . . . .	54
5.2.2	Electrical Properties . . . . .	58
5.2.3	Optical Properties . . . . .	61
5.3	Charge carrier control by Lithium Doping . . . . .	62
5.3.1	SIMS . . . . .	63
5.3.2	Structural Analysis . . . . .	63
5.3.3	Electrical Properties . . . . .	65
5.3.4	Optical Properties . . . . .	67
<b>6</b>	<b>Conclusion</b>	<b>69</b>
	<b>Suggestions for Further Work</b>	<b>70</b>
<b>A</b>	<b>Structural Analysis</b>	<b>75</b>
<b>B</b>	<b>Optical Analysis</b>	<b>77</b>



# Chapter 1

## Introduction

Inexpensive and reliable energy sources have been coveted by society since long before the laws of physics were written down. Early civilizations utilized the kinetic energy of flowing water to mill grains and the chemical energy in firewood for its warmth, oblivious to the rules of fluid- and thermodynamics. Understanding the world around us has allowed us to develop more efficient ways of extracting energy. Traditional energy sources, i.e. coal and natural gas, are non-renewable and lead to increased levels of greenhouse gases (GHG) in the atmosphere. If Norway is to reduce their total GHG emissions by at least 50% within 2030 compared to 1990 emissions, in accordance with the Paris agreement, research and development of renewable energy sources is imperative. Renewable energy is energy extracted from non-depleting energy sources, e.g. solar and wind. To dominate the energy market, however, these renewable sources have to be more inexpensive and reliable than fossil fuels, and they have to be compatible with existing systems and infrastructure. Solar power can be extracted in several ways. Solar thermal energy systems for example, collect the solar energy as heat, which in turn can generate steam for a turbine. Solar cells, on the other hand, make use of the photoelectric effect, the generation of voltage in a material upon exposure from light, in order to convert sunlight to electricity. Reducing the cost of solar cell power can be achieved in different ways. Either by reducing the material cost of the unit itself or by making the solar cells more efficient, producing more energy per unit.

The solar industry of today is dominated by silicon-based solar cells. Consisting of an earth abundant element with a well developed industry and infrastructure, the silicon solar cell is relatively inexpensive to produce, and the technology is becoming commercially mature. The dilemma of silicon solar cells, however, is that they are grossly inefficient, with a theoretical upper limit below 30% efficiency. This implies that 70% of the energy which could have been harvested is not extractable. Tandem solar cells aim to harvest this surplus energy. By implementing an additional solar absorber material on top of the traditional Si cell, one could increase the efficiency significantly. These solar cells exist in today's market, but they are expensive and rely on either toxic materials or elements of low abundance. Thus, there is a need for earth-abundant, inexpensive and non-toxic alternatives to improve on the well-implemented Si solar cell.

A solar cell material, indeed in a tandem cell together with Si, requires electrical and optical properties that are compatible with the Si bottom cell. This includes, for instance, an appropriate band gap energy. A commercially available materials system for optoelectronics and also solar cell applications such as tandem top cells, is the III-nitride system. These materials include AlN, GaN, InN and alloys thereof. GaN is particularly important in optoelectronics such as LED technology. In fact, the discovery of p-type GaN and thus the blue LED, was awarded the 2014 Nobel prize in physics. However, fabrication of III-nitrides is costly, especially compared to that of Si. Recently, II-IV-nitrides, where the group III-cations in III-nitrides are substituted with an equal amount of group-II and group-IV cations, have been proposed as a compromise having optoelectronic properties similar to that of III-nitrides, but at the same time being inexpensive, abundant and non-toxic. Moreover, they can be fabricated employing industrially scalable techniques such as magnetron sputtering.

Within the II-IV-nitrides are the Zn-IV-nitrides, where one of the two cations is Zn and the remaining cation is either Si, Ge or Sn. This material system is relatively unexplored compared to its III-nitride counterparts, and its possibilities and constraints are still under investigation. Especially ZnSnN<sub>2</sub> has uncertainties related to the band gap, crystal quality and donor/acceptor mechanisms of the native material. Thus, the motivation for this work is to explore properties of ZnSnN<sub>2</sub> in the context of solar absorbing material in a tandem solar cell. This includes development of a viable growth process, and an investigation of its charge carrier density and mobility, optical band gap and crystal structure. To better understand the material and methods of this work, an introduction to semiconductor physics and ZnSnN<sub>2</sub> is presented in Chapter 2. This is followed by a presentation, and explanation of, the experimental methods employed in Chapter 3. Chapter 4 covers the extensive process development conducted in this work. The following results are presented in Chapter 5, and discussed consecutively. A conclusion is presented in Chapter 6, followed by a suggestion for further work.

The results presented in this work have contributed to a publication in *Advanced Optical Materials*, by my supervisor Dr. Vegard S. Olsen, in which I am a co-author. The paper is titled *ZnSnN<sub>2</sub> in Real Space and k-Space: Lattice Constants, Dislocation Density, and Optical Band Gap*.

# Chapter 2

## Theory

This chapter aims to explain some core concepts behind the work of this thesis. An introduction to solid materials and how atoms arrange themselves in crystal structures is presented in section 2.1, based on the textbooks of Hemmer [1], Kittel [2] and Tilley [3]. Material specific properties such as band gap and electrical conductivity are determined by the atomic structure of said material. Hence an explanation of the crystal system is imperative for an understanding of how the material behaves, and can be developed for a specific purpose, i.e. tandem solar cells. The succeeding section is an introduction to semiconductor physics. This section is based on the textbooks of Kittel [2], Tilley [3], Griffiths [4] and Streetman [5], and describes the behaviour of semiconductors and why they are such an important group of materials. This section is followed by a segment on the growth of thin films, and a description of different types of thin film growth. Thin film growth is governed by specific conditions such as pressure, temperature and substrate surface mobility, and an understanding of how variations in these parameters influence the finished film, is of importance. The section on thin film growth is based on the textbook of Campbell [6] and Venables [7]. Section 2.4 embodies an overview of  $\text{ZnSnN}_2$ , including structural and electrical properties of the material. Its properties are discussed in relation to the III-nitrides and as a tandem solar cell material. To conclude this chapter, a short introduction to  $pn$ -junctions and solar cells is presented. These sections cover the physics, possibilities and limitations of such components. An understanding of these areas is critical if one is to recognize the importance of this work. The section on  $pn$ -junctions is based on the textbook of Streetman [5], and the section on solar cells is based on the textbooks of Streetman [5] and Campbell [6] and Nelson [8].

### 2.1 Crystal Structures

Atoms in a solid arrange themselves to minimize their free energy, and their placement relative to each other determines the electrical, optical and structural properties of the material. A crystalline solid differs from other solids in that its constituents arrange themselves periodically. This means that there is a fundamental arrangement of atoms that is repeated throughout the solid. The definition of this periodicity can be expressed by *primitive vectors*  $\mathbf{a}$ ,  $\mathbf{b}$  and  $\mathbf{c}$ , constructing an infinite lattice of points. Each point

within this lattice can be represented by a sum of the primitive vectors

$$\mathbf{R} = u\mathbf{a} + v\mathbf{b} + w\mathbf{c} \quad (2.1)$$

where  $u, v, w$  are integers. The volume spanned by these vectors is called the *unit cell* of the crystal, with side lengths  $a, b$  and  $c$ . Depending on the length of  $a, b$  and  $c$ , and the angle between them, seven different crystal systems emerge. A unit cell of lengths  $a = b = c$  with  $90^\circ$  angles between them will be cubic. Examples of variations of the cubic crystal system can be found in figure 2.1. The crystal lattice is not to be confused with the crystal *structure*, which is made up of actual atoms. These seven unit cells give rise to 14 different *Bravais* lattices. Examples of crystal structures exhibited by some important semiconductors are the diamond-like structure of Si, often termed the *Zinc blende* structure, and the wurtzite structure, common for III-nitride semiconductors, i.e. GaN. ZnSnN<sub>2</sub> can grow in an orthorhombic and wurtzite configuration. Thus, potential compatibility with the existing III-nitride based framework is possible.

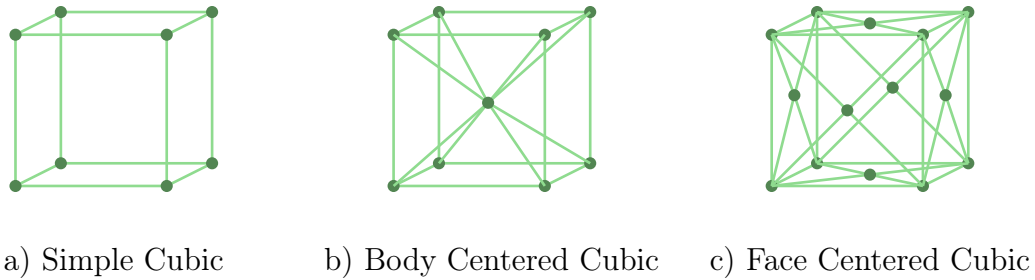


Figure 2.1: The cubic unit cell has three Bravais lattices. a) The primitive cell is the simple cubic (sc). b) The body-centered cubic (bcc) with a lattice point in the middle of the cubic structure. c) The face-centered cubic (fcc) has a lattice point on each face of the cubic structure.

Several material characterization techniques utilize diffraction and scattering processes to analyze the material. As such it is useful to implement a nomenclature to describe the crystal planes in the material. *Miller indices* is such a system, where the indices  $(hkl)$  are a set of parallel planes. These indices represent the reciprocal of the points where the plane intercepts the primitive vectors. As an example, the plane spanned by  $\mathbf{a}$  and  $\mathbf{b}$  in a primitive unit cell will be expressed as  $(1/1, 1/1, 1/\infty) \rightarrow (1, 1, 0)$ , as the plane intercept  $1\mathbf{a}$  and  $1\mathbf{b}$ , but does not intercept  $\mathbf{c}$  at any point. The  $[1, 1, 0]$  vector is perpendicular to the  $(1, 1, 0)$  plane. This nomenclature is used for every crystal structure, except the hexagonal. Planes within hexagonal crystal structures are expressed with *Miller-Bravais* indices in the form  $(hkil)$  and need to satisfy the relation

$$i = -(h + k) \quad (2.2)$$

The atoms in a solid are bound together by strong chemical bonds that can be categorized into three groups; ionic, covalent and metallic bonds. The latter is not considered when discussing semiconductors, while the covalent, ionic, or a mix of the two

bonds are of great interest here. Covalent bonds form as atoms with unpaired electrons interact and said electrons share molecular orbitals. Covalent bonds typically form between identical atoms, or between atoms whose difference in electronegativity is insufficient for electron transfer to occur. If an electron is transferred between the bonding atoms, forming ions, an *ionic* bond occurs. The resulting ions of different polarities are held together by the electrostatic forces between them. Ions are charged atoms where the number of electrons surrounding the nucleus differs slightly from the requirements of charge neutrality. As ions of opposite charge are brought closer to each other, a compromise between the attractive electrostatic forces and repulsive forces due to overlapping electron clouds is met, finding a stable equilibrium.

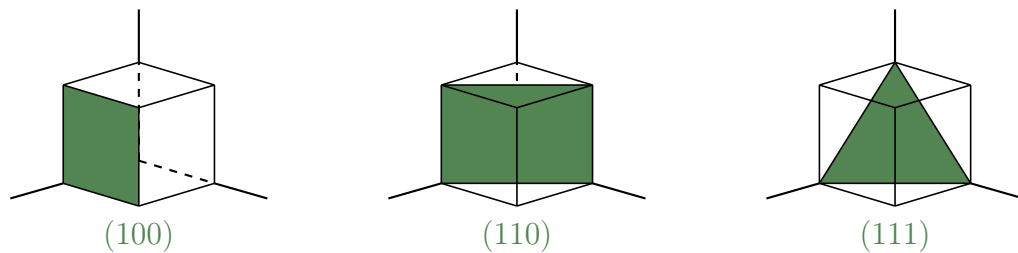


Figure 2.2: Planes named by their respective Miller indices.

## 2.2 Semiconductors

Semiconductors are a class of materials whose electrical conductivity lies between that of a conductor and an insulator. Semiconducting materials can be grouped in two classes, elemental and compound semiconductors (ESC and CSC respectively). ESCs are composed of single species of atoms, found in group IV in the periodic system. Silicon is an example of such a material, possessing semiconducting capabilities in its most elemental form. CSCs however, are materials consisting of different combinations of elements. An example of such a material is GaN, a compound semiconductor composed of a group III and a group V element used in the famous blue LED [9]. The discovery of which awarded Shuji Nakamura, Isamu Akasaki and Hiroshi Amano the 2014 Nobel Prize in Physics. The impact of III-V CSC's has been immense, especially in the IC and optoelectronic industries. Compared to elemental Si, there are no semiconductors that can compete on price and performance, there are some limitations to Si, however. Due to its indirect band gap (the definition of which is defined later in this section), a Si-based LED is not possible. Several CSC's, e.g. ZnO and GaAs have a direct band gap, and are optimal for optoelectronic devices. In addition to this, each CSC has its unique electrical and structural properties, allowing for band gap engineering. An example of this is the III-nitrides, AlN, GaN and InN. Three materials with three distinct band gaps, and consequently, their optoelectronic properties differ. Alloys of these materials, e.g.  $\text{Al}_x\text{Ga}_{1-x}\text{N}$ , have a band gap that varies by the cation ratio, allowing for band gap engineering for specific needs.

### 2.2.1 Electron Energies and Band Structure

As a result of Pauli's exclusion principle, each electron in a single atom has a discrete energy level of which it can occupy. As a large number of atoms ( $\sim 10^{23}$ ) group together to form a solid, the discrete energy levels are so closely spaced that we can consider them as continuous, forming energy bands and a periodic potential within the crystal structure. The electrons can be considered to be *nearly free*, and their interactions are described by the time-independent Schrödinger Equation

$$H\Psi(\mathbf{r}) = \left[ -\frac{\hbar}{2m}\nabla^2 + U(\mathbf{r}) \right] \Psi(\mathbf{r}) = \varepsilon\Psi(\mathbf{r}) \quad (2.3)$$

where  $H$ , the Hamiltonian, is a mathematical operator that describes the energy of the system.  $\Psi(\mathbf{r})$  is the wave function of the electron, and  $\varepsilon$  is the corresponding energy eigenvalue.  $\hbar$  is the reduced Planck's constant and  $m$  is the mass. The potential,  $U(\mathbf{r})$  is periodic and follows

$$U(\mathbf{r}) = U(\mathbf{r} + \mathbf{R}) \quad (2.4)$$

where  $\mathbf{R}$  is a fixed distance derived from the primitive lattice vectors of the atomic crystal.

In some cases, it is expedient to consider the electrons as plane waves that propagate through a lattice of perfect periodicity. In that case, one can express the eigenfunction from equation (2.3) as a Bloch wavefunction on the form

$$\Psi_k(\mathbf{r}) = e^{i\mathbf{k}\mathbf{r}} u_k(\mathbf{r}) \quad (2.5)$$

where the periodicity of the lattice is described by  $u_k(\mathbf{r})$ , and the propagation constant  $\mathbf{k}$  (also called the wavevector) describes how the electron moves through the lattice, and also the energy of the electron (as  $\varepsilon$  is dependent on  $\mathbf{k}$ ). We will also assign a band index to each  $\varepsilon_n$  ( $n=1, 2, 3, \dots$ ), indicating what band the electron occupies. If one is to plot each  $\varepsilon_n$  as a function of  $\mathbf{k}$ , we get a plot of all allowed and forbidden energy states, as shown in figure 2.3.

Energy bands can be separated by forbidden regions where no electron states are found. These regions are called *band gaps* ( $E_g$ ), and the classification of a material as an insulator ( $E_g > \sim 5 \text{ eV}$ ), semiconductor ( $0 < E_g < \sim 5 \text{ eV}$ ) or metal ( $E_g = 0 \text{ eV}$ ) is dependent on the magnitude of this energy gap. The band structure of an intrinsic semiconductor, i.e. where impurities or other defects do not influence the electrical conductivity, is such that no electrons occupy the conduction band at 0K. Its conducting capabilities are in practice that of an insulator because there are no available electrons in the conduction band (or electron-holes in the valence band) that can be accelerated by an electric field. To be conductive, the electrons in the valence band have to be excited, meaning they have to gain additional energy, e.g. from an incoming photon with some energy,  $E_\gamma$ . For the electron to be excited from the valence band to

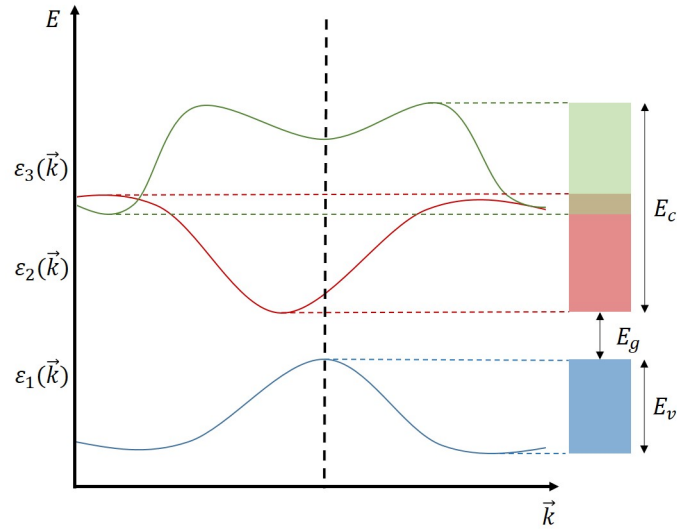


Figure 2.3: Example of a band diagram, where energy eigenvalues  $\varepsilon_n$  are plotted as a function of  $\mathbf{k}$ . Valence and conduction bands are shown in blue and red respectively, as well as the band gap between the two.

the conduction band,  $E_\gamma \geq E_g$ , leaving a missing electron (hole) in the valence band. At temperatures  $> 0\text{K}$ , electrons are excited by the thermal energy of the material, implying that the conductivity of a semiconductor increases with an increase in temperature (up to a certain temperature where phonon scattering effects must be taken into account).

A semiconductor has a *direct* band gap if the valence band maximum (VBM) and conduction band minimum (CBM) are located at the same value of  $\mathbf{k}$ . This means that additional energy  $\geq E_g$  is the only requirement for an electron to be excited from the VBM to the CBM. An *indirect* band gap, however, requires a shift in  $k$  in addition to energy for the electron to be excited. From the relation  $\mathbf{p} = \hbar\mathbf{k}$ , this implies a change in momentum. Only if a quantified lattice vibration, known as a *phonon*, change the momentum of an electron at the same time as said electron gains a sufficient amount of energy, will the electron be excited to the CBM in an indirect semiconductor.

Whether the semiconductor has a direct or indirect band gap is significant in terms of possible applications. Radiative recombination is substantially stronger in direct band gap compared to indirect band gap semiconductors, meaning that direct band gap semiconductors can emit light when excited electrons recombine with holes in the VBM, making them optimal for LEDs and laser diodes.

### 2.2.2 Charge Carriers

As an electron is excited into the conduction band, it leaves a hole treated as a particle of opposite charge in the valence band. This implies that the electron and hole concentrations in an intrinsic semiconductor, i.e. without any defects or dopants, is equal

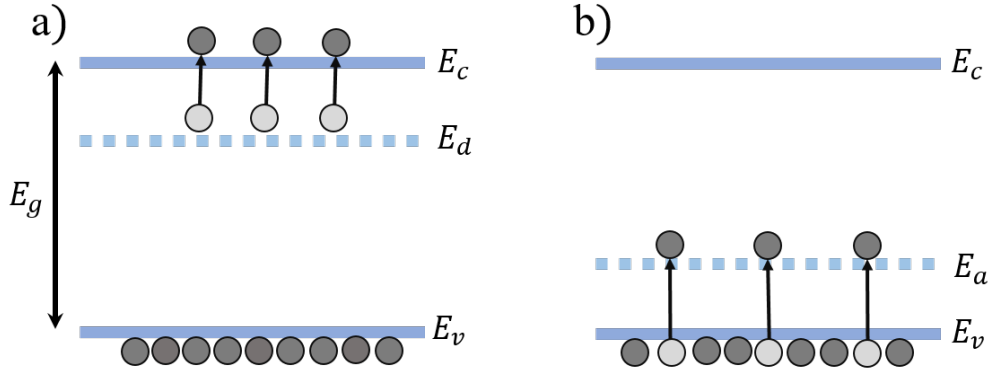


Figure 2.4: Illustration of the introduced energy states and excitation processes in a) a donor doped and b) an acceptor doped semiconductor.

$$n_i = n = p \quad (2.6)$$

An effective way of manipulating the charge carrier density is by introducing elements with excess/a lack of valence electrons in a process called *doping*. Using elemental Si as an example, the number of electrons can be increased by doping the material with an element of higher valency, such as phosphorous (P). The P-atom will bind to four Si-atoms, occupying a Si-site in the lattice. As P has five valence electrons (compared to the four of Si), there is one electron that is not accounted for that occupies a higher energy state than its Si-bound counterparts. In this case, P acts as a *donor*, as the remaining electron is loosely bound and thus can easily be donated to the lattice. Similarly for holes, where boron (B) is of lower valency compared to Si and can therefore accept an electron, leaving behind a hole. By doping a semiconductor, we introduce energy states within the band gap, in principle increasing the likelihood of an electron being excited. A semiconductor that is doped with donor-dopants is called *n-type*, because electrons will be the dominating charge carrier type, whereas an acceptor doped semiconductor is called *p-type*. Note that equation (2.6) is not valid for a doped material, as the introduced electrons or holes will skew the ratio between  $n$  and  $p$  significantly. The charge carrier that dominates the semiconductor is called a majority carrier, leaving the other carrier as the minority carrier.

Electrons in a solid follow Fermi-Dirac statistics, and their distribution over a set of allowed energy states at thermal equilibrium is described by the Fermi-Dirac distribution function

$$f(E) = \frac{1}{1 + e^{(E-E_f)/kT}} \quad (2.7)$$

Where  $E$  is the electron energy,  $E_f$  is the fermi-energy,  $k$  the Boltzmann constant and  $T$  the temperature. This equation maps the probability of an electron occupying an allowed energy state at an absolute temperature,  $T$ . Since the number of thermally excited electrons is equal to the number of thermally generated holes, the probability

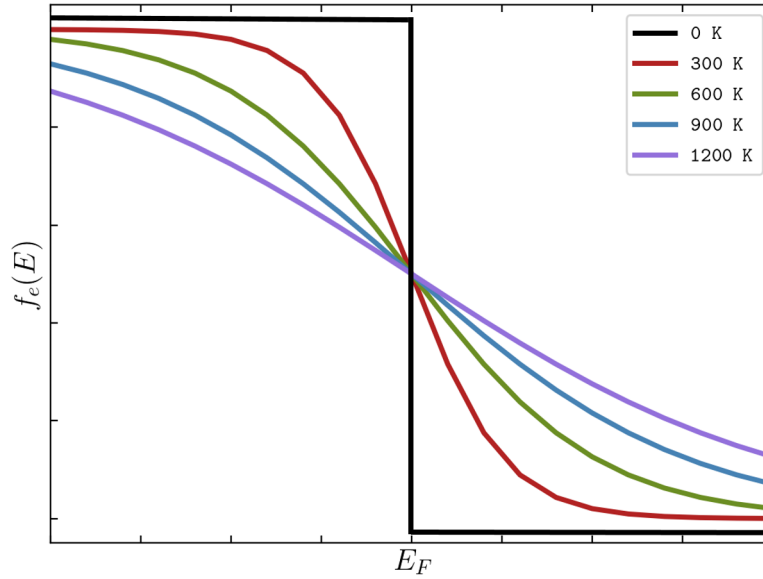


Figure 2.5: The Fermi-Dirac distribution function at different temperatures in steps of 300 K.

of finding a state occupied by a hole is equal to the probability of a state *not* being occupied by an electron. Thus, the hole distribution is given by

$$1 - f(E) = \frac{1}{1 + e^{(E-E_f)/kT}} \quad (2.8)$$

These two expressions depend on the Fermi level,  $E_f$ , of the material.  $E_f$  is defined as the upmost filled energy level at absolute zero temperature and lies halfway between the valence band and the conduction band in an intrinsic semiconductor at absolute zero temperatures. By doping, the Fermi level shifts closer to the conduction- and valence band edges, respectively.

To calculate the carrier concentration, the Fermi-Dirac distribution alone is not sufficient. One would also need to know the number of available states the charge carriers can occupy. More precisely, one needs the density of available states,  $N(E)$ . We find the carrier concentration by integrating the product  $f(E)N(E)$  over a range of energies  $dE$ .

$$n_0 = \int_{E_c}^{\infty} f(E)N(E)dE, \quad p_0 = \int_0^{E_v} [1 - f(E)]N(E)dE \quad (2.9)$$

Integrating from the conduction band,  $E_c$ , to infinity yields the electron concentration, as this is the energy range conducting electrons occupy. Similarly, we integrate from 0 to the valence band edge,  $E_v$ , to find the hole concentration. From equation 2.7, the probability of electrons occupying energies above the conduction band decreases exponentially. This implies that the vast majority of electrons have energies just above

the conduction band edge. The probability of finding holes at low energies decreases exponentially as well, so that the majority of holes lies just below the valence band. In the cases close to the band edges where most of the charge carriers are situated, the Fermi-Dirac distribution function can be approximated

$$f(E_c) \simeq e^{-(E_c-E_f)/kT}, \quad 1 - f(E_v) \simeq e^{-(E_f-E_v)/kT} \quad (2.10)$$

In these regions, the carrier concentrations can be calculated through the effective density of states,  $N_c$  and  $N_v$  for electrons near  $E_c$  and holes near  $E_v$  respectively.

$$N_c = 2 \left( \frac{m_n^* kT}{\hbar^2} \right)^{\frac{3}{2}} \quad (2.11)$$

$$N_v = 2 \left( \frac{m_p^* kT}{\hbar^2} \right)^{\frac{3}{2}} \quad (2.12)$$

Where  $m_n^*$  and  $m_p^*$  are the effective masses of electrons and holes,  $\hbar$  is the reduced Planck constant and  $k$  is the Boltzmann constant. The carrier concentrations are

$$n_0 = N_c f(E_c) = N_c e^{-(E_c-E_f)/kT} \quad (2.13)$$

$$p_0 = N_v f[1 - f(E_v)] = N_v e^{-(E_f-E_v)/kT}$$

The relation  $n_i^2 = n_0 p_0$  is a temperature dependent value, specific for all materials. The Fermi energy of an intrinsic material lies in the middle of the band gap, and the intrinsic carrier concentrations are

$$n_i = N_c e^{-(E_c - \frac{E_g}{2})/kT} \quad (2.14)$$

$$p_i = N_v e^{-(\frac{E_g}{2} - E_v)/kT}$$

By multiplying these two terms, it is clear that the product between  $n_0$  and  $p_0$  does not depend on the Fermi level of the material. This implies that the carrier concentrations in the valence and conduction bands can be expressed by the intrinsic carrier concentration.

$$n_0 p_0 = n_i p_i = N_c e^{-(E_c - \frac{E_g}{2})/kT} N_v e^{-(\frac{E_g}{2} - E_v)/kT} \quad (2.15)$$

$$n_i^2 = n_0 p_0 = N_c N_v e^{-E_g/kT}$$

This is an expression that is valid for doped and undoped materials.

## 2.3 Thin Film Growth

Thin films are layers of material ranging from a single monolayer of atoms up to microns in thickness. The synthesis of thin films is often referred to as depositions, and several

chemical and physical processes can be used. Sputtering, Atomic Layer Deposition (ALD) and Metalorganic Chemical Vapour Deposition (MOCVD) are all examples of thin film deposition processes suitable for different applications. Sputtering is a purely physical process, in which the sputtered species adhere to the substrate directly. In contrast, ALD and MOCVD are chemical processes, in which a series of chemical reactions take place on the substrate surface before a layer forms. Solids can form in three different ways. i) The *single crystalline* formation is the growth of a single crystal. These crystals are highly ordered structures and require great control of growth parameters to form. ii) *Polycrystalline* solids are formed when smaller crystallites grow together. These crystallites can be oriented in all directions, creating grain boundaries as they merge. iii) Amorphous solids are materials that lack the long-range order that characterizes crystals.

Epitaxial growth is the process where a film is deposited on top of a chosen substrate, and the growing film uses the substrate's crystal structure as a template for further growth. Even though the crystal structure is the same, there might be large differences in lattice constants e.g. in *ZnO* and *Al<sub>2</sub>O<sub>3</sub>* that both share the hexagonal wurtzite crystal structure. The degree to which these parameters resemble each other is termed *lattice mismatch*, and is often presented as a percentage calculated from the ratio of the lattice parameters of the two materials. The degree of lattice mismatch between the substrate and thin film can strongly affect the properties of the final material. Lattice mismatch leads to *strain* in the deposited material, causing extended defects in the crystal structure. There are three growth modes we consider when discussing epitaxial growth. i) The *Frank van der Merwe* mode, commonly referred to as the layer-by-layer growth mode. In this case, the deposited atoms are more attracted to the substrate than to each other. The second growth mode is the ii) *Volmer-Weber* mode, and is often called the island growth mode. In this case, "islands" of adatoms forms on top of the substrate. This growth mode occurs when there is a large lattice mismatch and the surface energy is high, as in the adatoms are more likely to bind to each other than to the substrate. iii) The *Stranski-Krastanov* mode is a combination of the previous two modes. Referred to as the layer-plus-island growth mode, the Stranski-Krastanov growth mode is preferred when the surface energy is low, but the lattice mismatch is large.

## 2.4 ZnSnN<sub>2</sub>

The III-nitride compound semiconductors have been vastly influential in the development of optoelectronic devices. UV-lasers, high brightness LED displays and high-power electronics are all examples of technologies enabled by III-nitride semiconductors. Their properties imply they are suitable for solar absorbing applications, as their band gaps range from the infrared to the ultraviolet part of the electromagnetic spectrum [10]. Thus, a stacked arrangement of their alloys allows the harvest of a significant amount of the solar energy. However, the III-nitrides have limitations related to cost

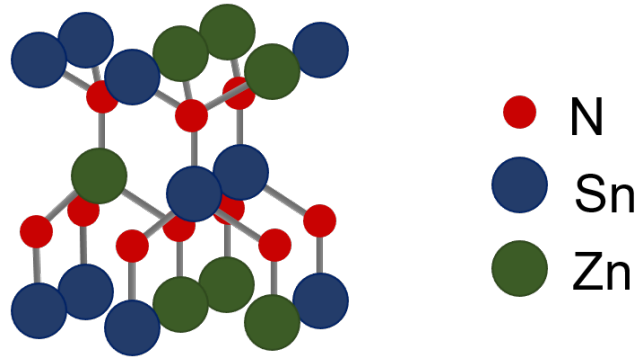


Figure 2.6: Illustration of the hexagonal wurtzite crystal structure of  $\text{ZnSnN}_2$ , adapted from Lahourcade *et al.* [11].

and large-scale production, a significant obstacle if they are to compete in the solar energy market.

$\text{ZnSnN}_2$  is a compound semiconductor that belongs to a class of materials termed II-IV-nitrides. The II-IV-nitrides consist of two cations from group II and IV respectively, along with two nitrogen atoms. The Zn-IV-nitrides, where the group-II-cation is Zn, and IV is Si, Ge or Sn, is of particular interest, since their band gaps match those of the III-nitrides closely, i.e. AlN, GaN and InN [10]. In other words, they are an earth-abundant alternative to the III-nitrides and hence interesting for solar cell applications and optoelectronics.

### 2.4.1 Crystal Structure

$\text{ZnSnN}_2$  has three experimentally confirmed crystal structures; a monoclinic structure, the orthorhombic  $\text{Pna}2_1$  configuration and a hexagonal wurtzite structure with space group  $\text{P}6_3\text{mc}$  [11, 12, 13, 14]. First principle calculations estimate that a second orthorhombic structure with space group  $\text{Pmc}2_1$  is the most energetically favourable [11], but this configuration has to present not been observed experimentally. The orthorhombic  $\text{Pna}2_1$  structure on the other hand, has the lattice parameters  $a = 0.6721$  nm,  $b = 0.5842$  nm,  $c = 0.5459$  nm [11]. Wurtzite  $\text{ZnSnN}_2$  has previously been grown on ZnO substrates through magnetron sputtering demonstrated by Gogova *et al.* [15], and on ZnO buffer layers by Le *et al.* employing plasma-assisted molecular beam epitaxy (PAMBE) [13]. The lattice constants of wurtzite  $\text{ZnSnN}_2$ , the structure of which is illustrated in figure 2.6, have until recently been a topic of discussion, estimated from XRD peak positions of films of varying quality. Single crystalline  $\text{ZnSnN}_2$  thin films was grown heteroepitaxially on (0002) ZnO substrates by Olsen *et al.* [14] allowing for more precise measurement. The reported lattice constants were determined to  $a = 0.346$  nm and  $c = 0.554$  nm, as measured by XRD and transmission electron microscopy (TEM).

### 2.4.2 Electrical Properties, Defects and Optical Band Gap

ZnSnN<sub>2</sub> is an *n*-type material. Its as-grown stoichiometric carrier concentrations are typically in the vicinity of  $n \approx 10^{20} \text{cm}^{-3}$ , resulting in a degenerate behaviour [16]. Although the defects causing this *n*-type behaviour is not yet fully understood, theoretical calculations employing density functional theory (DFT) have predicted a list of possible candidates. The cation antisite Sn<sub>Zn</sub> is calculated to have the lowest formation energy, i.e., has the highest probability of formation. This antisite acts as a double donor in ZnSnN<sub>2</sub>, and can therefore be a significant contributor to the degenerate nature of the as-grown material [17, 18]. The opposite antisite, namely the Zn<sub>Sn</sub> defect, acts as an acceptor, but significantly higher formation energy prevents an equal formation of antisites [17, 18]. Other potential donors, possibly contributing to the high as-grown carrier concentration, are the Zn<sub>i</sub>, as well as the nitrogen vacancy V<sub>N</sub> [16]. These defects on the other hand, have higher formation energies compared to the Sn<sub>Zn</sub> antisite, and are therefore not predicted to be the main contributors [17, 18]. In addition, extrinsic defects incorporated during growth, such as oxygen substituting for nitrogen, O<sub>N</sub>, or interstitial hydrogen, H<sub>i</sub>, also acts as donors in nitrides in general, specifically in ZnSnN<sub>2</sub> [17, 18]. It is therefore likely to be present in any grown material.

The band structure of hexagonal ZnSnN<sub>2</sub> has been modeled through density functional theory (DFT) calculations. The direct band gap of ZnSnN<sub>2</sub> is formed from the N 2p, Zn 3d and Sn 5d orbitals constituting the valence band, and the conduction band contributions are from the Sn 5s and N 2s and 2p orbitals [17]. There is a large span in calculated band gap energies, however. Depending on crystal structure and cation-disorder, calculated  $E_g$  ranges from 0.35 eV to 2.67 eV [10, 19, 20]. Observations from experiments reinforce these findings as the optical band gap vary with crystal structure as well as the carrier concentration due to the Burstein-Moss shift [21, 22], which is the phenomenon where the optical band gap of a material is increased due to electrons occupying a significant amount of states in the conduction band. Therefore, the band gap energy of ZnSnN<sub>2</sub> depends on the cation sub-lattice ordering of the material, complicating the experimental band gap determination [12, 23, 24].

### 2.4.3 Crystal Quality and its Relation to Solar Cell Applications

ZnSnN<sub>2</sub> is a relatively unexplored material in the realm of Zn-IV-nitride semiconductors compared to its Si and Ge counterparts, and its most fundamental properties are still under investigation. The large variations in reported band gap energies is an example of this. To gain an increased understanding of the material and its fundamental properties, which is imperative for further material analysis and device fabrication, single crystalline growth of ZnSnN<sub>2</sub> on a lattice-matched substrate, e.g ZnO, is desirable. Lattice parameters of  $a = b = 0.3250 \text{ nm}$  and  $c = 0.5207 \text{ nm}$  for ZnO [25] compared to the lattice parameters of  $a = b = 0.346 \text{ nm}$  and  $c = 0.554 \text{ nm}$  for ZnSnN<sub>2</sub> [14], amounts to a lattice mismatch of about 4.17%. Although this is relatively high for epitaxial layers, it is rather small compared to GaN grown epitaxially on *c*-Al<sub>2</sub>O<sub>3</sub>, which has a lattice

mismatch of  $\sim 15\%$  [26]. This, along with its wurtzite crystal structure makes ZnO a prime candidate as a substrate for growth optimization. ZnO is also n-type, however, and won't be suitable in forming a heterojunction.

## 2.5 The pn-Junction

Most of the semiconducting devices made today rely on *pn*-junctions to operate. These junctions are instrumental in rectification, amplification and switching operations. A *pn*-junction is the interface between a *p*-type and an *n*-type material when brought together, illustrated in Figure 2.7, the purpose of which is to control the recombination of electron-hole-pairs (EHP).

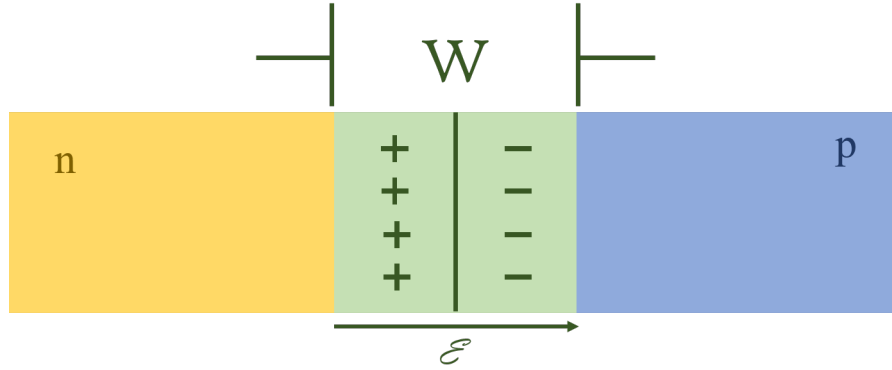


Figure 2.7: Schematic of a *pn*-junction. The yellow and blue areas are *n*- and *p*-type respectively. The depletion zone, *W*, is shown in green, the electrical field  $\mathcal{E}$  goes from the *n*-type to the *p*-type material.

While the concentration of electrons is high in *n*-type material and low in *p*-type material, conversely the hole concentration is high in *p*-type material and low in *n*-type material. This leads to a concentration gradient between the two, and charge carriers will diffuse from one region to the other, leaving uncompensated ionized donors and acceptors behind. This leads to a build-up of charge in the area around the interface, termed the *depletion region* (*W*). With these charge differences comes an electrical field,  $\mathcal{E}$ , spanning the width of *W*. At last, the diffusion and  $\mathcal{E}$  will come to an equilibrium, hindering further diffusion. At equilibrium, the current density through the component is zero as the diffusion current is counteracted by the drift current generated by the electrical field. The electron- and hole-current density can be expressed with the two terms shown in equation (2.16)

$$J_n(x) = q \left[ \mu_n n(x) \mathcal{E}(x) - D_n \frac{\partial}{\partial x} n(x) \right], \quad J_p(x) = q \left[ \mu_p p(x) \mathcal{E}(x) - D_p \frac{\partial}{\partial x} p(x) \right] \quad (2.16)$$

Where *J* is the current density of electrons or holes,  $\mu$  is the charge carrier mobility, *p/n* is the charge carrier concentration, *D* is the diffusion constant for electrons or holes.

The introduction of electrons and holes through doping shifts the Fermi level closer to the conduction and valence band. The Fermi level of a semiconductor in equilibrium is also always constant and continuous. To meet this requirement, the energy bands are bent within the depletion region, as shown in figure 2.8. The difference between the energy bands acts as a potential barrier for the charge carriers, termed the *built-in potential*,  $V_{bi}$ .

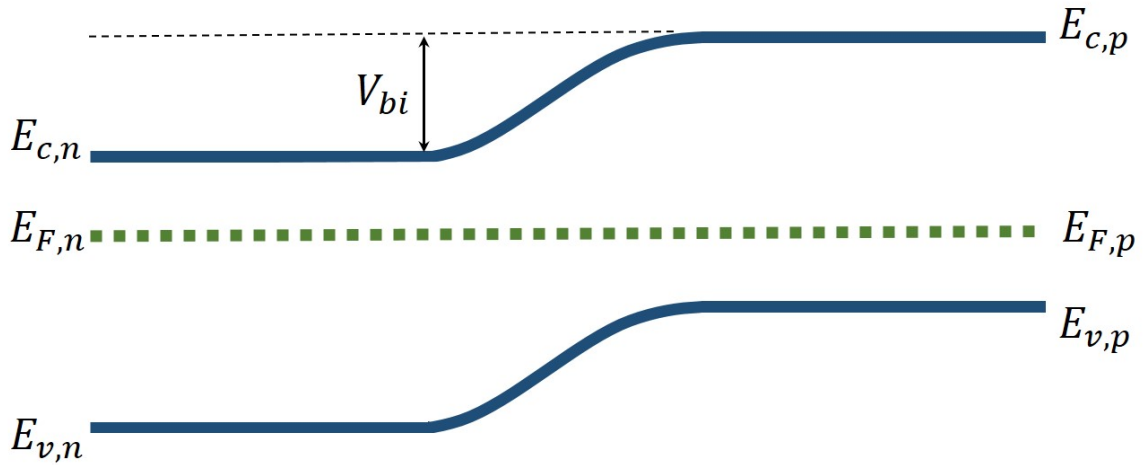


Figure 2.8: Diagram showing the alignment of the band structure between a donor doped (subscript  $n$ ) and acceptor doped (subscript  $p$ ) material. Notice how the Fermi level,  $E_F$ , is constant throughout the structure.

For an excited electron in the conduction band to overcome this barrier, it needs additional energy equivalent to the potential,  $qV_{bi}$ . The built-in potential is dependent on the band gap of the material, as well as the doping concentrations. By applying a voltage over the junction, the energy bands will shift relative to each other, altering the built-in voltage in the process. By applying a forward-biased voltage ( $V = V_f$ ) the barrier decrease, increasing the chance of a charge carrier overcoming the barrier. A reverse bias ( $V = -V_f$ ) has the opposite effect where it increases the potential barrier. This feature makes a pn-junction rectifying because the current only flows in one direction when the applied voltage is forward biased.

$$V_{bi} = \frac{k_B T}{q} \ln \frac{N_d N_a}{n_i^2} \quad (2.17)$$

Equation (2.17) shows the relation of doping concentrations and  $V_{bi}$ .  $N_d$  and  $N_a$  is the concentration of donors in the n-type material and acceptors in the p-type material, respectively.

## 2.6 Working Principles of Solar Cells

Solar cells are devices that convert electromagnetic energy in the form of sunlight directly into electric energy. The sun emits light in a wide range of energies over the electromagnetic spectrum, the energy of which is determined by the wavelength ( $\lambda$ ). A solar cell absorbs the energy of the sunlight in an excitation process and separates the charge carriers before they are transported to an external circuit where they can do work on a load. The light absorption and charge carrier separation processes are both heavily dependent on the band gap of the solar cell material, and band gap engineering is therefore instrumental in solar cell manufacturing. The vast majority of the solar cells on today's market are made from crystalline silicon. With a band gap of 1.2 eV, silicon is well suited as a solar cell material because of its abundance and non-toxic properties.

A solar cell is built like a pn-junction, and works as a two terminal device. This means that it has the rectifying properties of a diode in the dark and photovoltaic (PV) properties when illuminated. As a photon with energy  $E \geq E_g$  enters the material, it can excite an electron in the valence band into the conduction band. This leads to a build up of minority carrier concentration, and the minority carriers diffuse into the depletion region, where they are accelerated across the junction by the electric field  $\mathcal{E}$ . The following current density in the cell can be expressed as

$$J(V) = J_{sc} - J_{dark}(V) = J_{sc} - J_0 \left( e^{\frac{qV}{k_B T}} - 1 \right) \quad (2.18)$$

where  $J_{dark}$  is the dark current density of an ideal diode,  $J_0$  is a constant and  $J_{sc}$  is the short circuit current density. Note that the sign convention of voltage and current in photovoltaics is opposite to the usual conventions for electronic devices so that the photocurrent is positive.  $J_{dark}$  is generated when a load is present and a potential difference develops between the terminals of the cells.  $J_{dark}$  flows opposite to the direction of the photocurrent, and reduces the net current of the cell. The *open circuit voltage*,  $V_{oc}$ , has its peak when  $J_{sc} = J_{dark}$ , from equation 2.18 this equates to

$$V_{oc} = \frac{k_B T}{q} \ln \left( \frac{J_{sc}}{J_0} + 1 \right) \quad (2.19)$$

The power delivered by the solar cell is defined as the product between the operating voltage and the associated current

$$P_{cell} = J_m V_m \quad (2.20)$$

The operating efficiency is defined as the ratio between  $P_{cell}$  and the incident light power density,  $P_{sun}$

$$\eta = \frac{P_{cell}}{P_{sun}} = \frac{J_m V_m}{P_{sun}} \quad (2.21)$$

Another important relation is that of the *fill factor* ( $FF$ ).  $FF$  is a measure of the 'squareness' of the J-V curve and is a figure of merit for solar cell design. The fill factor is defined as

$$FF = \frac{J_m V_m}{J_{sc} V_{oc}} \quad (2.22)$$

The fill factor and efficiency are directly related through the maximum power output,  $P_{cell}$ .

$$\eta = \frac{J_{sc} V_{oc} FF}{P_{sun}} \quad (2.23)$$

Despite the suitable band gap of silicon, a significant share of the incident radiation is not converted to electricity. About 20% of the light that enters the solar cell has insufficient energy to excite charge carriers from the valence band to the conduction band [27], and photons with energies  $E_\gamma > E_g$  will excite electrons above the conduction band, and the excess energy is dissipated through the crystal as heat.

### 2.6.1 Tandem Solar Cells

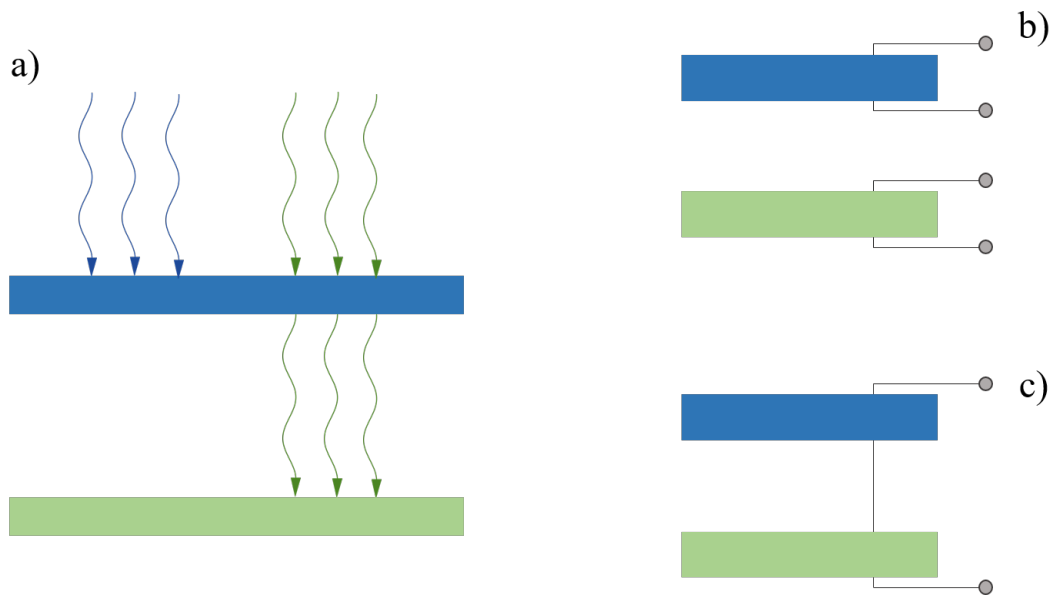


Figure 2.9: a) Working principle of TSCs, high energy light (blue) is absorbed at the top layer, letting low energy light (green) pass through to be absorbed by the narrow band gap material. b) Schematic of a four-terminal tandem cell, c) schematic of a two-terminal tandem cell.

The basic principle of tandem solar cells (TSCs), as schematically illustrated in figure 2.9 (a), is to stack materials with different band gaps on top of each other, making a solar cell with a wider absorption spectrum. A wide band gap material as the top cell will absorb the higher energy photons (blue layer in figure 2.9 (a)), transmitting the lower energy photons to be absorbed by the narrow band gap material underneath. TSCs have a higher theoretical efficiency limit and have lower thermal losses than conventional single junction solar cells. There are two methods to connect the different cells, illustrated in figure 2.9b-c. The most efficient of the two is the four-terminal

design (figure 2.9 (b)) where both junctions are connected with independent connections, the efficiency of which would be the sum of the two. The number of fabrication steps associated with such a design is significant, however, and large scale commercialization seems unlikely at this point. The two-terminal design (figure 2.9 (c)) is the most elegant of the two, connecting the different cells in series. A drawback of this configuration is that the total generated current of such a device would be constrained to the lowest-performing cell. With the widespread use of silicon based solar cells, a natural development to increase the efficiency further would be a Tandem solar cell with Si as the bottom cell. The main challenge then for material scientists would be the top layer. A top-layer material will have to be transparent to light of longer wavelengths, have high carrier mobility and suitable carrier concentrations. Apart from the physical requirements of the material, one would prefer its constituents to be earth-abundant, cheap, non-toxic and suitable for large-scale production.

# Chapter 3

## Experimental Methods

This chapter covers the experimental methods employed in this work. Section 3.1 covers different sputtering techniques, i.e. DC, RF and HiPIMS, used to deposit the  $\text{ZnSnN}_2$  thin films. An explanation of reactive co-sputtering aims to explain how this technique is utilized to alter the stoichiometry of the films. Working principles, possibilities and limitations are discussed. Section 3.1 is based on the textbooks of Campbell [6] and Lundin [28]. The subsequent section is an introduction to X-ray diffraction (XRD), a characterization technique employed to investigate the structural properties of the  $\text{ZnSnN}_2$  films. The section aims to clarify the difference between different scans performed in this work, and the information one can gather from such scans. Section 3.2 is based on the textbooks of Tilley [3] and Kittel [2]. Hall effect theory and Hall effect measurements are covered in section 3.3, employed in this work to characterize the electrical properties of the deposited  $\text{ZnSnN}_2$ . The van der Pauw method and temperature-dependent Hall measurements are described. Section 3.3 is based on the textbook of Streetman and Banerjee [5]. Section 3.4 is an introduction to Scanning electron microscopy with energy dispersive spectroscopy (SEM EDS), working principles, possibilities and limitations. SEM EDS is used in this work for compositional analysis of the deposited films, as well as investigation of the sample surface. This section is based on the textbook of Goldstein [29]. Following is a description of atomic force microscopy (AFM) based on the textbook of Rogers, Adams and Pennathur [30]. AFM is employed to investigate the topographical properties of the deposited films. The section includes a description of the tuning fork and beam bounce configurations, and their differences. The succeeding section 3.6, is an introduction to UV-VIS spectrophotometry. A technique employed to investigate the transmittance and reflectance of  $\text{ZnSnN}_2$ , and how this data can be interpreted through Tauc analysis. Section 3.7 is based on a review article of Gilliland [31], and covers Photoluminescence Spectroscopy (PL) and its relation to this work. The following section covers secondary ion mass spectrometry (SIMS), employed to measure trace elements, i.e. Li and O, in the grown films. The concluding section, section 3.9, is a description of ion-implantation and an explanation as to how this technique allows us to alter the properties of the substrate.

## 3.1 Sputter Deposition

Sputtering is a well-established thin film deposition technique, widely used in large-scale thin film industry, that utilizes bombardment of a target material with an incident beam of plasma ions. The incident ions sputter off target atoms and molecules, that are ejected in the direction of a substrate. The target materials can be elemental or compounds, and one can introduce reactive gases in the sputtering chamber to implement non-solid elements. By tuning the kinetic energy of the incident bombardment particles, the sputtering rate can be altered, allowing for high control of the composition, crystalline quality and morphology of the complete film.

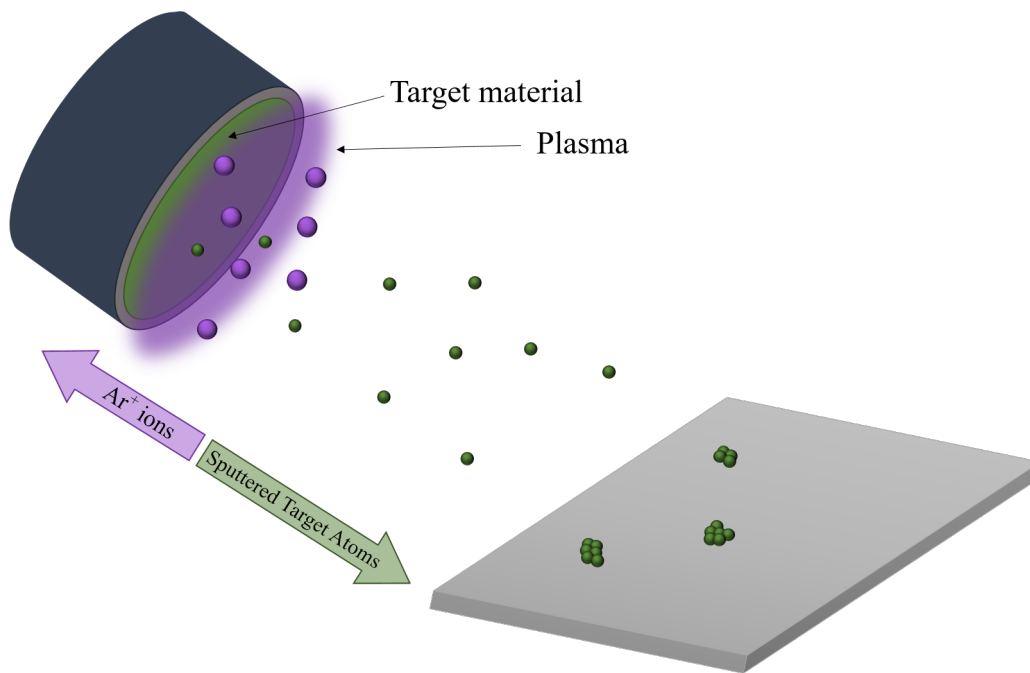


Figure 3.1: Schematics of a sputtering process involving  $\text{Ar}^+$ -ions bombarding the target material, resulting in the ejection of sputtered species in the direction of the substrate. Figure adapted from Olsen [32].

### 3.1.1 Sputtering

The sputtering process is based on a plasma formed by an inert gas, typically Ar, passed between two electrodes. The target material is placed on to a cathode surrounded by a shield that acts as the anode. An applied voltage between these two terminals will ionize the inert gas within the low pressure deposition chamber, forming a plasma in front of the target material. the positively charged  $\text{Ar}^+$ -ions are accelerated by the applied voltage towards the negatively charged cathode, bombarding the target as illustrated in Figure 3.1.

Since the plasma is electrically charged by definition, it can be confined using electromagnetic fields generated by a magnet, typically located behind the target, in a process

termed *magnetron sputtering*. The Lorenz force ( $\vec{F}_L$ ) exerted on each charged species by the magnetic field is defined as

$$\vec{F}_L = q\vec{v} \times \vec{B} \quad (3.1)$$

where  $q$  is the electric charge and  $\vec{v}$  the velocity vector of the charged species, and  $\vec{B}$  is the magnetic field vector.  $\vec{F}_L$  will have a direction perpendicular to  $\vec{v}$  and  $\vec{B}$ , causing the species to travel in a helical motion with radius

$$r = \frac{mv}{qB} \quad (3.2)$$

where  $m$  is the mass,  $v$  the velocity,  $q$  the charge of the charged species respectively, and  $B$  is the applied magnetic field. Given the direct relationship between particle mass and the magnetic force acting on the particle, the magnetic field is adjusted so that electrons are affected by it, while the heavier ions remain practically unaffected. This results in a longer travel path for the electrons, increasing the probability of hitting, and subsequently, ionizing an argon atom.

### 3.1.2 Sputtering and Plasma Characteristics

A plasma is a partially ionized gas and can be formed by heating or applying a voltage to the said gas. When the voltage is high enough the gas will become conductive, and a voltage arc forms between the anode and cathode in the chamber. This ionizes the gas, and free electrons are emitted as a result. An inert gas such as argon is most often used as the plasma forming species to prevent incorporation in the final film. The incident ion energy has to be sufficiently large to sputter off a target atom. If the energy is too high however the incident ions will be implanted into the target, and no sputtering will occur. The  $\text{Ar}^+$ -ions forming the plasma collide with the target material, knocking off sputtered atoms and secondary electrons. These negatively charged electrons are accelerated away from the target by the electric field, ionizing more argon atoms on their way. The ionization rate from these secondary electrons increases further away from the target, resulting in an increasing ion density, moving from the target to the plasma. Moving even further away from the target, there is a build-up of positive charge, shielding electrons from the electric field and thus lowering their kinetic energy. This results in a region close to the cathode termed the *dark space* of the plasma, where no optical emission occurs due to an insufficient excitation of the argon atoms. The discussion above is valid for DC sputtering systems with a conductive target material.

### 3.1.3 Sputter yield and deposition rate

The sputter yield ( $S$ ) is a key parameter in sputtering processes. It is defined as the number of atoms ejected from the target material ( $Z_e$ ) per incident ion ( $Z_i$ ), and is of great importance to the deposition rate.

$$S = \frac{Z_e}{Z_i} \quad (3.3)$$

It is, however, not the only parameter that influences the deposition rate. Ion flux towards the target and the ability of ejected atoms to travel through the plasma also affects the growth rate of the sputtered film. The mobility of sputtered atoms at the substrate surface is governed by substrate temperature and the binding energy between the substrate species and the sputtered atoms. The kinetic energy of ejected target atoms when they reach the substrate will also affect the mobility. The mobility at the sample surface determines whether or not the adatoms settle at the most energetically favourable position. The surface mobility of the adatoms is governed by the substrate temperature and ion energy, which in turn is a product of target power and chamber pressure. There is a threshold to both substrate temperature and ion energy, however, beyond which the structural integrity of the crystal will suffer. If the substrate temperature is too high, the deposited material can deteriorate. Likewise, if the target power is inappropriately high, the structure will suffer continuous damage throughout the deposition. Therefore, there is an optimum temperature and target power where the surface mobility is suitable for different growth regimes [33]. If the surface mobility is insufficient, the adatoms will bond at an unfavourable position, resulting in, e.g. amorphous and porous films, by increasing the substrate temperature, and thus the surface mobility, denser films are formed. This is because of a reduced shadowing effect from other grains as well as an increased probability of an adatom finding a suitable nucleation site. Depositions with high temperature and high target power result in larger grain size. As this project aims to grow single crystalline  $\text{ZnSnN}_2$ , high surface mobility is of great importance.

### 3.1.4 RF Sputtering

In order to sputter insulating or low conductive materials, it is necessary to use an RF (radio frequency) voltage source. When sputtering an insulating material, the ejection of secondary electrons, in addition to target species, causes a build-up of positive charge on the target surface, which eventually will extinguish the plasma. Therefore, an AC signal at radio frequencies accelerates positive ions towards the target when the signal is negative, and negative electrons when the signal is positive, eliminating a surface charge build-up at the target. Because of the large disparity in the mobility of ions and electrons, due to the significant difference in mass, the electrons contribute more to the electron flow through the anode than ions contribute to the flow at the cathode. This asymmetry means that the self-bias of the RF sputtering system is negative.

### 3.1.5 Reactive Sputtering

The composition of a sputtered film depends on the target material(s), but it is possible to incorporate other elements by sputtering in a reactive atmosphere, a process termed *reactive sputtering*. As an example,  $\text{ZnO}$  thin films can be grown either by sputtering of a ceramic  $\text{ZnO}$  target in vacuum, or by sputtering a Zn metal target in an O-flow. Reactive sputtering allows for a more flexible sputtering process, as it is possible to alter the gas incorporation by adjusting the gas flow, rather than using compound

targets with set compositions. The gas incorporation depends on partial pressures, plasma characteristics and sputtering power within the chamber. Reactive sputtering allows for the deposition of insulating materials in DC mode since only the target has to be conductive. Reactive sputtering is an important technique in the development of ZnSnN<sub>2</sub> thin films as ZnSnN<sub>2</sub> targets are currently unavailable. Therefore, reactive co-sputtering of metal Zn and Sn targets in N<sub>2</sub> flow is utilized in this work.

### 3.1.6 High-power Impulse Magnetron Sputtering

High-power impulse magnetron sputtering (HiPIMS) is a magnetron sputtering technique where the applied voltage is delivered in short, high power pulses, typically two-three orders of magnitude greater than that used in conventional DC magnetron sputtering systems [34]. The duration of these pulses is significantly shorter than the interval between them, with pulse durations down to tens to hundreds of a microsecond, and frequencies up to 5 kHz. Although the peak pulse power is high, the average power is not damaging to the target nor magnetron.

Compared to conventional DC sputtering, HiPIMS yields a somewhat lower deposition rate at similar powers. The average target power ( $P_{avg}$ ) is given by

$$P_{avg} = V_{avg}I_{avg} \quad (3.4)$$

where  $V_{avg}$  is the average voltage and  $I_{avg}$  is the average current. HiPIMS has a significantly higher  $V_{avg}$  than conventional DC sputtering at the same power, implying that  $I_{avg}$  is correspondingly low. The average current is closely related to the ion flux, and a reduced ion flux towards the target reduce the deposition rate.

Due to the high applied voltage utilized in HiPIMS, free electrons can be accelerated and become ionizing, releasing secondary electrons from neutral gas atoms. These secondary electrons are accelerated and can ionize a second neutral gas atom. Thus HiPIMS leads to a higher degree of ionization of the sputtered target material compared to conventional DC and RF sputtering. The low-energy, high-flux ion irradiation in HiPIMS allows for lower substrate temperatures, higher deposition rates, and produces films of uniform thickness with good adhesion to the substrate [35]. Since thin film growth properties are directly influenced by the energy of the sputtered species, HiPIMS allows for greater control of the thin film growth than conventional DC sputtering would. HiPIMS has tunable parameters that are inaccessible in DC sputtering systems. Pulse width, frequency and peak current can be adjusted, which gives the operator greater control of the deposition and allows for depositions of elements not normally compatible with DC sputtering. HiPIMS leads to a higher degree of N<sub>2</sub>-ionization, allowing for greater incorporation of elemental nitrogen in the films. The formation of N<sub>2</sub>-bubbles incorporated in the structure are common for sputtered nitrides, as shown by Bazioti *et al.* [36]. Thin film growth by HiPIMS typically leads to smoother and denser thin films [37, 38]. It is theorized that the energetic bombardment of the growing structure is the source of this densification. As this work revolves around the growth of nitrides, the degree of N<sub>2</sub>-ionization is of critical importance.

Although ZnSnN<sub>2</sub> thin films grown by HiPIMS are relatively unexplored, Olsen *et al.* [14] obtained single crystalline ZnSnN<sub>2</sub> thin films with an epitaxial relationship to ZnO substrates employing this method.

All sputtering depositions were performed using the Polyteknik Flextura Cluster system at MiNaLab. This system has two growth chambers, a load-lock for sample mounting, an annealing chamber and an analytical chamber. The magnetron sputtering chamber used in this study contains 5 sputtering sources, and allows for reactive and ordinary magnetron sputtering with two DC sources, two RF sources and HiPIMS, employed either individually or simultaneously. Metallic targets of Zn, Sn and Si were employed in the reactive sputtering processes for the different thin films. In order to obtain Li doped ZnSnN<sub>2</sub> films, a Li doped Zn-target with a Li concentration of 1 wt.% was used. Nitrogen of 99.9999% (6N) purity was used in the reactive atmosphere, the Ar gas used was 99.999% pure.

## 3.2 X-Ray Diffraction

X-ray diffraction (XRD) is a powerful characterization technique used to investigate a wide range of structural properties of a material. The method is non-destructive and can give information about material phases, the crystalline structure, the quality and orientation of the structure, as well as strain. The technique utilize monochromatic x-rays directed at a mounted sample and then detecting scattered x-rays. The atoms that constitute a crystal structure align themselves in crystallographic planes, with an inter-planar spacing  $d_{hkl}$ . According to Bragg's law, an incident x-ray beam will be scattered with constructive interference when

$$n\lambda = 2d_{hkl} \sin(\theta) \quad (3.5)$$

is satisfied, where  $\lambda$  is the wavelength of the incident x-ray,  $n$  is an integer and  $\theta$  is the angle between the crystal plane and incident beam. For this relation to be valid  $2d$  must be greater than, or equal to,  $\lambda$ . A demand that is satisfied for wavelengths in the x-ray range of the electromagnetic spectrum. When an incident x-ray is scattered by an atomic plane of spacing  $d_{hkl}$  between planes, a phase shift of  $2d\sin(\theta)$  occurs for any angle  $\theta$ . From equation (3.5), this phase shift results in constructive interference when  $\theta$  is equal to  $2d(hkl)$ . A visualization of this can be found in figure 3.2. To detect this constructive interference, a detector is mounted opposite the x-ray source, at an angle  $\theta$  relative to the sample surface.

The distance  $d_{hkl}$  is related to the hexagonal lattice parameters and the Miller indices  $(hkl)$  of the crystal by

$$\frac{1}{d_{hkl}^2} = \frac{4}{3} \left( \frac{h^2 + hk + k^2}{a^2} \right) + \frac{l^2}{c^2} \quad (3.6)$$

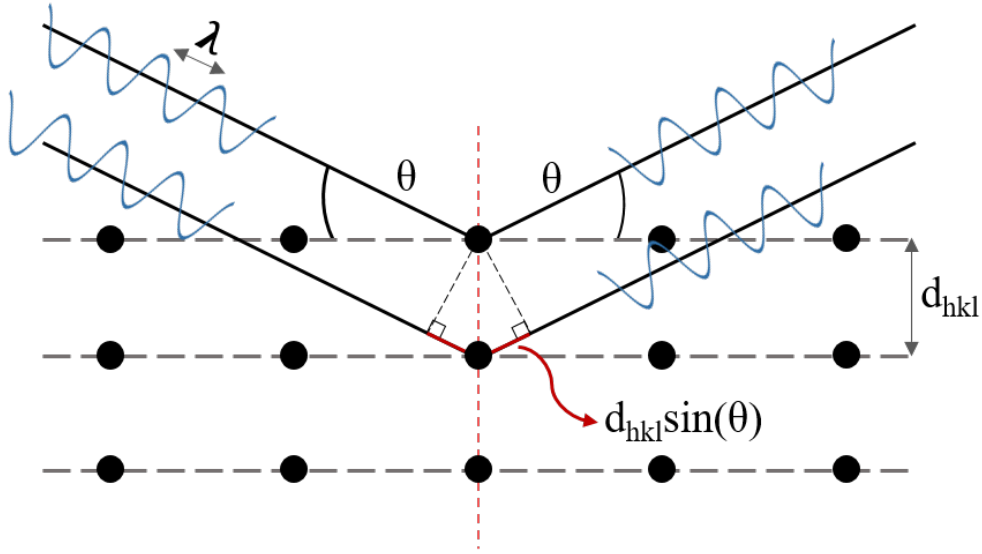


Figure 3.2: Illustration representing diffraction in a crystal with atomic planar spacing of  $d_{hkl}$ . Incident x-rays with wavelength  $\lambda$ .

By implementation of equation (3.6) in Bragg's law, it is evident that by scanning over a wide range of angles ( $\theta$ ), the lattice planes yielding constructive interference will yield a peak in the resulting diffraction pattern.

$$\sin^2 \theta = \frac{\lambda^2}{4a^2} \left[ \frac{4}{3}(h^2 + hk + k^2) + \frac{l^2}{(c/a)^2} \right] \quad (3.7)$$

### 3.2.1 $\theta/2\theta$ Scan

Given the amount of information one can obtain by exploiting diffraction and Bragg reflections, XRD is one of the most powerful tools within crystallographic characterization techniques. To register the Bragg reflections and their intensity, the x-ray source and a detector is mounted on two separate, mobile arms, forming a constant radius hemisphere encapsulating the sample. A simple illustration of a  $\theta/2\theta$  setup is shown in figure 3.3. Because the distance between the sample and the source/detector-hemisphere is constant, any variations in measured intensity stem from interactions between the sample and the beam. Two distinct  $\theta/2\theta$  scans are presented in this work. A wide survey scan between  $20^\circ$  and  $100^\circ$  in order to locate all reflections and their higher order replicas, and a high-resolution scan of the expected (0002) reflection of  $\text{ZnSnN}_2$  at  $32.65^\circ$ . [39]

A  $\theta/2\theta$  scan results in a plot of registered counts vs.  $\theta$ , with peaks corresponding to crystal planes parallel to the substrate surface, i.e. the (0001) growth direction. The position, height and width of these peaks contain information about the structural characteristics of the sample material. Peak positions and their higher order replicas, as discussed previously, contain information about the interplanar spacing between atomic layers, and thus can be used to distinguish materials and phases. The width of a Bragg

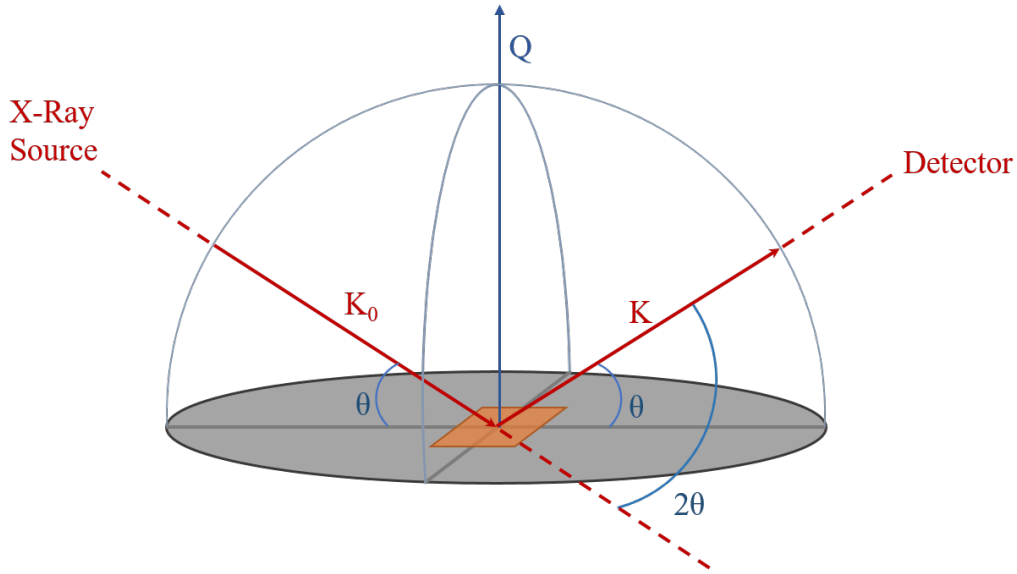


Figure 3.3: The  $\theta/2\theta$  scan experimental setup. The angle between the sample plane and the source ( $\theta$ ) is equal to the angle between the sample plane and the detector. The incident and diffracted x-ray beams are described by the vectors  $\mathbf{K}_0$  and  $\mathbf{K}$  respectively.

reflection peak determines the spread in interplanar spacings for that reflection. In all real materials, there are defects present, all of which affect the interplanar spacing to some extent, which again can be related to crystallite grain size. As a result of lattice mismatch in heteroepitaxially grown thin films, i.e.  $\text{ZnSnN}_2$  grown on  $\text{ZnO}$ , either tensile or compressive strain may build up in the crystal structure. This strain is relieved at a critical thickness, typically for sample thicknesses of some tens of nm, for example in the form of dislocations.

### 3.2.2 Rocking Curve Scan

A rocking curve ( $\omega$ ) scan is conducted by locking the detector at an intensity maximum of a Bragg reflection. The incident x-rays are then scanned over a set of angles corresponding to the  $2\theta$  values of said Bragg reflection. The tilt of the sample is denoted by  $\omega$ , and is related to the surface normal.  $\omega$  is described by

$$\omega = \theta - \frac{2\theta_0}{2} \quad (3.8)$$

The  $\omega$  scan returns an intensity plot as a function of tilt. Since the detector is fixed at a specific Bragg reflection, a  $\omega$  scan of a perfect crystal will only return a signal when  $\omega = 0$ . If there are tilted lattice planes present in the crystal, however, these tilted planes will give rise to constructive interference at an angle  $\omega \neq 0$ . This implies that a signal for  $\omega \neq 0$  corresponds to a reflection of a lattice plane, not parallel to the sample surface, as illustrated in figure 3.4 (a). The scattering vector,  $\vec{Q}$ , is shifted from the surface normal for such reflections, whereas  $\vec{Q}$  is normal to the sample surface for the entirety of a  $\theta/2\theta$  scan. A wide  $\omega$  peak may indicate disruptions in the parallelism

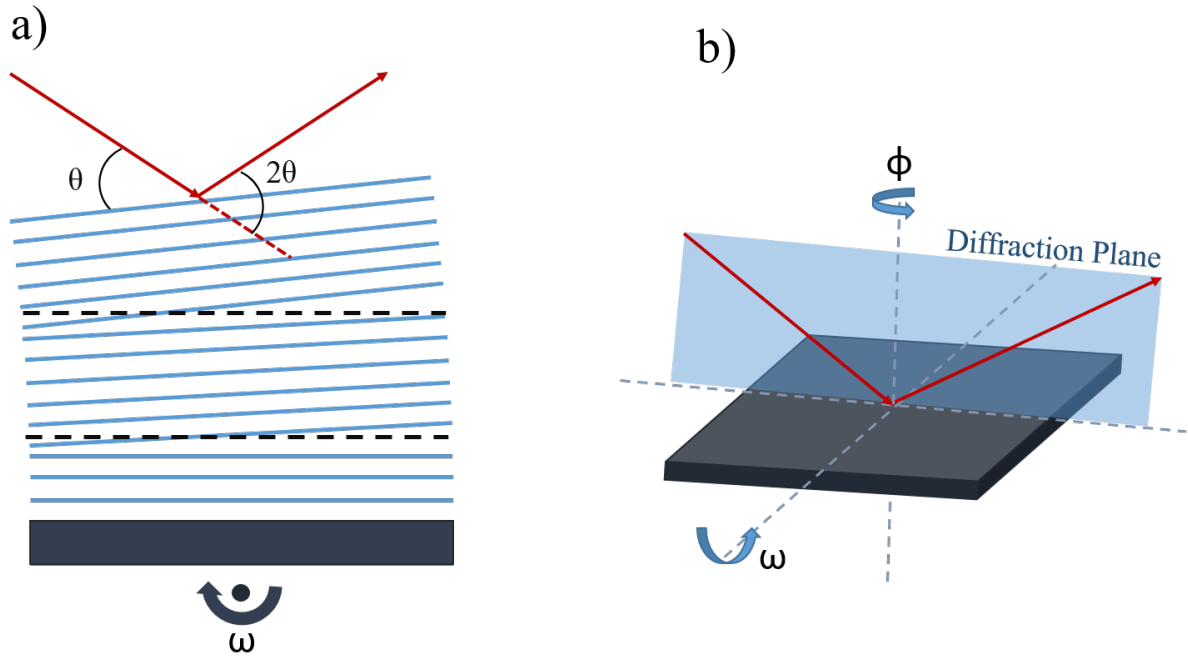


Figure 3.4: a) Illustration of how tilted lattice planes are detected in a  $\omega$  scan, b) representation of the  $\phi$ - and  $\omega$ -axis in an XRD experimental setup.

of the atomic planes in the crystal. Tilt may form as a result of crystal defects, in particular dislocations. Dislocations can again be the result of the crystal relieving strain caused by lattice mismatch with the substrate. A high value of full width at half maximum (FWHM) of the  $\omega$  peak can be interpreted as a significant amount of tilted lattice planes, oriented in a set of angles. The FWHM of a  $\omega$  peak can therefore be an indication of the dislocation density in the thin film.

### 3.2.3 Phi Scan

A  $\phi$  scan is done at a specific Bragg reflection with  $\theta/2\theta$  held constant, rotating the sample stage  $360^\circ$  around the  $c$ -axis ( $\phi$ -axis) of the crystal. The purpose of such a scan is to determine rotational symmetries in the crystal structure. In the case of hexagonal wurtzite, a six-fold rotational symmetry would manifest itself in a spectrum as six distinct peaks, each separated by  $60^\circ$ . Whereas the  $\theta/2\theta$ -scan is employed to determine lattice planes parallel to the growth direction in this work, the  $\phi$ -scan identifies planes that are not normal, nor parallel to, the  $c$ -axis. An illustration of the  $\omega$ - and  $\phi$ -axis can be found in figure 3.4 (b).

All XRD measurements were done by a Bruker AXS D8 Discover utilizing a Cu x-ray source with characteristic wavelengths  $k_{\alpha 1} = 1.5406 \text{ \AA}$  and  $k_{\alpha 2} = 1.54444 \text{ \AA}$ . The  $k_{\alpha 2}$  signal was filtered out by a Ge (220) double bounce monochromator. An instrumental broadening of  $0.0008^\circ$  has to be accounted for in the measurements.

### 3.3 Hall Effect Measurement

Hall effect measurements is a technique that measures the resistivity of a sample. The setup requires at least four ohmic contacts, e.g. at the periphery of a symmetrical sample. This configuration is termed the van der Pauw method, and illustrated in figure 3.5 (a). The sample has to meet four criteria for the van der Pauw method to be valid: i) the contacts are placed on the edges of the sample, ii) the contact area is at least one order of magnitude smaller than the sample, iii) the sample surface is free of holes and isolated islands, iv) the sample is flat and of homogeneous thickness.

#### 3.3.1 Hall Effect Theory

An illustration of a Hall effect measurement is shown in figure 3.5 (b), and is conducted to determine the resistivity of a material. Given the resistivity, it is possible to calculate carrier concentration and mobility. Without any external interference, the electrons will travel from contact 1 to contact 4 with a velocity related to the current magnitude

$$\nu = \frac{I}{nAq} \quad (3.9)$$

where  $n$  is the carrier concentration,  $A$  is the cross sectional area of the sample,  $q$  is the elementary charge and  $I$  is the current.

As electrons with charge  $q$  moves through an applied magnetic field normal to the sample surface,  $\vec{B}$ , there is a Lorentz' force,  $\vec{F}_L$ , acting on the electrons

$$\vec{F}_L = q\vec{\nu} \times \vec{B} \quad (3.10)$$

This force pushes the electrons perpendicular to the current and magnetic field, in the case of figure 3.5 (b) where the electrons move from terminal 4 to 1, towards terminal 3. This leads to a build-up of electrons at terminal 3, which in turn generates an electric field  $E$ . This field and its associated force,  $F_E$ , counteracts  $F_L$  and an equilibrium between the forces is reached, effectively preventing further build-up of charge at terminals 2 and 3. An expression for  $E$  at this equilibrium point can be found through the two forces associated with the electric fields counteracting each other,  $F_E = F_L$ .  $F_L$  is related to the electron velocity,  $\nu$ , through equation (3.10). Combining equation (3.10) with equation (3.9) an expression for  $E$  can be found,

$$E = \frac{I}{nAq} B \quad (3.11)$$

By integrating this field over the width of the sample,  $W$ , we get the associated *Hall voltage*,  $V_H$

$$V_H = \int_0^W E dW = WE = \frac{WIB}{nAq} = \frac{IB}{qnt} \quad (3.12)$$

From  $V_H$  it is possible to calculate the *Hall coefficient*,  $R_H$ , the sign of which is determined by the polarity of the sample (negative implies electrons are the majority carrier, positive implies that holes are the majority carrier).

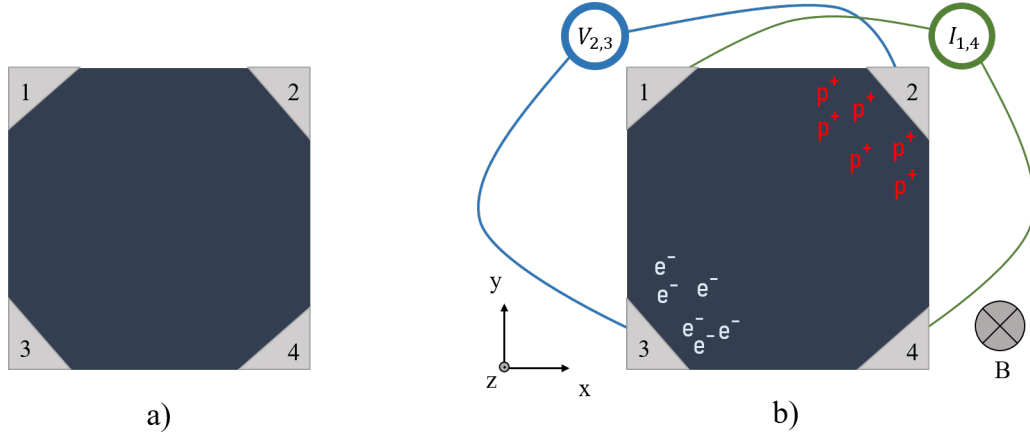


Figure 3.5: a) Example of a van der Pauw setup, with ohmic contacts, labeled 1-4, at each of the four corners of the sample. b) Illustration of a Hall effect measurement. A current is applied between contacts 1 and 4, and the voltage drop is measured over contacts 2 and 3. A magnetic field,  $B$ , is applied uniformly over the sample, the direction of which is in the negative  $z$ -direction.

$$R_H = \frac{V_H t}{IB} \quad (3.13)$$

$R_H$  is an important factor as it is related to the carrier concentration through

$$n = \frac{r}{q|R_H|} \quad (3.14)$$

where  $r$  is a *Hall scattering factor*, as the expression assumes that the limiting mobility scattering mechanisms are independent of energy.

### 3.3.2 The van der Pauw Method

The van der Pauw method is a technique employed to measure the resistivity and Hall coefficient of a material. The resistivity ( $\rho$ ) is related to carrier concentration ( $n, p$ ) and mobility ( $\mu_{n,p}$ ) through

$$\sigma = \frac{1}{\rho} = q(n\mu_n + p\mu_p) \quad (3.15)$$

where  $q$  is the elementary charge,  $n$  and  $p$  is the electron and hole concentrations, and  $\mu_n$  and  $\mu_p$  is the mobilities of electrons and holes, respectively. For an  $n$ -type material,  $n \gg p$ , and the expression is simplified to  $\sigma \sim qn\mu_n$ . Similarly for  $p$ -type materials, where  $p \gg n$ ,  $\sigma \sim qp\mu_p$ .

The measurements are carried out by applying a current  $I$  between two contacts while measuring the voltage drop  $V$  over the remaining contacts. For example, one can apply a current between contacts 1 and 2, and measure the voltage drop between contacts 3 and 4. The resulting resistance can be expressed as

$$R_{12,34} = \frac{V_4 - V_3}{I_{12}} \quad (3.16)$$

Similarly, if a current is applied between contacts 1 and 4 and a voltage drop is measured over 2 and 3, the measured resistance is

$$R_{14,23} = \frac{V_3 - V_2}{I_{14}} \quad (3.17)$$

By measuring the resistance for all equivalent geometries, and reversing the current, two average resistances can be calculated

$$R_1 = \frac{R_{12,34} + R_{34,12} + R_{21,43} + R_{43,21}}{4} \quad (3.18)$$

$$R_2 = \frac{R_{23,41} + R_{41,23} + R_{32,14} + R_{14,32}}{4} \quad (3.19)$$

With  $R_1$  and  $R_2$  known, one can calculate the resistivity through the relation

$$\rho = \frac{\pi t}{\ln(2)} \frac{R_1 + R_2}{2} F \quad (3.20)$$

where  $t$  is the sample thickness and  $F$  is a sample specific uniformity factor. In the special cases where the sample is circular or square,  $F = 1$ , therefore it is expedient to make the samples as symmetrical as possible. The van der Pauw method is a powerful technique because measurement of the resistance and Hall coefficient of the material makes resistivity, mobility and carrier density easily obtainable through equations (3.14) and (3.20).

The determination of electrical properties of the sputtered  $\text{ZnSnN}_2$  is critical in material optimization for solar cell applications, as these are imperative physical properties in such a component. The conductivity of a semiconductor is proportional to both carrier concentration and mobility, thus directly related to the current density of a potential  $pn$ -junction. Equally interesting is the temperature dependency of the carrier densities and mobilities, which can be evaluated through temperature-dependent Hall (TdH) measurements. During a TdH measurement, the temperature is lowered, thus "clearing" the conduction band of electrons. As the temperature is increased, a series of Hall measurements are conducted, and it is thus possible to register the temperature at which the carrier concentration increase. There are typically two main scattering mechanisms that limit carrier mobility in a semiconductor, *phonon scattering* and *impurity scattering*. The dominating mechanism depends on the temperature of the material. For lower temperatures, ionized impurities in the crystal structure will dominate, as lattice vibrations are a direct consequence of thermal energy in the material. The temperature dependency of the carrier density can indicate defect energy levels of certain defects, such as  $\text{Li}_i$ . TdH measurements can be challenging, however, as the current passing through the sample may heat the sample if the resistance is too high.

The Hall measurements of this thesis have been conducted with the Lakeshore 7604 Hall effect measurement system at MiNaLab, which allows for both room temperature measurements, as well as temperature dependent measurements in the range of 20-300 K, with an applied magnetic field strength of 1.0T. The measurements were carried out in an inert He atmosphere.

## 3.4 SEM EDS

Scanning Electron Microscopy (SEM) is a form of microscopy that utilizes a focused beam of electrons to form an image. The implementation of electrons rather than light allows for magnifications up to 200 000 times and can gather information about the relative composition within a sample, as well as the surface topography. This section is based on the textbook of Goldstein [29].

SEM conducts a raster scan of the surface, using a series of electromagnetic lenses to manipulate the electron beam. The focused electron beam interacts with the sample-atoms producing back scattered- and secondary electrons. Secondary electrons are a product of ionization, whereas back scattered electrons are primary electrons which have been deflected by an atomic nucleus of the sample material. The frequency of which back scattered electrons are created depends on the mass of the nucleus of the sample. These emitted and scattered electrons are then analyzed by a detector, and it is possible to construct a digital image of the sample surface. Typically, heavier elements tend to produce more back scattered electrons than lighter elements because of their bigger nuclei. Thus, areas with heavier elements appear brighter than areas with lighter elements in an SEM generated image. Since the finely tuned electron beam is sensitive to electric fields, the sample has to be conductive to prevent a build-up of charge at the sample surface.

### 3.4.1 Energy Dispersive X-Ray Spectroscopy

Energy Dispersive X-Ray Spectroscopy (EDS) is a characterization technique often used in tandem with SEM to gather compositional data of a sample. When an incident electron from the electron beam hits an atom in the sample, the incident electron energy, if sufficiently high, can excite an electron out of its shell, leaving an empty state. When an electron of an outer shell decays back to its initial energy state, the excess energy is released as a photon. The energy difference in electron shells close to the atomic nucleus corresponds to photons in the X-ray range of the electromagnetic spectrum, thus X-rays are emitted. A detector can measure these X-rays, and characterize them by their wavelength.

Given the numerous energy states electrons can occupy in an atom, there are several possible transitions that can occur. Every element has a characteristic emission profile, making it possible to identify the different elements of a sample. This emission profile is used to calculate the ratios of constituents in the sample, with precision between

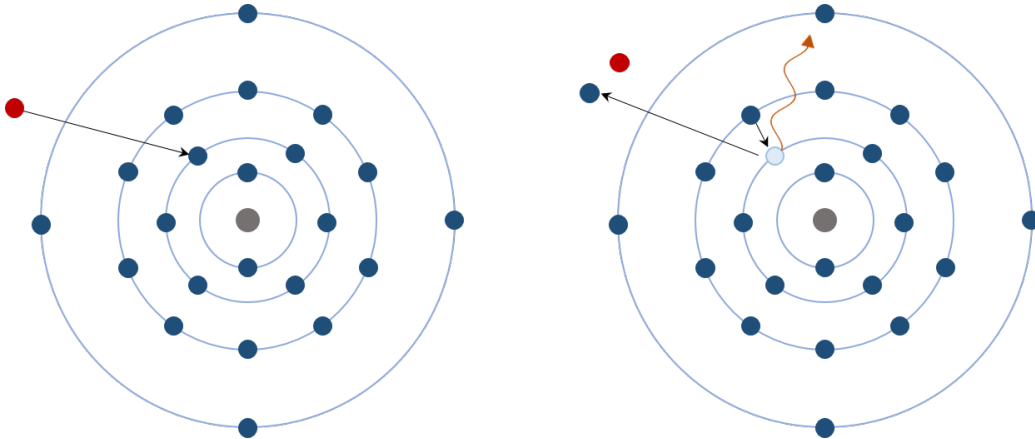


Figure 3.6: Illustration of X-ray emission as a result of an incident electron knocking an electron out of its energy state.

0.1 – 0.5 wt.%. It is not possible, however, to measure trace amounts of elements, e.g. doping concentrations.

The emission profile of heavier elements is easy to distinguish, as there are several X-ray intensities associated with each element. Distinguishing between lighter elements such as nitrogen and oxygen can be challenging. Lighter elements (atomic number 11 or less) only have one characteristic wavelength, making it difficult to distinguish their signals from other overlapping elements. Another complicating factor is that of *fluorescence yield*. Defined as the fraction of ionization events resulting in characteristic X-ray radiation rather than Auger electrons, the fluorescence yield is lower for lighter elements. Thus, elements of low atomic number produce less characteristic X-rays, complicating the identification of e.g. nitrogen in  $\text{ZnSnN}_2$ . The electrons involved in the X-ray emission process in lighter atoms are also affected by the bonding conditions of the material; their energy can thus be shifted, altering the X-ray fingerprint of the element.

SEM EDS measurements were employed in this work in order to determine the composition of the grown films, especially the cation ratios, as these are predicted to affect the carrier concentration of the material [17, 18]. In addition to this, SEM EDS allows us to examine the surface of the films in greater detail than an optical microscope would. All SEM EDS measurements presented in this thesis were undertaken employing the JSM-IT300 SEM at MiNaLab with a  $\text{LaB}_6$  filament. This electron microscope is equipped with a ThermoFischer UltraDry EDS detector, used for compositional analysis. A working distance between 11-12 mm and an acceleration voltage of 10 keV was employed.

### 3.5 Atomic Force Microscopy

This section is based on the textbook of Rogers, Adams and Pennathur [30]. Atomic force microscopy (AFM) is a form of scanning probe microscopy used to perform topo-

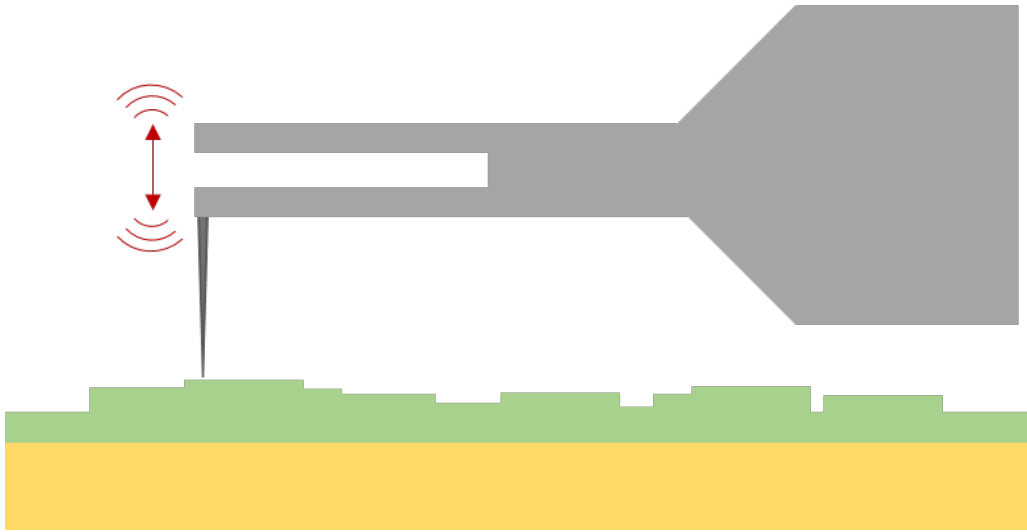


Figure 3.7: Schematic of a tapping mode Atomic Force Microscope. The tuning fork resonates at its resonant frequency, tapping the sample surface in its extended state.

graphical measurements of a sample. With resolutions between 0.1 - 1 nm, AFM is a powerful tool when investigating the topography of deposited thin films. The working principle of AFM is to sweep a probe over the sample surface, measuring the force between the probe and sample surface. There are generally two main configurations to consider, related to AFM. i) The most common one being the beam bounce technique, which relies on a probe connected to a cantilever, on which a reflector is situated. A laser is directed at the reflector, which is then reflected onto a photodetector. The movement of the probe as it is swept across the sample surface will be translated to the reflector, which will divert the laser beam onto the position-sensitive photodetector. ii) a tuning fork configuration, illustrated in figure 3.7, where the probe is mounted on a tuning fork vibrating at its resonant frequency.

In general, there are two main operating modes associated with AFM; *contact* mode and *tapping* mode. In contact mode, the probe is in contact with the sample at all times during a raster scan. In tapping mode the probe resonates at a set frequency, tapping the sample surface as it is rastered across the surface. One advantage of tapping mode AFM is that it is a semi-contact mode, meaning that it is less destructive than a full contact mode scan. Another advantage is that the phase change of the cantilever is sensitive to height differences, this is ideal for imaging of e.g. grain boundaries, which can be obscured by variations in topography.

The tapping mode probe can be mounted on a tuning fork sensor, with the probe set at one of the prongs, with the base fixed. A compensating mass is attached to the opposite prong to maintain the resonant frequency of the tuning fork. The tuning fork works as the frequency determining element of an oscillator of constant amplitude. The amplitude of the oscillations is altered when the tip passes over elevations or depressions in the surface topography, leading to a change in frequency. The probe height is adjusted so that the resonant frequency is restored, it is this height change

that is recorded and converted into a topographic image.

AFM was employed in this thesis in order to investigate the surface topography of the grown films. High resolution raster scans of the surface might reveal columnar growth typical for grown nitrides, as well as the width and depth of potential surface pits in this. AFM performed in this work was done using a Nanonics Imaging SPM Multiview - 2000, utilizing a Cr coated tuning fork probe in tapping mode, with a resonant frequency of 32.24kHz.

### 3.6 UV-VIS Spectrophotometry

When investigating candidates for novel PV materials, an understanding of their interactions with light is crucial. Light waves can interact with semiconductors in four different ways; transmission, reflection, absorption and scattering. UV-VIS (ultraviolet - visible light) spectroscopy measures how much of an incident beam of light is transmitted, reflected and absorbed as a function of wavelengths.

Beer-Lambert's law relates the intensities of incident light on to a sample, to transmitted light through the following equation

$$I_t = I_0 e^{-\alpha(\lambda)d} \quad (3.21)$$

assuming no scattering processes occur in the material. Where  $I_t$  and  $I_0$  are the intensities of the transmitted and incoming light, respectively.  $\alpha(\lambda)$  is the wavelength dependent transmission coefficient, and  $d$  is the sample thickness. During a transmission measurement, a monochromatic light beam is focused on a sample. The sample itself is mounted on the perimeter of an integral sphere, the inside of which is covered in a highly reflective material. Even though the Beer-Lambert law assumes no scattering, some portion of the light will be scattered in the material. The reflective interior of the integral sphere assures as much as possible of the transmitted light reach the detector, often mounted at the top or bottom of the integral sphere.

For reflection measurements, the sample surface is mounted towards the centre of the integral sphere. The incident beam travels through an aperture before it enters the integral sphere, and light reflected by the sample is directed back into the integral sphere illustrated in figure 3.8. This specific setup is termed direct reflectance measurement and suffers from specular reflection obscuring the results. In addition to ordinary reflectance measurements, diffuse reflectance will be conducted, assuming a direct band gap in  $\text{ZnSnN}_2$ .

$$T = \frac{(1 - R)^2 e^{-\alpha d}}{1 - R^2 e^{-2\alpha d}} \sim (1 - R)^2 e^{-\alpha d} \quad (3.22)$$

where  $T$  is the percentage of transmitted light,  $R$  is the percentage of direct reflected light and  $d$  is the thin film thickness. Equation (3.22) is simplified for high absorption.

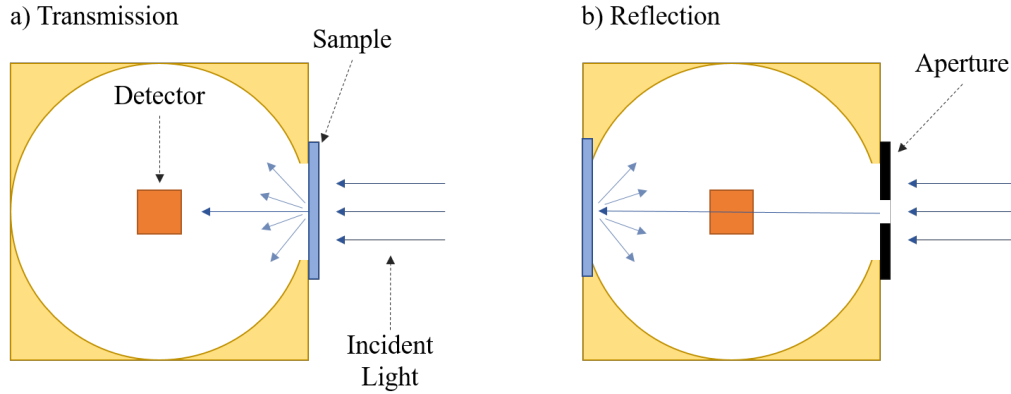


Figure 3.8: The experimental setups of a) transmission and b) direct reflection measurements.

### 3.6.1 Tauc Analysis

Through analysis of the transmittance and reflection data, one can estimate the optical band gap of the material. The absorption coefficient ( $\alpha$ ) is closely related to the optical band gap from the equation

$$[\alpha(E)h\nu]^{1/n} = C(h\nu - E_g) \quad (3.23)$$

where  $\alpha(E)$  is the absorption coefficient for an incident photon with energy  $E$ ,  $h\nu$  is the photon energy,  $C$  is a structure dependent constant,  $E_g$  is the band gap and  $n$  is 1/2 or 2 for direct and indirect allowed transitions, respectively. To determine the optical band gap,  $(h\nu\alpha)^{\frac{1}{n}}$  is plotted as a function of photon energy. By linear extrapolation of the resulting graph, one can estimate the band gap to be where the extended graph cross the abscissa [40]. This extrapolation has an associated deviation, commonly named the *Urbach-* or *absorption tail*, which is usually governed by structural disorder, surface passivation and localized states [41], [42]. This method is termed *Tauc analysis*, and the band gap acquired through this analysis is often underestimated. An important limitation of this method is the necessity of a linear region in the  $(h\nu\alpha)^{\frac{1}{2}}$  plot, as this is not necessarily the case.

Transmittance and reflectance measurements by UV-VIS photospectrometry were undertaken in this work to investigate the absorption onset of the grown ZnSnN<sub>2</sub> films. Linear extrapolation of the absorption onset is used in estimates of the optical band gap of the material, a property of ZnSnN<sub>2</sub> still under investigation. The UV-VIS photospectrometry in this work was done with a Shimadzu SolidSpe-3700 DUV spectrophotometer with wavelengths between 300 nm to 1500 nm and a step size of 0.1 nm.

## 3.7 Photoluminescence Spectroscopy

PL measurements presented in this thesis have been conducted by Dr. Augustinas Galeckas. This section is based on the review article of Gilliland [31]. Photoluminescence

(PL) spectroscopy is based on the optical excitation of charge carriers in a semiconductor, and the monitoring of the emitted photons as these excited charge carriers decay back to their initial energy state. The energy distribution of these photons can reveal information of the radiative recombination mechanisms involved, e.g. involving defects. The photoluminescence is dispersed by a spectrometer, after which it is detected. Once an electron is optically excited, there are several recombinatory mechanisms that can occur. Recombination mechanisms can be divided into two groups, radiative and non-radiative. The electron-hole recombination of a direct semiconductor is a radiative process, emitting photons as excited charge carriers decay to their initial energy state. The emission of Auger electrons, where an electron is ejected instead of a photon, is a non-radiative recombination process. It is the radiative processes that are examined with PL. With both an electron and a hole present, band-to-band recombination is possible. An electron at the CBM can recombine with a hole at the VBM, emitting a photon with energy corresponding to the band gap energy. In some materials, the excited electron-hole-pair can form a quasi-particle called an *exciton*. An exciton forms when an electron is excited to an energy state above the CBM, creating an EHP which is attracted to each other through coulombic forces. The exciton has no net electric charge, as the charges of the electron and hole cancel each other out. As the exciton can move freely in the crystal lattice, it can transport energy even though it is not electrically charged. In a perfect material, the main signal from PL spectroscopy stems from free-exciton recombination. With defects and impurities present, however, recombination centers can exist within the band gap. The position of which depends on the chemical identity and charge state of the defect at hand. Donor and acceptor levels lie near the CBM and VBM respectively. Thus, PL is utilized in this work to gain the optical emission profile of  $\text{ZnSnN}_2$ , to identify possible band-to-band recombination.

PL measurements were undertaken in this work to investigate the optical emission properties of stoichiometric  $\text{ZnSnN}_2$  at different temperatures. PL measurements presented in this work were undertaken in vacuum at 10 K and 300 K employing a 325 nm wavelength He-Cd cw-laser with a power density  $<1 \text{ Wcm}^{-2}$ . The emission was analyzed with a Horiba Jobin Yon iHR320 imaging spectrometer system coupled with an Andor iXon888 Ultra EMCCD.

### 3.8 SIMS

The SIMS measurements presented in this thesis have been conducted by Prof. Lasse Vines. Secondary Ion Mass Spectrometry (SIMS) is a characterization technique used to identify and quantify the concentrations of different elements in a material. With detection limits in the range of parts per billion (ppb), it is one of the most sensitive elemental and isotopic analysis techniques. The working principle of SIMS is a bombardment of a sample with primary ions (often  $\text{Ar}^+$ ,  $\text{Ga}^+$ ,  $\text{Cs}^+$  or  $\text{O}^+$ ), sputtering secondary ions, neutral atoms and molecules of the sample surface. SIMS only measure the sputtered secondary ions, accounting for approximately 1% of the total sputtered material. SIMS is associated with two operational modes; *dynamic* and *static* SIMS. Dynamic SIMS mode, which is employed in this work, uses a high primary ion flux to

remove several atomic layers, investigating the bulk composition and in-depth analysis of trace elements in the sample as a function of depth. Static SIMS use a low flux of primary ions to analyze the sample surface exclusively.

An ion source generates the primary ions, which are passed through an electromagnetic filter, removing unwanted ions. To reduce the influence of external particles, the sample is under a high vacuum. The primary ion beam is passed through a series of electromagnetic lenses and can be deflected using a deflector. Several approaches exist to detect secondary ions, including a magnetic sector analyser, a quadrupole, and a time-of-flight. In the work presented in this thesis, a magnetic sector analyser has been used. In this case, the sputtered secondary ions are accelerated towards an electrostatic sector analyzer equipped with two curved metal plates at different potential for energy filtering. To analyze the mass of the secondary ions, a magnetic sector analyser is used. The secondary ions are passed through a magnetic field perpendicular to their velocity vector, accelerated by a potential difference. The path of the ions will be curved by the magnetic field as they are electrically charged, and the radius of this curve is dependent on the ionic mass. The magnetic field is then adjusted so that only the desired ions are passed through a slit, where they are registered by a detector. A mass spectrum can be acquired through variation of the magnetic field in the magnetic sector analyzer. By slowly increasing the magnetic field, ions of different mass will pass through the analyzer slit. A depth profile is obtained by keeping the magnetic field strength constant, thus only ions of a certain mass are allowed to pass through to the analyzer. The intensity of a certain signal (ionic counts per second) is measured as a function of time, which can be converted to concentration vs. depth.

As Li doped ZnSnN<sub>2</sub> films are of interest due to the carrier suppressing possibilities of the Li<sub>Zn</sub> defect, an understanding of the Li distribution in the films would be beneficial. The high detection limits of SIMS make it possible to acquire Li depth profiles, as well as concentrations. In order to acquire concentrations, however, a reference sample of known doping concentration at specific depths is needed. Such a reference is often made by ion implantation. In addition to this, SIMS allows for superior thickness measurements compared to that of stylus profilometry.

SIMS measurements were done by a Cameca IMS-7f microanalyzer equipped with a Duoplasmatron (O<sub>2</sub>) and a Cs primary ion source, a magnetic sector analyzer, an electrostatic sector analyzer and secondary ion detectors.

### 3.9 Ion-Implantation

Ion implantation in this work was performed by senior engineer Viktor Bobal at MiN-aLab. Ion implantation is a technique used to introduce impurities into a material. The process relies on ions accelerated by an electrostatic field striking the surface of a target material. By monitoring the ion current it is possible to control the ion dose precisely, often in the range of  $10^{11} \text{cm}^{-2}$  to over  $10^{18} \text{cm}^{-2}$  [6]. With ion energies commonly in

the range of a few keV to several MeV, it is possible to control the penetration depth of the ions.

The introduction of impurities in the crystal lattice will alter the resistivity of the implanted material, the effect of which is determined by the charge of the incident species, as well as ion flux and ion energy, as shown by Johra *et al.* [43].

A consequence of ion implantation is that of substrate damage, and increased lattice parameters are commonly seen in implanted materials. When the high energy ions strike the substrate, they collide with substrate atoms transferring energy. If the energy transferred during a collision event is sufficiently high, the target atom may be kicked out of its lattice position, creating a Frenkel defect pair. Some displaced substrate atoms have enough energy to produce additional displaced atoms, causing considerable substrate damage. Depending on the dose, ion energy, substrate binding energy and substrate temperature, the damage can be substantial, even rendering the substrate amorphous.

This work will include nitrogen and phosphorous implanted ZnO. The implantation of N and P is done to form an insulating top-layer on the ZnO substrate. Specifically, box-implantations were made. That means that, e.g., N was implanted with two different doses using two different energies in order to form this layer. By forming this layer, we maintain the wurtzite ZnO surface for epitaxial growth of ZnSnN<sub>2</sub>, while it is possible to measure the electrical properties of the thin film. The P and N implanted ZnO was annealed at 800°C and 1150°C in an oxygen atmosphere for 60 minutes to reduce the implantation damage and restore the substrate surface for epitaxial growth. The temperature of the annealing step was chosen to be high enough to restore the surface, and low enough to prevent diffusion of the implanted element. The implantation was done using the NEC Tandem Accelerator at MiNaLab, with a terminal voltage of 1 MV. For both P- and N-implantation, the ions were implanted with doses of (i)  $1 \times 10^{14} \text{ cm}^{-2}$  with an energy of 36 keV and (ii)  $2 \times 10^{14} \text{ cm}^{-2}$  with an energy of 180 keV.

# Chapter 4

## Process Development

In order to control the depositions and optimize the sputtering parameters, a significant amount of process development was conducted. Reactive co-sputtering with both RF and HiPIMS sources yield a wide parameter space for process development. To investigate which parameters alter specific properties in the deposited films, a systematic iterative process in which a single parameter was tuned at a time, often increasing or decreasing within a series of depositions, was conducted. Because of the high cost of, and significant workload associated with, single crystalline implanted ZnO, the process development was performed mainly on Si and *c*-Al<sub>2</sub>O<sub>3</sub> substrates. Si was used as it is a cheap and available substrate, as well as conductive, allowing for SEM EDS measurement of the deposited films. *c*-Al<sub>2</sub>O<sub>3</sub> was employed for electrical characterization through Hall effect measurement, due to its insulating properties. The lattice constants of *c*-Al<sub>2</sub>O<sub>3</sub> is not ideal for growth of Zn-IV-nitrides, however. Thus the crystal quality of the deposited ZnSnN<sub>2</sub> was sub-optimal, likely due to the large lattice mismatch. Through development on cheaper and more available substrates, we were quite certain of the compositional and electrical properties of the recipes, allowing for deposition of entire series on implanted ZnO substrates. All samples developed in this work is presented in table 4.1.

When I entered the project, a recipe for stoichiometric films had already been developed. It was clear however, that the carrier density of the stoichiometric films were too high, and likely degenerate ( $n > 10^{20}\text{cm}^{-3}$ ). In theory, there are two prevailing routes to reduce the carrier density of the films. *i*) reduce the incorporation of extrinsic impurities, e.g. O<sub>N</sub> defects which works as double donors, and *ii*) altering the stoichiometry of the films, more precisely the Zn/(Zn+Sn) ratio. First principle calculations predict that the cation antisite defects Zn<sub>Sn</sub> and Sn<sub>Zn</sub> acts as acceptors and double donors, respectively [17, 18]. Thus, by making the films Zn-rich, the carrier concentration should be suppressed in two distinct ways,

Table 4.1: Table presenting all series discussed in this thesis, with their growth parameters and composition. Each series is denoted by a subscript; "S" - Stoichiometric, "OR" - Oxygen Reduced, "NS" - Non-Stoichiometric and "Li" - Li Doped.

	HiPIMS Power [W]	HiPIMS Frequency [Hz]	RF Power [W]	Process Pressure [mbar]	N <sub>2</sub> Flow [sccm]	Deposition Time [min]	Zn [at. %]	Sn [at. %]	N [at. %]	Zn/(Zn+Sn)
<b>Stoichiometric</b>										
A <sub>S</sub>	44	1400	43	$2.00 \times 10^{-3}$	20	180	20.8±1.04	21.4±1.07	57.8±2.89	0.49
B <sub>S</sub>	44	1400	47	$2.00 \times 10^{-3}$	20	180	20.5±1.02	22.0±1.10	57.5±2.87	0.48
C <sub>S</sub>	44	1400	49	$2.00 \times 10^{-3}$	20	180	20.4±1.02	22.5±1.12	57.1±2.85	0.48
D <sub>S</sub>	44	1400	46	$2.00 \times 10^{-3}$	20	180	20.5±1.02	21.2±1.06	58.3±2.92	0.49
<b>Non-Stoichiometric</b>										
A <sub>NS</sub>	44	1400	43	$2.00 \times 10^{-3}$	20	180	24.47±0.20	24.93±0.21	50.60±1.07	0.50
B <sub>NS</sub>	44	1400	35	$2.00 \times 10^{-3}$	20	180	27.80±0.22	22.44±0.21	49.76±1.23	0.55
C <sub>NS</sub>	44	1400	30	$2.00 \times 10^{-3}$	20	180	35.09±0.27	18.43±0.18	46.48±1.33	0.66
D <sub>NS</sub>	44	1400	25	$2.00 \times 10^{-3}$	20	180	40.99±0.32	11.99±0.17	47.01±1.87	0.77
A <sub>NS,cap</sub>	44	1400	43	$2.00 \times 10^{-3}$	20	180	27.02±0.22	23.35±0.24	49.63±1.11	0.54
B <sub>NS,cap</sub>	44	1400	35	$2.00 \times 10^{-3}$	20	180	32.83±0.26	20.16±0.22	47.01±1.14	0.62
C <sub>NS,cap</sub>	44	1400	30	$2.00 \times 10^{-3}$	20	180	35.43±0.27	18.88±0.21	45.69±1.18	0.65
<b>Li Doped</b>										
A <sub>Li</sub>	44	1400	43	$2.00 \times 10^{-3}$	20	180	23.95±0.24	26.08±0.19	49.25±1.31	0.48
B <sub>Li</sub>	44	1400	35	$2.00 \times 10^{-3}$	20	300	27.80±0.22	22.44±0.21	49.76±1.23	0.55
C <sub>Li</sub>	44	1400	30	$2.00 \times 10^{-3}$	20	420	35.09±0.27	18.43±0.18	46.48±1.33	0.66
D <sub>Li</sub>	44	1400	25	$2.00 \times 10^{-3}$	20	533	36.93±0.41	15.86±0.23	47.20±1.39	0.70

through the implementation of acceptors and the reduction in double donors. A non-negligible amount of O in the films were confirmed by SIMS, thus reduction in O incorporation was prioritized in the first half of the work.

## 4.1 Reducing Oxygen Incorporation

In principle, the Polyteknik FLEXTURA cluster allows for a reduced incorporation of O compared to conventional sputtering instruments as the deposition chamber is under constant pump-down and the base pressure is in the range of  $10^{-8} - 10^{-9}$  mbar. The only gasses present in the low-pressure environment should ideally have been  $N_2$  and Ar. The Ar is supplied by an industrial grade Ar flask, rendering this unlikely to be the source of contamination. The  $N_2$ -source however, was the house gas at MiNaLab, which was connected directly to the FLEXTURA cluster system. As we saw this as a potential source to the O contamination, we connected the house gas to a purifier to remove as much O from the house gas as possible. This was not as effective as theorized, however, with carrier densities in the deposited films still  $> 10^{20} cm^{-3}$ . To ensure that the  $N_2$  supplied to the chamber was of desired purity, a 6N-flask was connected directly to the cluster system. If the  $N_2$ -supply was the source of contamination, the carrier density should have been reduced noticeably. This was not the the case.

Most nitrides are also reactive, oxidizing the surface when exposed to air. This may affect the electrical characterization of the  $ZnSnN_2$  films. We therefore developed a procedure in which the deposited films were covered with a  $Si_3N_4$  capping layer *in-situ*. This capping layer complicated the characterization process, obscuring thickness measurements obtained through stylus profilometry and rendering compositional analysis by SEM EDS challenging. The insulating nature of the capping layer made Hall effect measurements challenging. To overcome this, Al-contacts had to be deposited on the substrate and covered with Kapton tape before the film was to be deposited. The Al contacts were deposited using the Ångström e-beam evaporator located in the clean room at MiNaLab. Figure 4.1 explains the entire deposition process, with contacts and capping layer. SIMS confirmed the capping layers to be approximately 50 nm thick.

Room temperature Hall effect measurements of the capped  $ZnSnN_2$  discussed above, showed no noticeable decrease in carrier density. This meant that the source of contamination most likely was located within the cluster system. This lead us to disconnecting the O-supply from the cluster system completely. This combined with a high purity  $N_2$  supply, bake-out and flushing procedures of the deposition chamber and capping layer on the films, reduced the O-content in the film, confirmed by SIMS. Interestingly, even though the O-concentration was reduced significantly, no equivalent reduction in carrier density was observed. This implies that other defects, e.g. the  $Sn_{Zn}$  antisite has a greater contribution to the degenerate nature of  $ZnSnN_2$  in our experiments.

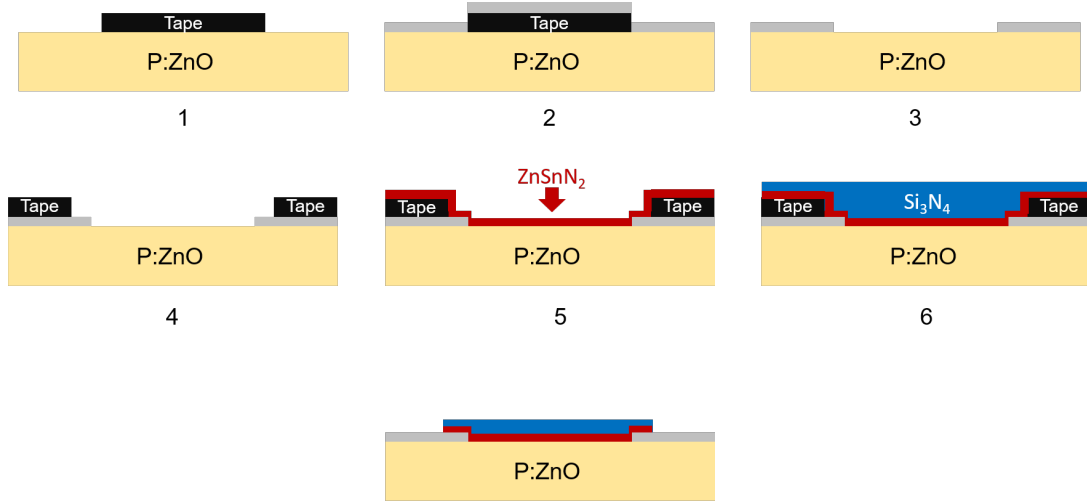


Figure 4.1: Illustration of the capping layer deposition in seven steps. 1) The P-implanted ZnO substrate is covered with an aluminium mask, exposing the corners, 2) Al contacts were deposited onto the substrate, 3) the mask is removed, revealing the exposed substrate with Al contacts in the corners, 4) part of the contacts are covered with kapton tape, 5)  $\text{ZnSnN}_2$  (red) is deposited, 6)  $\text{Si}_3\text{N}_4$  capping layer (blue) is deposited, 7) the tape is removed exposing the contacts.

## 4.2 Non-stoichiometric Growth

The second prevailing route to non-degenerate  $\text{ZnSnN}_2$  thin films is non-stoichiometric growth [16, 44]. The goal was to deposit a series of samples with an increasing  $\text{Zn}/(\text{Zn}+\text{Sn})$  ratio, incorporating  $\text{Zn}_{\text{Sn}}$  antisite acceptors, and reducing the amount of  $\text{Sn}_{\text{Zn}}$  antisite donors. Using the recipe for stoichiometric films as a template, we tuned the Zn- and Sn-target powers to alter the  $\text{Zn}/(\text{Zn}+\text{Sn})$  ratio of the  $\text{ZnSnN}_2$  thin films. Initially, the HiPIMS Zn-target power was increased, while all other parameters remained unaltered. Compositional analysis by SEM EDS confirmed the  $\text{Zn}/(\text{Zn}+\text{Sn})$  ratio of these films to be overwhelmingly Zn-heavy, with a  $\text{Zn}/(\text{Zn}+\text{Sn}) = 0.78$ . Thus, the RF Sn-target power was decreased. With reduced sputtering power on the RF Sn-target, fewer Sn atoms should be sputtered off and deposited, creating films with  $\text{Zn}_{1+x}\text{Sn}_{1-x}\text{N}_2$  composition. The cation ratios of the comparatively low RF Sn-target power deposited samples were Zn-rich, but the  $\text{Zn}/(\text{Zn}+\text{Sn})$  ratio remained excessive, above 65%. As it proved difficult to lower the RF power further while maintaining a stable plasma, we reduced the HiPIMS frequency by 10% while the RF target power remained low. This resulted in a series with steadily increasing Zn incorporation. The data suggests, however, that the N incorporation was affected by the lowered Sn power, implying nitrogen poor films. Due to SEM EDS' limited ability to detect lighter elements however, there are significant uncertainties associated with these N values, and we assume that the films have sufficient nitrogen incorporation. As a consequence of the reduced sputtering power the sputter yield decreased as well, resulting in thinner films. This is illustrated in figure 4.2. To account for this we prolonged the deposition

times in parallel with the decreasing power. Hall effect measurements were conducted on N implanted ZnO and c-Al<sub>2</sub>O<sub>3</sub> substrates to investigate the non-stoichiometric effect on the electrical properties. XRD measurements was undertaken on ZnSnN<sub>2</sub> deposited on ZnO substrates to investigate the structural properties of the thin films.

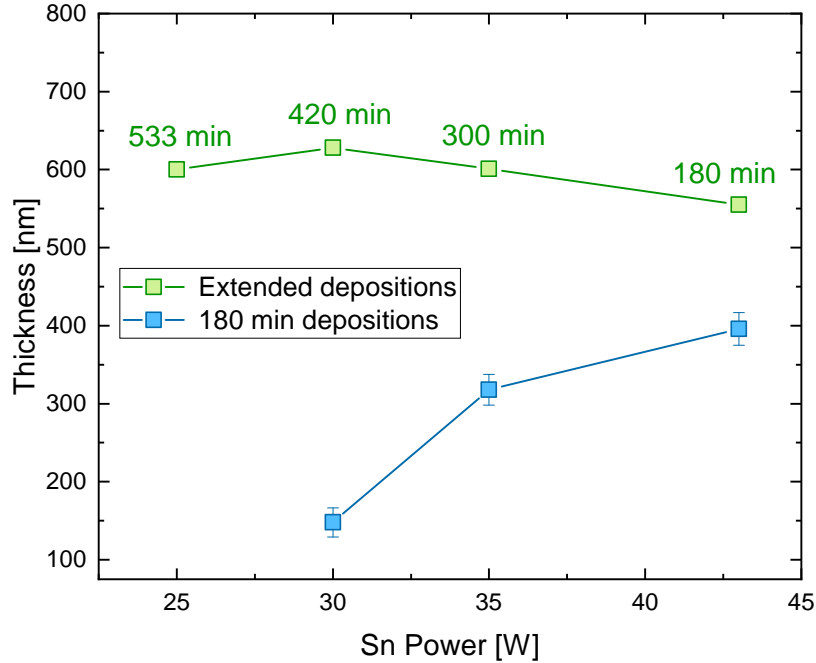


Figure 4.2: Thin film thickness of two separate Zn-rich series of constant (blue) and extended (green) deposition times. The extended series, Li-doped in table 4.1, was measured by SIMS, the constant series was measured by stylus profilometry.

### 4.3 Development of Li-doped ZnSnN<sub>2</sub>

In addition to non-stoichiometry as a means to lower carrier concentration, doping the ZnSnN<sub>2</sub> films with Li was of interest. Acceptor doped ZnSnN<sub>2</sub> is yet to be properly investigated besides first principle calculations. Attempts to find literature reporting of Li doping ZnSnN<sub>2</sub> was unsuccessful, although Ba-doped ZnSnN<sub>2</sub> has been reported by Chinnakutti *et al.* [45]. An additional argument for a Li doped series, is that it proved difficult to maintain the structural integrity of the hexagonal wurtzite ZnSnN<sub>2</sub>, investigated through XRD, for off-stoichiometric samples. In order to lower the carrier densities to an acceptable level, while preserving the crystal quality, a process for doping the ZnSnN<sub>2</sub> films with Li was developed. The Li<sub>Zn</sub> defect is theorized to act as an acceptor in ZnSnN<sub>2</sub>, effectively lowering the majority carrier density.

A new Zn-target doped with 8.69 at.% (1.00 wt.%) Li was installed at the HiPIMS. This should have resulted in a uniform Li distribution through the film as long as the sputtering process remained stable. A new series with identical deposition parameters

as the non-stoichiometric series presented in table 4.1 was thus deposited. As with the non-stoichiometric series, the Li-doped series was deposited on Si substrates for compositional analysis by SEM EDS, and *c*-Al<sub>2</sub>O<sub>3</sub> and P implanted ZnO for electrical, optical and structural characterization through Hall effect, UV-VIS and XRD measurements, respectively. SIMS results confirmed substantial Li-incorporation. The film thickness was measured utilizing a stylus profilometer and SIMS.

Reducing the carrier concentration of deposited ZnSnN<sub>2</sub> is crucial for the material to be fit for solar cell applications. It was therefore of high priority for this work. The many possible contributions to the degenerate state of ZnSnN<sub>2</sub> made the process development difficult and time consuming, however, as each deposition series had to be thoroughly examined for the project to proceed.

# Chapter 5

## Results and Discussion

The development of  $\text{ZnSnN}_2$  for solar cell applications require an understanding of the native properties of the material. We have therefore grown stoichiometric, single crystalline  $\text{ZnSnN}_2$  thin films as a basis for further material exploration. However, the stoichiometric  $\text{ZnSnN}_2$  films were heavily  $n$ -type, limiting the material's applicability in a potential tandem cell arrangement. Thus, potential donors and acceptors were investigated through oxygen reducing measures, non-stoichiometric growth, i.e.  $\text{Zn}_{1+x}\text{Sn}_{1-x}\text{N}_2$ , and Li-doping to gain an understanding of the charge carrier origins of  $\text{ZnSnN}_2$ .

### 5.1 Stoichiometric Thin Films

The study of  $\text{ZnSnN}_2$  in the context of a solar absorber requires an understanding of the intrinsic properties of the material, e.g. the optical band gap. Hence, development of stoichiometric single crystalline  $\text{ZnSnN}_2$  is explored. Stoichiometric  $\text{ZnSnN}_2$  was deposited on N-implanted ZnO,  $c\text{-Al}_2\text{O}_3$  and Si substrates, labeled  $A_s$ ,  $B_s$ ,  $C_s$  and  $D_s$ . The sputtering parameters are presented in table 4.1. As the II-IV-nitrides are considered as a potential earth-abundant alternative to the group III-nitrides, ZnO was chosen as a substrate for heteroepitaxial growth, due to its low lattice mismatch with  $\text{ZnSnN}_2$ . AlN, GaN and InN all tend to grow in a wurtzite crystal structure [46], and it is thus expedient to obtain this crystal structure for the novel II-IV-nitrides for further exploration between the two material groups, i.e. heteroepitaxy. All four stoichiometric samples had a good Zn/(Zn+Sn) ratio determined by SEM EDS, between 0.48 and 0.49. The corresponding N-content are presented in table 4.1, at  $\sim 57$  at.%. Within the accuracy of SEM EDS however, these films are expected to be stoichiometric.

#### 5.1.1 Structural Analysis of Stoichiometric Films

The crystal quality of the thin films was evaluated through XRD measurements. The crystalline quality of a film will affect the optoelectronic properties of the material. Structural defects can, as an example, contribute to a larger Urbach tailing in Tauc analysis [41, 42], act as non-radiative recombination centers [47, 48], as well as limit the carrier mobility in the material [49, 50]. Hence, we aimed to reduce the uncertainties in

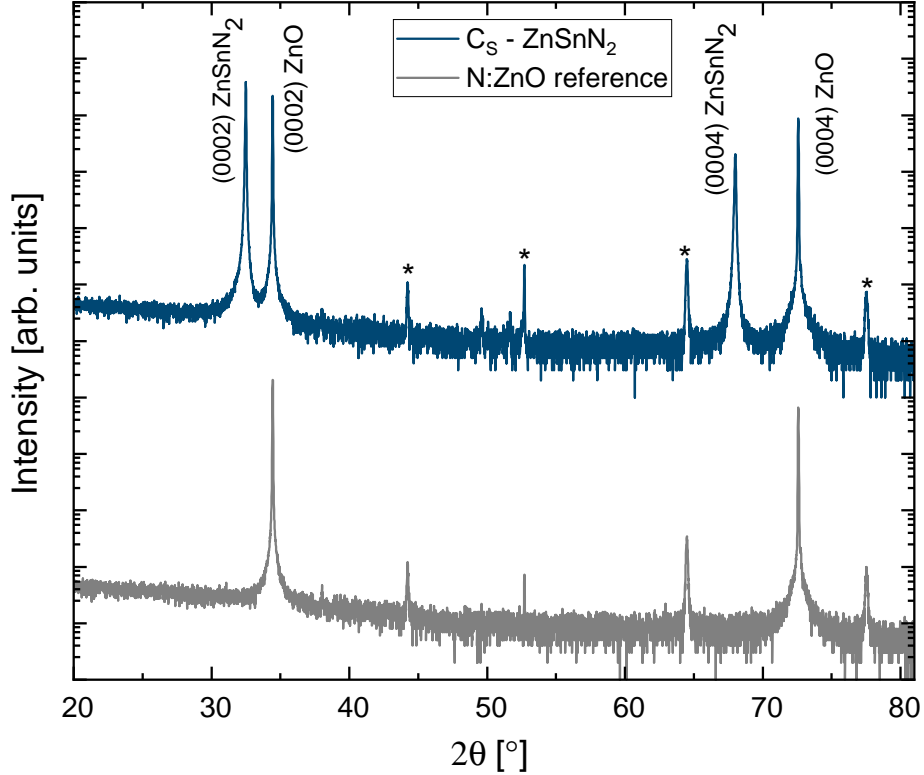


Figure 5.1:  $\theta/2\theta$  survey scan of a stoichiometric  $\text{ZnSnN}_2$  thin film (sample  $C_s$ ) deposited on N-implanted ZnO. The lower spectrum represents an equivalent measurement on a N-implanted ZnO substrate, as reference. Peaks labeled (\*) are related to the sample stage of the XRD equipment.

determining fundamental properties of  $\text{ZnSnN}_2$ , e.g., the optical band gap, by growing single crystalline thin films on ZnO substrates. ZnO was chosen as a substrate as its lattice parameters match those of  $\text{ZnSnN}_2$  closely, with a lattice mismatch of  $\sim 4.2\%$  [15]. However, ZnO is conductive at room temperature, and obscures any electrical characterization of the deposited films. Thus, the ZnO substrates were implanted as described in section 3.9.

As a result of ion implantation, the lattice constant of a material is generally increased, this effect is reduced by a post-implanting annealing step [51]. A reference  $\theta/2\theta$  survey scan was undertaken on an N-implanted ZnO substrate, presented in figure 5.1. The resulting spectrum displays two distinct peaks at  $34.4^\circ$  and  $72.6^\circ$ . These peaks correspond to the (0002) plane and its (0004) higher order replica, as expected for (0001)-cut single crystalline ZnO. The  $\theta/2\theta$  survey scan of stoichiometric  $\text{ZnSnN}_2$  presented in figure 5.1 exhibit two additional dominant reflections located at  $32.4^\circ$  and  $68.0^\circ$ , related to the (0002) plane of wurtzite phase  $\text{ZnSnN}_2$ , and its (0004) plane replica. The remaining peaks in the spectrum are related to the ZnO substrate or the sample holder, labeled with (\*). The absence of other  $\text{ZnSnN}_2$ -related diffraction peaks indicates wurtzite  $\text{ZnSnN}_2$  with a close to epitaxial relationship to the ZnO substrate, and that

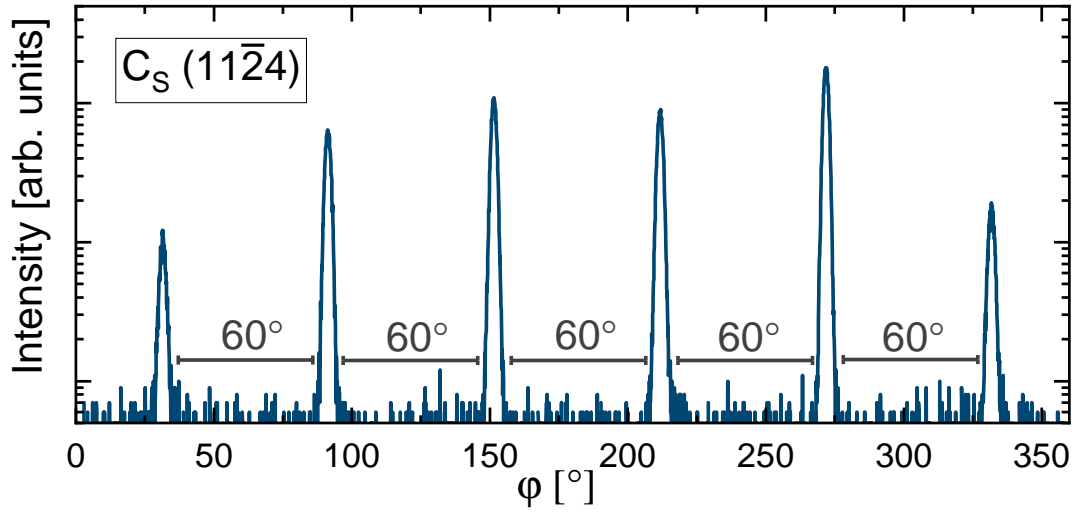


Figure 5.2:  $\phi$ -scan displaying the  $(11\bar{2}4)$  reflections of sample  $C_S$ , with a separation of  $60^\circ$  implying six fold symmetry.

no secondary phases have been formed during growth. The  $(0002)$   $\text{ZnSnN}_2$  FWHM was calculated to be  $0.05^\circ$  indicating a relatively uniform lattice spacing throughout the crystal. The interplanar atomic distance,  $d_{hkl}$ , which corresponds to the  $c$ -lattice constant, is calculated from the positioning of the  $(0002)$  reflection at  $34.44^\circ$  and found to be  $c = 0.554 \pm 0.005$  nm. To further examine the crystallographic properties of the  $\text{ZnSnN}_2$  thin films,  $\phi$ -scans were conducted, shown in figure 5.2. Figure 5.2 shows the rotational symmetry of the  $(11\bar{2}4)$  reflection of  $\text{ZnSnN}_2$ . Six distinct reflections, separated by  $60^\circ$ , strongly indicates a six-fold symmetry and thus hexagonal structure. Similar scans were undertaken for the  $(10\bar{1}4)$  reflection, also exhibiting six-fold symmetry (see figure A.2 in appendix A). Hence, combining the  $\theta/2\theta$  reflections and the six-fold symmetry equal to the wurtzite  $\text{ZnO}$  substrate, strongly indicate that  $\text{ZnSnN}_2$  is grown in the hexagonal wurtzite crystal structure with an epitaxial relationship to the substrate.

To further examine the crystal quality, a rocking curve ( $\omega$ )-scan was conducted. With  $2\theta$  fixed in the  $(0002)$  reflection of  $\text{ZnSnN}_2$  at  $32.44^\circ$ ,  $\theta$  was scanned from  $15^\circ$  to  $18^\circ$ . This scan symmetry is equivalent to tilting the sample, and thus the tilt of the  $(0002)$  planes can be evaluated. For a bulk, single crystal, the resulting diffraction results in a sharp and narrow peak. Broadening of the diffraction peak measured with a  $\omega$ -scan may indicate disruptions in the parallelism, termed tilting, of the atomic planes, which again may be caused by structural defects, e.g. dislocations. Thus, the FWHM of the diffraction peak measured with a  $\omega$ -scan can be used as an indication of the dislocation density in the thin film. Depending on which diffraction peak is evaluated, an estimation of the upper limit of different types of dislocations can be made. Threading dislocations (TDs) are a typical feature of nitride thin films, as they are extended defects that can emerge from imperfections at the interface between the substrate and the grown film [52]. There are generally three distinct TDs associated with III-nitride

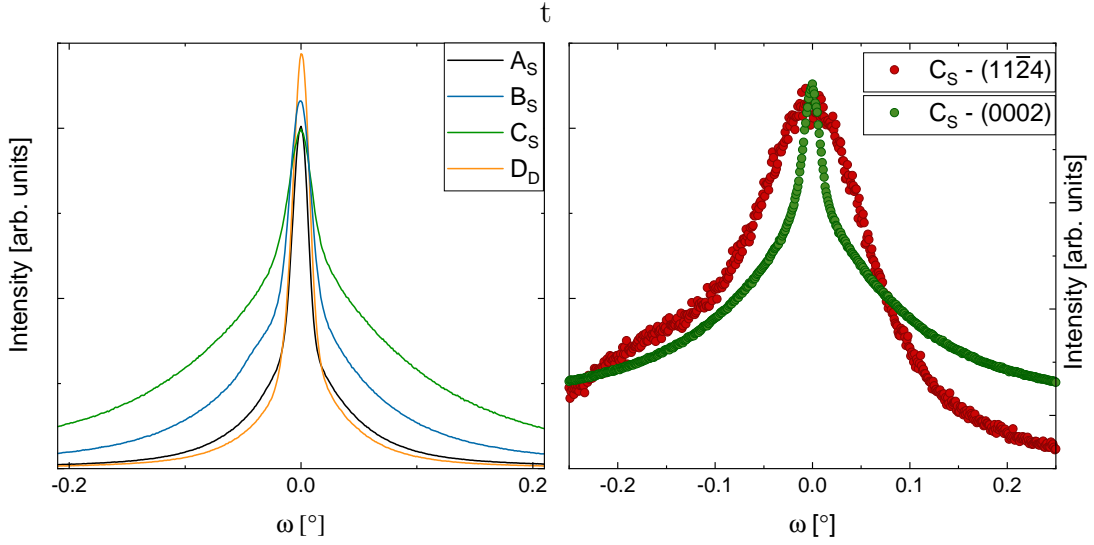


Figure 5.3: Rocking curve scan in the a) (0002) reflection for the stoichiometric series and b) the (11 $\bar{2}$ 4)- and (0002) reflections of sample  $C_S$ .

semiconductors; screw-TDs, edge-TDs and mixed type TDs, with corresponding Burger's vectors  $\mathbf{b}_s = \langle 0001 \rangle$ ,  $\mathbf{b}_e = 1/3 \langle 11\bar{2}1 \rangle$  and  $\mathbf{b}_m = 1/3 \langle 11\bar{2}3 \rangle$ , respectively [53]. As the edge-TDs tend to extend in directions normal to the growth direction, they will not affect an  $\omega$ -scan in the (0002) plane. Screw- and mixed type-TDs however, can cause tilting of lattice planes, and thus broadening in the resulting diffraction peak of a  $\omega$ -scan in the (0002)- and (11 $\bar{2}$ 4)-reflections, respectively. The  $C_S$  sample (0002) plane  $\omega$ -scan presented in Figure 5.3 (a), has a FWHM of  $0.05^\circ$ . The upper limit screw threading dislocation density ( $\rho_s$ ) can thus be estimated through the equation [54], [55]

$$\rho_s = \frac{\beta_\omega^2}{4.35c^2} \quad (5.1)$$

where  $\beta_\omega$  is the FWHM of the (0002) reflection acquired through a  $\omega$ -scan,  $c$  is the  $c$  lattice parameter of  $\text{ZnSnN}_2$  assumed to be equal to the Burgers-vector along the  $c$ -axis. A FWHM of  $0.05^\circ$  corresponds to an upper limit screw threading dislocation density  $\rho_s = 1.9 \times 10^7 \text{ cm}^{-2}$ . The  $\omega$ -scans detect lattice plane tilts with respect to a certain axis only, thus edge threading dislocations ( $\rho_e$ ), perpendicular to the  $c$ -axis, were not estimated through this technique, as it requires measuring lattice planes normal to the sample surface, which is not possible with the current instrumentation at MiNaLab. An assessment of these types of defects can be made, however, given that  $\rho_e > \rho_s$  is typical for III-nitrides [56], we assume that the same holds true for  $\text{ZnSnN}_2$ . With this regard, the actual dislocation densities of the thin films are likely to be higher than reported in this thesis. This is further supported by a higher FWHM of an  $\omega$ -scan of the (11 $\bar{2}$ 4) reflection, which can be used to estimate an upper limit of mixed-type TDs, i.e. both edge- and screw-TDs, presented in figure 5.3 (b). As a result, the total dislocation density in the  $\text{ZnSnN}_2$  is expected to be higher than estimated with equation (5.1). Recent work carried out by Olsen *et al.* [14] includes cross sectional

transmission electron microscopy (TEM) images of sputtered  $\text{ZnSnN}_2$  grown epitaxially on ZnO substrates. The image displays screw-TDs emerging from the ZnO substrate, propagating through the grown film. The TEM analysis reported a total dislocation density in the range of  $1 \times 10^{10} - 5 \times 10^{10} \text{ cm}^{-2}$ , substantially higher than those obtained through XRD measurements. Screw threading dislocations may be a result of the crystal releasing strain due to lattice mismatch with the substrate and is commonly seen in heteroepitaxially grown nitride films [57] along with misfit dislocations.

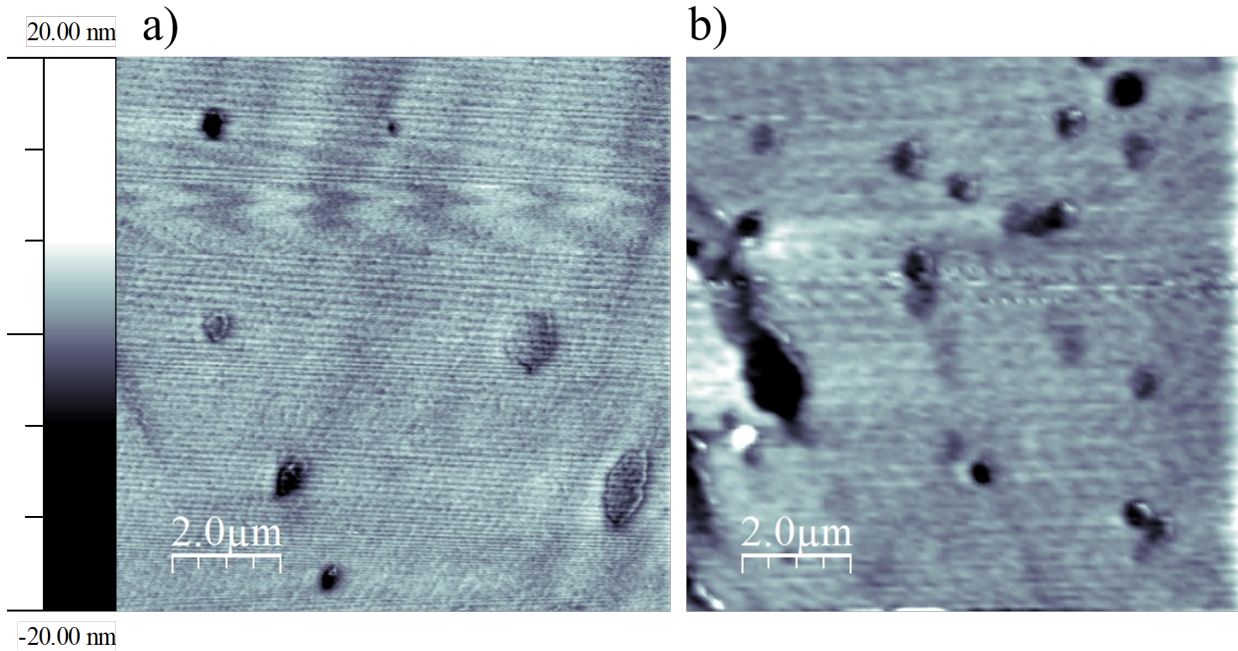


Figure 5.4: Topographical images of a sample  $C_s$ , displaying surface defects, manifested as pits. The raw data collected by the tuning fork SPM was processed in the WSxM software, applying parabolic flattening.

### Topography

Topographical analysis of the sample surface was undertaken applying a tuning fork scanning probe microscope. The acquired topographical data was processed using the WSxM software [58], applying a simple parabolic flattening and increased contrast to enhance the recorded features. The smoothness of the films was estimated employing root-mean-square (RMS) roughness analysis. The thin film displayed in figure 5.4 (a, b) are distinctly flat with an RMS of a) 1.03 nm and b) 1.51 nm, with pits included in the measurements. Excluding these features, the RMS roughnesses are that of a) 0.83 nm and b) 0.61 nm. Smooth film surfaces are a common feature for thin films grown by HiPIMS [59], and are normally desirable. The pits displayed at the sample surface are up to  $2 \mu\text{m}$  wide, and range from 1 nm - 10 nm in depth. Surface pits are a common feature in grown III-nitride films [60, 61, 62], and often attributed to dislocations. The pits displayed in figure 5.4 may therefore be a result of threading dislocations propagating through the crystal, acting as nucleation sites for growth in

different orientations. The growth rate in these alternative directions might be lower than that of the (0002) direction, causing pits. Further examinations of the pits have to be undertaken to conclude on the cause of this feature, however. There are no clear signs of columnar growth, a characteristic feature of sputtered III-nitrides [63, 64].

### 5.1.2 Electrical Properties of Stoichiometric Films

In order to optimize ZnSnN<sub>2</sub> for solar cell applications, control of the electrical properties of the material is imperative. If the carrier density is too high, typically  $>10^{19} \text{ cm}^{-3}$ , a potential *pn*-junction will not be feasible, as the resulting depletion region may probe almost exclusively the substrate. Hall effect measurements were undertaken on the stoichiometric series to work as a reference for future material explorations. The measurements were conducted using a magnetic field strength of  $\pm 1.02T$  measured at room temperature, and sample specific information such as thin film thickness was accounted for. The stoichiometric ZnSnN<sub>2</sub> samples had average carrier concentrations exceeding  $10^{20} \text{ cm}^{-3}$ , indicating a degenerate semiconductor.

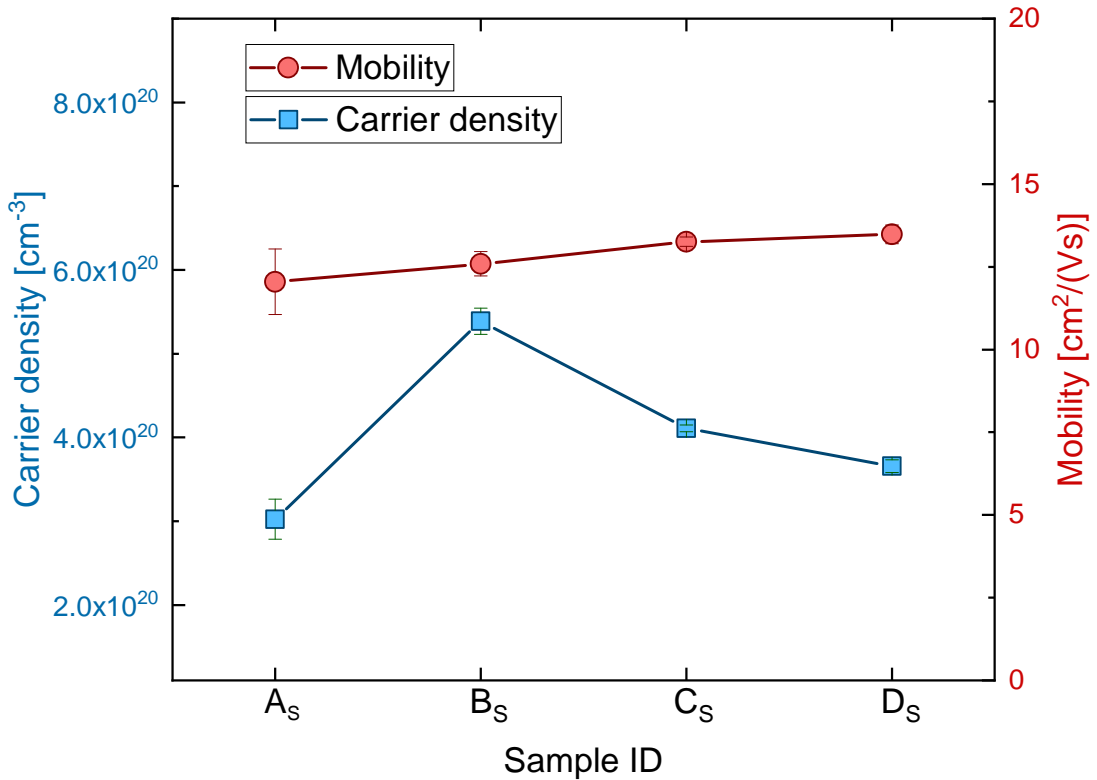


Figure 5.5: Plot of the carrier density and mobility at room temperature obtained through Hall effect measurement of the stoichiometric samples.

Their corresponding mobilities ranged from  $12.0 \text{ cm}^2/(\text{Vs})$  to  $13.5 \text{ cm}^2/(\text{Vs})$  and the resistivities from  $9.23 \times 10^{-4} \Omega\text{cm}$  to  $1.74 \times 10^{-3} \Omega\text{cm}$ , in good agreement with values previously reported for stoichiometric ZnSnN<sub>2</sub> [16, 65]. The electrical data for the four

stoichiometric samples are presented in figure 5.5, and they are reasonably uniform as expected for samples of similar growth conditions, and thus also cation ratios. The measured mobilities are relatively low compared to the electron mobility of  $38 \text{ cm}^2/(\text{Vs})$  in high quality  $\text{ZnSnN}_2$  grown on  $\text{ZnO}$  by Gogova *et al.* [15]. The dominating mobility limiting scattering effect in  $\text{ZnSnN}_2$  at room temperature, is predicted to be caused by neutral impurities, as reported by Hamilton *et al.* [66].

From the room temperature Hall effect measurements presented, it is evident that the stoichiometric  $\text{ZnSnN}_2$  thin films are not suitable for solar cell applications in their current state, with carrier densities exceeding  $10^{20} \text{ cm}^{-3}$ .

### 5.1.3 Optical Properties

The light absorbance of  $\text{ZnSnN}_2$  was investigated through UV-VIS transmittance and diffuse reflectance measurements performed by Dr. Galeckas. An estimate of the optical band gap of stoichiometric  $\text{ZnSnN}_2$  was made through Tauc plot analysis for direct allowed transitions of transmittance data, presented in figure 5.6 (a). Figure 5.6 (a) displays the absorption coefficient plotted for all measured photon energies, with an inset zoomed in around the absorption onset region of  $\text{ZnSnN}_2$ . Diffuse reflectance data analysed with the Kubelka-Munk method [67] is presented in (b). All of the measurements have additional base lines added for a more precise evaluation of the data [68], accounting for present Urbach tailing in the absorption onset of  $\text{ZnSnN}_2$  [41].

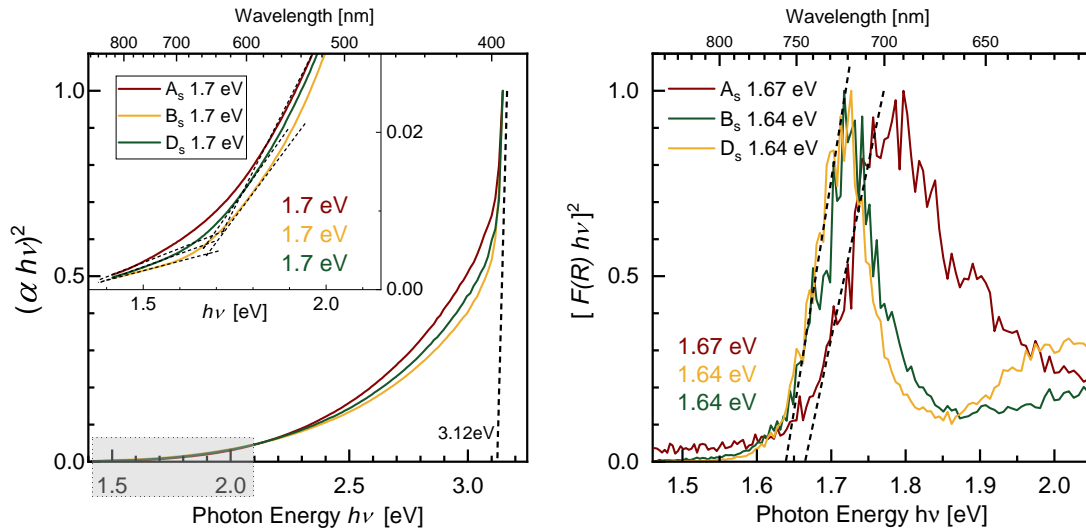


Figure 5.6: Direct allowed transitions evaluated through a) transmittance data displayed in a Tauc plot, with linear extrapolation of the linear Tauc-region. Inset displays the absorption onset of  $\text{ZnSnN}_2$ , with added baseline. b) Diffuse reflectance measurement, applying the Kubelka-Munk method. Adapted from Olsen *et al.* [14].

Three perforated lines display the linear extrapolation performed on the linear regions of the three graphs, all crossing the added base line close to 1.7 eV. The spectrum

displays a broad absorption tail of mixed nature between 2.1 eV - 3.0 eV, with contributions from N-implanted ZnO, the ZnSnN<sub>2</sub> epilayers and unspecified defects. The light transmitted through the sample has undergone interactions with both the ZnSnN<sub>2</sub> thin film as well as the ZnO substrate, which is in the order of 1000 times thicker than the thin film. Hence, the measured light will naturally have contributions from both. This is evident in figure 5.6 (a), where the absorption onset of ZnO is observable at 3.12 eV, whereas the absorption onset of ZnSnN<sub>2</sub> is fairly vague. The approximated absorption onset of ZnSnN<sub>2</sub> indicate  $E_g \sim 1.7$  eV for all measured samples. Due to the large influence of the N-implanted ZnO substrate, there are relatively large uncertainties related to the estimated band gap employing transmittance measurements. A way to reduce this uncertainty is to employ diffuse-reflectance measurements. Diffuse-reflectance measurement is the measurement of light which is reflected at an angle independent of the angle of incidence, i.e. reflected within the thin film. This excludes signals caused by specular reflection, allowing more precise measurement of the ZnSnN<sub>2</sub> thin film.

Diffuse-reflectance measurements, also performed by Dr. Galeckas, are presented in figure 5.6 b), displaying three graphs with associated linear extrapolations. The band gap estimate presented in figure 5.6 (b) can be seen to be in good agreement with the band gap estimates obtained from the transmittance data, thus reducing the uncertainty of the band gap estimates significantly. The estimated  $E_g$  might on the other hand be affected by the high carrier concentration measured by Hall effect (see fig 5.5) for the stoichiometric ZnSnN<sub>2</sub> series. For semiconductors with such high carrier concentrations, a blue shift of the absorption onset is expected, as a result of the Burstein-Moss effect [21, 22]. The high number of charge carriers in the conduction band will occupy states so that carriers in the valence band require additional energy  $>E_g$  to be excited. Thus, we expect that the fundamental band gap of stoichiometric ZnSnN<sub>2</sub> is lower than the estimated  $E_g$  of 1.6 - 1.7 eV. Reducing the carrier density should in principle reduce this blue shift, which can be measured through transmittance and reflectance data.

### Photoluminescence

Photoluminescence (PL) measurements were undertaken by Dr. Galeckas in a vacuum at 10 K and 300 K. An optical emission profile of the ZnSnN<sub>2</sub> was thus obtained, presented in figure 5.7. There is a considerable decrease in the measured intensity in the visible region of the electromagnetic spectrum, between 10 K and 300 K. However, the emission profile of ZnSnN<sub>2</sub> is relatively low compared to that of the ZnO substrate. The resulting emission profile is therefore heavily influenced by the substrate, and a majority of the measured intensity in the high photon energy region (3.5 - 2.5 eV) is most likely contributions from ZnO. This region has three distinct peaks at 300 K, accentuated by three fits in the figure. These peaks are possibly related to defects in the ZnO substrate. There is no significant near-band emission (NBE) apparent for ZnSnN<sub>2</sub> in figure 5.7. This may be attributed to the relatively high dislocation density of the films as evaluated through XRD measurements, common in III-nitrides [57]. Dislocations and other structural defects may serve as non-radiative recombination

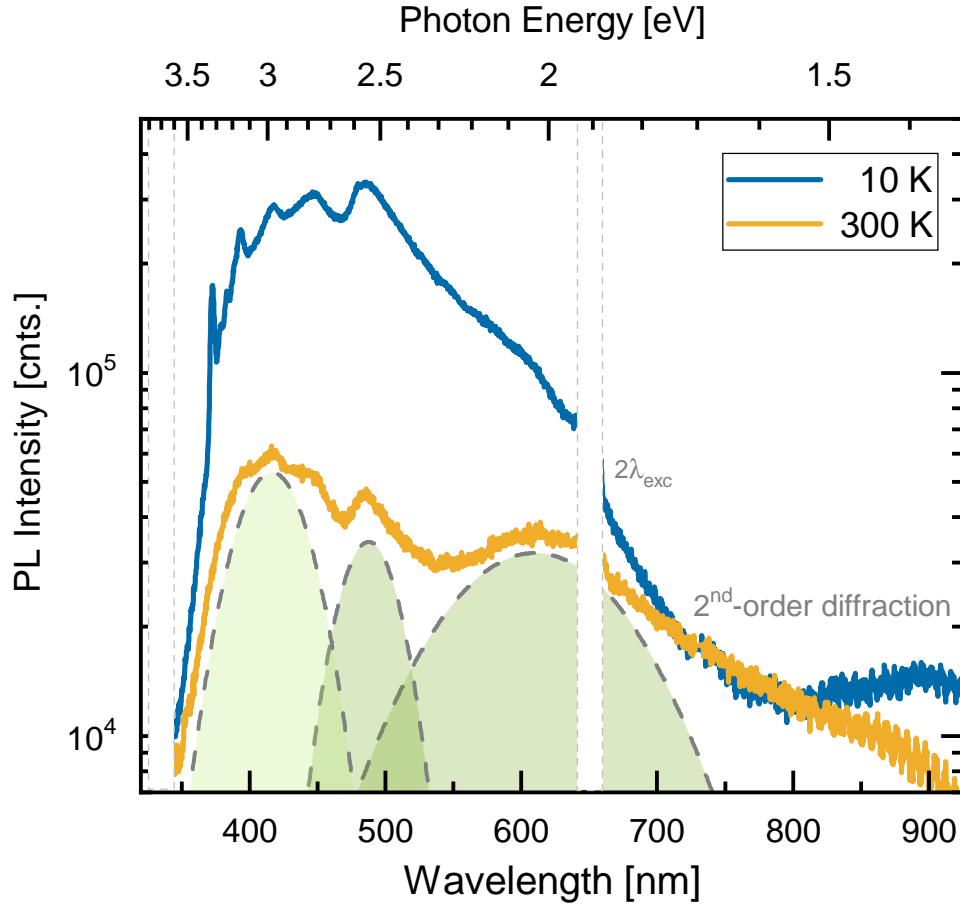


Figure 5.7: Photoluminescence emission spectra at 10 K and 300 K for sample  $B_s$ .  $2\lambda_{exc}$  marks an instrumental error excluded from the figure. Adapted from Olsen et al. [14].

centers in the material, thus reducing the total emission profile of the ZnSnN<sub>2</sub> thin films. Compositional ratios of Zn, Sn and N, as well as O<sub>N</sub> donors has been proven to affect the photoluminescence of ZnSnN<sub>2</sub>. One can thus tune the PL as a function of Zn, Sn, N and O content [69].

## 5.2 Off-Stoichiometric ZnSnN<sub>2</sub> Growth

The large carrier concentrations in the stoichiometric ZnSnN<sub>2</sub> thin films renders them possibly degenerate and unfit for solar cell applications. Thus, non-stoichiometric growth was investigated as an approach to reduce the carrier concentration. The Zn/(Zn+Sn) ratio of ZnSnN<sub>2</sub> has been predicted from theoretical calculations to affect the carrier concentration, as Zn<sub>Sn</sub> antisites are acceptors and Sn<sub>Zn</sub> antisites are double donors in ZnSnN<sub>2</sub> [16]. Shifting the cation ratio toward Zn-rich conditions has thus proven to be a viable route to suppress the carrier concentration down to  $2.7 \times 10^{17} \text{ cm}^{-3}$  [16, 44]. Even though non-degenerate ZnSnN<sub>2</sub> has been successfully grown, the

reported mobilities associated with these carrier concentrations are generally quite low,  $<10 \text{ cm}^2/(\text{Vs})$ . We therefore aimed to grow non-stoichiometric  $\text{ZnSnN}_2$  thin films of high crystal quality with reduced carrier concentrations and increased carrier mobilities. A series of non-stoichiometric  $\text{ZnSnN}_2$  films, and their deposition parameters are presented in table 4.1, with a denotation "NS". The non-stoichiometric samples has cation ratios  $\text{Zn}/(\text{Zn}+\text{Sn}) = 0.55, 0.66, 0.77$ .

Parallel to the strategy for reducing the carrier concentration by non-stoichiometric growth, the incorporation of impurities, such as O, was analysed. O is a common impurity in deposited nitrides, and  $\text{O}_N$  acts as a donor. The nitrogen gas purity was enhanced, as described in section 4.1, to reduce the incorporation of O in the  $\text{ZnSnN}_2$  films. A second non-stoichiometric series was deposited with a 50 nm thick  $\text{Si}_3\text{N}_4$  capping layer *in-situ* to prevent surface oxidation, denoted by "NS, cap". All of the presented samples were deposited on Si substrates for compositional analysis by SEM EDS as well as SIMS and thickness measurements. For structural, optical and electrical evaluation, P-implanted ZnO and *c*- $\text{Al}_2\text{O}_3$  was used as substrates. The capping layer complicated compositional analysis through SEM EDS. No deposition parameters were altered in the O-reducing measures however, and we assumed the composition of the films to be comparable to a series deposited prior to the O-reducing measures. Because the Zn-content increases within each series the non-stoichiometric samples are referred to as stoichiometric ( $A_{NS}$ ), Zn-rich ( $B_{NS}$ ), Zn-rich<sup>+</sup> ( $C_{NS}$ ) and Zn-rich<sup>++</sup> ( $D_{NS}$ ) throughout this section for a more descriptive notation of the samples. Likewise for the capped samples  $A_{NS,cap}$  (capped stoichiometric),  $B_{NS,cap}$  (capped Zn-rich),  $C_{NS,cap}$  (capped Zn-rich<sup>+</sup>).

### 5.2.1 Structural Analysis

Stoichiometric wurtzite  $\text{ZnSnN}_2$  was deposited epitaxially on N-implanted ZnO, and it was desirable to replicate these results for the non-stoichiometric samples in order to make a direct comparison between the series. All non-stoichiometric samples were investigated through XRD analysis, and both  $\theta/2\theta$ - and  $\omega$ -scans were employed.

The  $\theta/2\theta$  scans for the non-stoichiometric series are presented in figure 5.8. Sample  $B_{NS}$  displays a sharp peak identified as the  $\text{ZnSnN}_2$  (0002) reflection, indicating a uniform lattice plane spacing throughout the crystal. It is evident, however, that the crystal quality is compromised by the increasing Zn-content of the films, as both the intensity and peak-position of the (0002) reflection change. From sample  $B_{NS}$ , it is evident that by increasing the  $\text{Zn}/(\text{Zn}+\text{Sn})$  ratio even further, reduces the intensity of the (0002) reflection, while the peak position shifts towards lower  $2\theta$  angles. In addition, the  $D_{NS}$   $\theta/2\theta$  scan displays a reflection at  $\sim 97^\circ$ , a peak not associated with wurtzite  $\text{ZnSnN}_2$ . This peak has been cross-referenced with databases and is not related to metallic Zn or Sn, nor  $\text{Zn}_3\text{N}_2$  or  $\text{Sn}_3\text{N}_4$ . The peak could originate from the sample stage, but this is unlikely to be the case, however, as no previous  $\theta/2\theta$  scans have displayed this reflection. A high resolution  $\theta/2\theta$  scan around the two (0002) reflections of  $\text{ZnSnN}_2$  and ZnO, presented in figure 5.9 (a), reveals a shoulder at the ZnO (0002) reflection. The peak is located at  $34.26^\circ$ , and is seemingly unaffected by the increasing

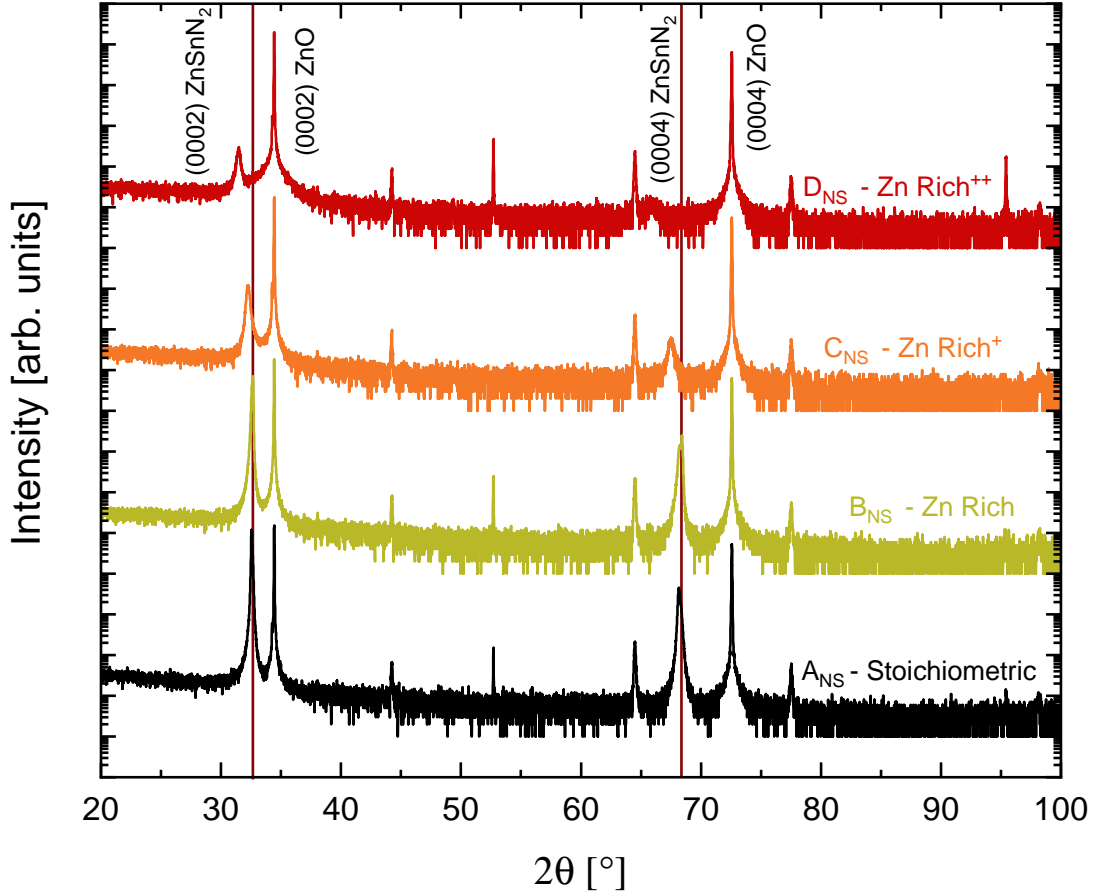


Figure 5.8:  $\theta/2\theta$ -scan of ZnSnN<sub>2</sub> with increasing Zn content, from stoichiometric ( $A_{NS}$ ), Zn-rich ( $B_{NS}$ ), Zn-rich<sup>+</sup> ( $C_{NS}$ ) and Zn-rich<sup>++</sup> ( $D_{NS}$ ). The (0002) and (0004) reflections of ZnSnN<sub>2</sub> are marked by lines at 32.65° and 68.35°, respectively.

Zn content. However, it is not present for sample  $B_{NS}$ . This peak may correspond to the (321) plane of body-centered cubic Zn<sub>3</sub>N<sub>2</sub>, which has a Bragg reflection peak at 34.28° [70, 71]. There are no clear indications of orthorhombic ZnSnN<sub>2</sub>, as this phase displays peaks at 30.65° (200), 32.61° (002) and 34.78° (201) [39]. No other reflections related to wurtzite ZnSnN<sub>2</sub> is apparent in figure 5.8.

For the evolution of the (0002) reflection when increasing the Zn-rich conditions, there are two evident trends of decreased intensities as well as an apparent shift towards lower values of  $2\theta$ . From figure 5.8 it is evident that both the (0002) and (0004) reflections are shifted towards lower  $2\theta$  values as the Zn/(Zn+Sn) ratio increase. Focusing on the (0002) reflection, Figure 5.9 (a) shows the  $\theta/2\theta$  scan in the range of 30.5°- 35.5°, the peak intensity of sample  $D_{NS}$  is three orders of magnitude lower than that obtained by the stoichiometric films, indicating a dramatic decrease in crystal quality. The reduced intensity implies that the increased Zn-content compromises the single crystalline properties we observed for stoichiometric ZnSnN<sub>2</sub> epilayers. The (0002) peak

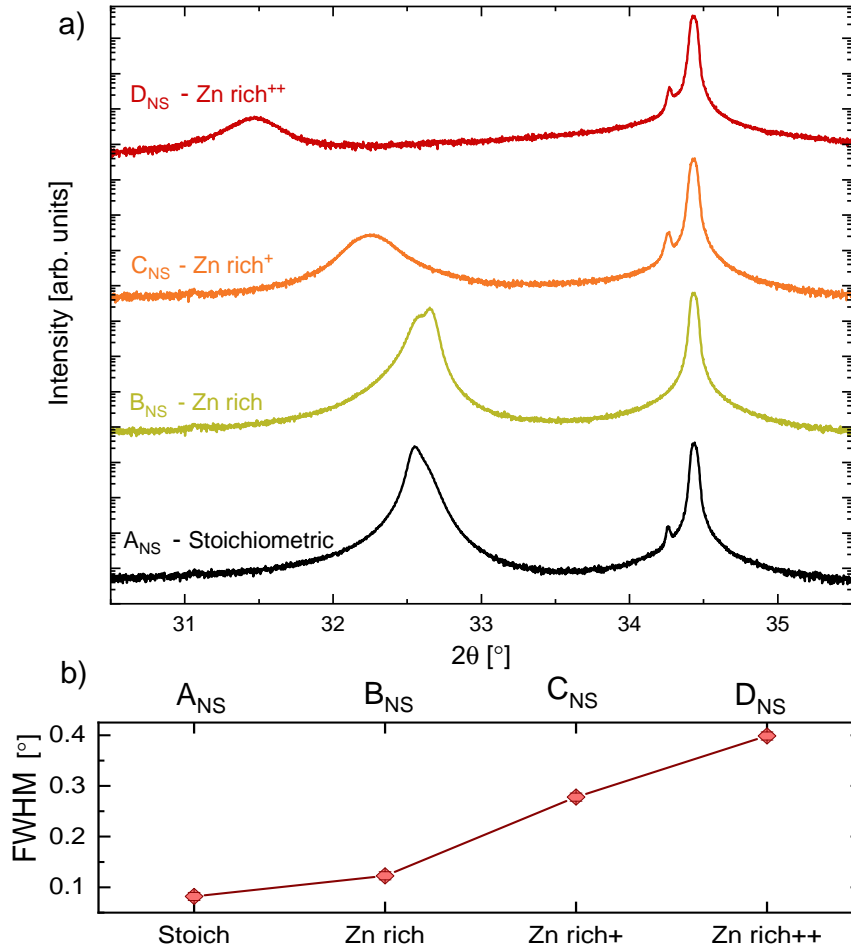


Figure 5.9: a)  $\theta/2\theta$  scan of non-stoichiometric series, ranging from  $30.5^\circ - 35.5^\circ$ . b) Evolution of calculated FWHM of the peaks located in the range  $31 - 33^\circ$ . An instrumental broadening of  $0.0008^\circ$  has been accounted for.

shift towards lower values of  $\theta/2\theta$  correspond to an increased average interatomic plane spacing, which may stem from tensile strain in the crystal, pushing the atomic planes apart. With peak positions of  $B_{NS} = 32.61^\circ$ ,  $C_{NS} = 32.26^\circ$  and  $D_{NS} = 31.46^\circ$ , the calculated lattice constants  $c$  are 0.548 nm, 0.555 nm and 0.568 nm, respectively. The significant shift in peak position for sample  $D_{NS}$  might also imply that this peak is not related to wurtzite  $ZnSnN_2$ .

Notably, the peak position of the stoichiometric sample  $A_{NS}$  has shifted towards higher values of  $2\theta$ , indicating a decreased lattice constant,  $c$ . Located at  $32.57^\circ$ , this sample has a lattice constant  $c = 0.549$  nm, 0.05 nm less than the calculated  $c$  of the stoichiometric series discussed in section 5.1. This might be a result of ion implantation of the ZnO substrate with P instead of N, but further investigation of the subject has to be made in order to conclude with this. The broadening of the peaks is evaluated by the FWHM, and is presented in figure 5.9 (b). The increased FWHM is an additional

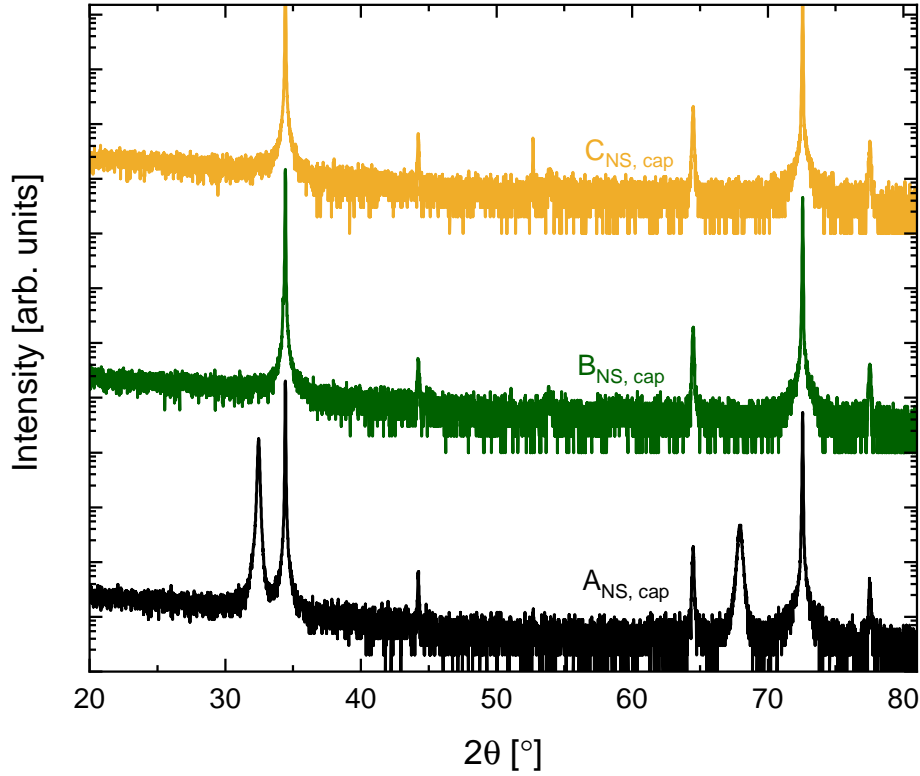


Figure 5.10:  $\theta/2\theta$  survey scan of the capped non-stoichiometric series.

indication of reduced crystal quality, thus our attempts at growth of highly crystalline wurtzite ZnSnN<sub>2</sub>, with reduced carrier concentrations caused by non-stoichiometry, were less successful than we aimed for.

The structural properties of the capped non-stoichiometric series were investigated through XRD measurements. A wide  $\theta/2\theta$  survey scan was conducted for the entire series, presented in figure 5.10. The stoichiometric sample displays a high intensity Bragg reflection at  $\theta/2\theta = 34.45^\circ$ , with a FWHM of  $0.13^\circ$ , related to the (0002) plane of wurtzite ZnSnN<sub>2</sub>. Besides the (0004) higher order multiple of the (0002) reflection, all other peaks can be related to the substrate or the sample stage. The high intensity of the (0002) peak confirms growth in the  $c$ -direction, although the reported intensity is significantly lower than those presented in figure 5.1. The FWHM may indicate that there are large disruptions in the interatomic spacing of the crystal. A  $\omega$ -scan (not shown here) was conducted in the (0002) reflection of sample A<sub>OR</sub>. The scan returned a broad peak of low intensity. If the material is polycrystalline, this might be indicative of crystallites oriented in different directions, i.e. not perpendicular to the substrate surface.

The  $\theta/2\theta$  scan for the non-stoichiometric samples with capping layer in figure 5.10 shows no sign of the wurtzite ZnSnN<sub>2</sub> (0002) Bragg reflection for the two non-stoichiometric samples. This is a further suggestion that an altered cation ratio disrupts the crystal

growth, resulting in reduced crystal quality. There are no signs of other phases present that are not related to the substrate or sample stage. It could be that high-quality Zn-rich  $\text{ZnSnN}_2$  require a higher substrate temperature, increasing the surface mobility. Further process development is required to investigate this behaviour.

### 5.2.2 Electrical Properties

Non-stoichiometric samples, i.e. Zn-rich  $\text{ZnSnN}_2$  were grown to fabricate non-degenerate  $\text{ZnSnN}_2$  thin films. The hypothesized increase of  $\text{Zn}_{\text{Sn}}$ - and reduction of  $\text{Sn}_{\text{Zn}}$ -antisites could in principle reduce the carrier density, as demonstrated by Fioretti *et al.* [16]. The electrical properties of the non-stoichiometric series were investigated through Hall effect measurements on P-implanted ZnO. Results of the aforementioned Hall measurements are presented in figure 5.11. Sample  $A_{\text{NS}}$  and  $B_{\text{NS}}$  both inhabit carrier densities  $> 10^{20} \text{cm}^{-3}$ , indicating degenerate state. However, a slight decrease in carrier concentration for the Zn-rich samples can be seen, with a carrier concentration in sample  $D_{\text{NS}}$  below  $3 \times 10^{19} \text{cm}^{-3}$ . Indeed, the carrier reducing effect of non-stoichiometry is more apparent as the Zn content increase. There is an obvious decrease in carrier density for sample  $C_{\text{NS}}$ .

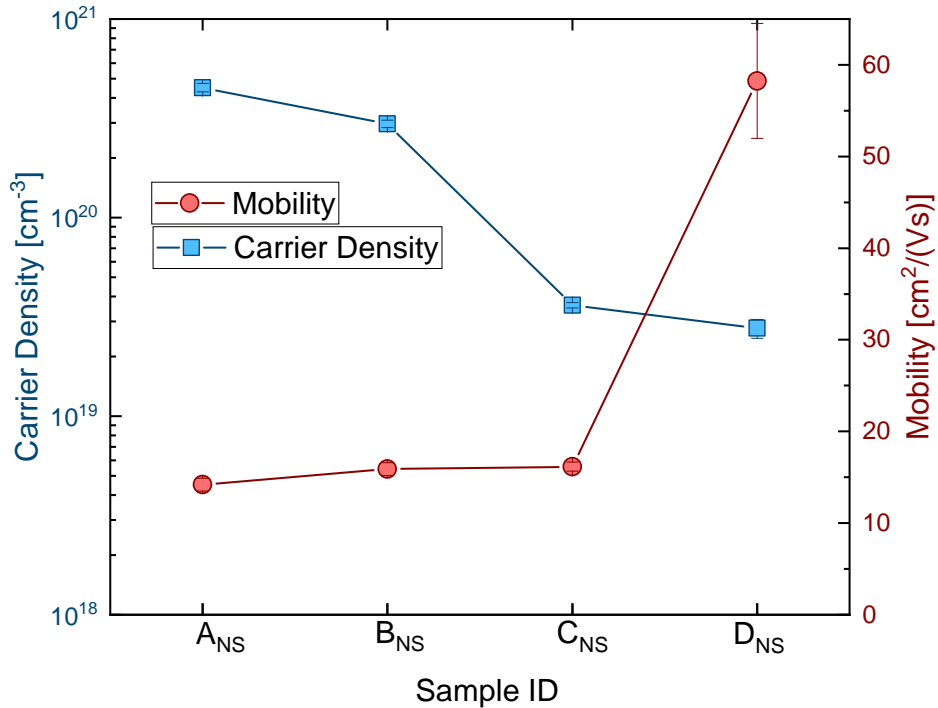


Figure 5.11: Plot of the carrier densities (blue squares) and mobilities (red circles) for the non-stoichiometric series as measured with Hall effect measurements.

After the significant reduction in carrier concentration from sample  $B_{\text{NS}}$  to  $C_{\text{NS}}$ , the evolution is more subtle when increasing the Zn-richness towards sample  $D_{\text{NS}}$ , with only a minor decrease. Due to the poor crystal quality of the non-stoichiometric

ZnSnN<sub>2</sub> films, it is difficult to make a direct comparison to the stoichiometric ZnSnN<sub>2</sub> epilayers presented in section 5.1.2. Whether the reduced carrier density is due to the off-stoichiometry of the films or structural changes, is grounds for further investigation, but taking into account the increasing Zn/(Zn+Sn) ratio, it indicates a reduction in Sn<sub>Zn</sub> antisites. Also presented in figure 5.11 is the measured carrier mobilities for the non-stoichiometric series. With mobilities in the range of 14 - 16 cm<sup>2</sup>/(Vs), samples A<sub>NS</sub>, B<sub>NS</sub> and C<sub>NS</sub>, although comparable to, still exceed those of stoichiometric wurtzite ZnSnN<sub>2</sub> presented in figure 5.5. Sample D<sub>NS</sub> is an outlier in this plot, with carrier mobility of 58.3 cm<sup>2</sup>/(Vs). This discrepancy could be an indication of a potential phase change due to the high Zn content of the sample, however, this has not been confirmed by XRD.

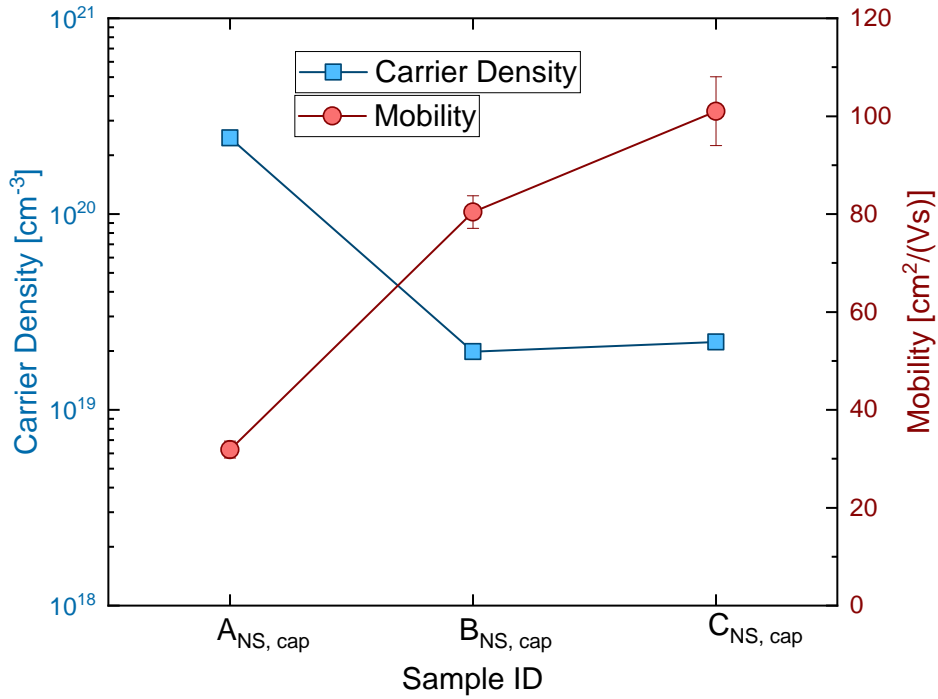


Figure 5.12: Plot of carrier density and carrier mobility of the capped non-stoichiometric series. Notice that the Zn content of the samples increase from left to right.

The capped non-stoichiometric series was also analysed with Hall effect measurements, both at room temperature and in a temperature range of 20 K - 300 K. The measured carrier densities and mobilities at room temperature are presented in figure 5.12. The capped stoichiometric film has a carrier concentration  $> 10^{20} \text{cm}^{-3}$ , and the two capped non-stoichiometric films have reduced carrier concentrations of  $\sim 1.7 \times 10^{19} \text{cm}^{-3}$ . The carrier mobilities range from  $\sim 35 \text{cm}^2/(\text{Vs})$  for the stoichiometric sample, to  $\sim 100 \text{cm}^2/(\text{Vs})$  for the Zn-rich<sup>+</sup> sample C<sub>NS, cap</sub>. Similar to the non-stoichiometric series, the crystal quality of these films are low, and a direct comparison between the series can not be made, but they display the same trend of reduced carrier concentration with

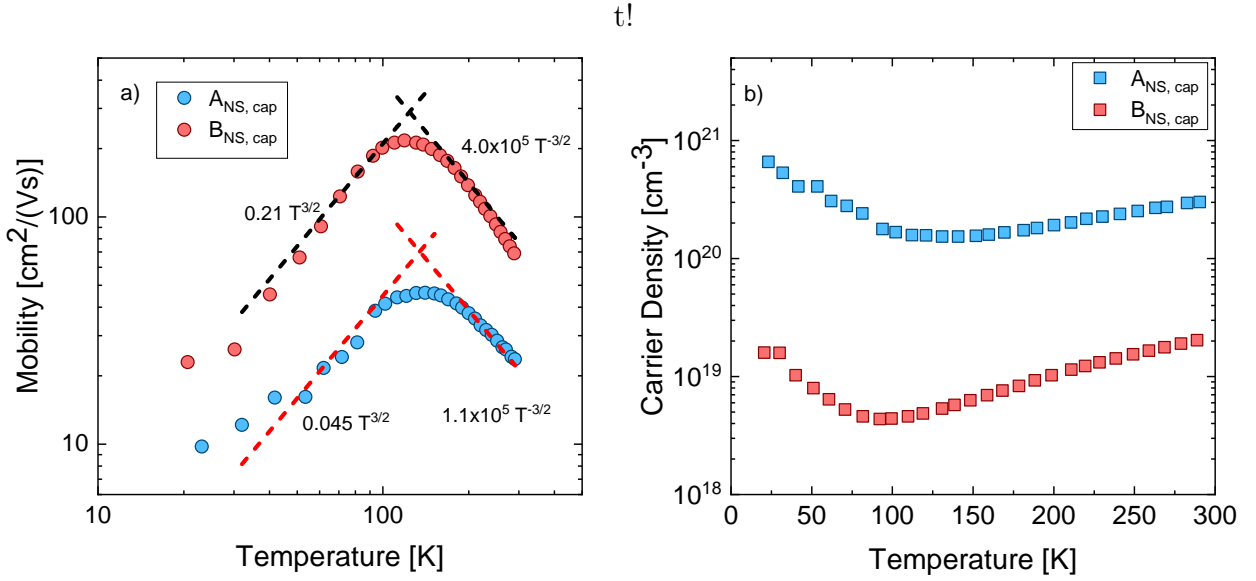


Figure 5.13: Temperature dependency of a) carrier mobility and b) carrier density in stoichiometric and Zn-rich films deposited with capping layer. The dashed lines in (a) illustrates the  $T^{\frac{3}{2}}$ - and  $T^{-\frac{3}{2}}$ -dependency in the low- and high-temperature domain, respectively.

increasing Zn-content, indicating that a reduction in  $\text{Sn}_{\text{Zn}}/\text{Zn}_{\text{Sn}}$  antisite ratio has been achieved.

The temperature-dependent Hall measurements (TdH) is presented in figure 5.13 (a, b). The two plots show the temperature dependence of (a) mobility and (b) carrier density in the range of 20 - 300 K. Interestingly, the carrier density of the stoichiometric film in the low temperature domain exceed the room temperature data. As the temperature increase, the carrier density decreases, a trend that continues to  $T \sim 120$  K. This behaviour is apparent for both the stoichiometric and non-stoichiometric films. The origin of this behaviour is not clear, although it has been observed in deposited III-nitrides as well, such as GaN grown by HVPE [72]. It is theorized that a degenerate layer forms at the GaN/substrate interface caused by high-density stacking faults due to lattice mismatch between the grown material and substrate, interfering with the measurements. As the temperature increases further, the carrier density starts to increase. This behaviour is expected, as more electrons are thermally excited to the conduction band at higher temperatures. The carrier mobilities for both the stoichiometric and non-stoichiometric samples exhibit classic semiconductor behaviour, although the peaks are slightly asymmetrical. In the low-temperature regions, mobility is limited by scattering between charge carriers and ionized impurities, with a temperature dependency  $\propto T^{\frac{3}{2}}$ , illustrated by dashed lines in the low-temperature region of figure 5.13 (a). As the temperature increase, the effect of ionized impurity scattering weans off, as the average thermal speeds of the carriers increase with temperature. Thus, the carriers spend less time in the vicinity of the ionized impurities, reducing the amount of scattering in the crystal. After a certain point, phonon scattering effects dominate, and the temperature-dependency of the mobility for higher temperatures is  $\propto T^{-\frac{3}{2}}$ ,

illustrated with dashed lines in the high-temperature region of figure 5.13 (a).

The asymmetry of the mobility is possibly related to the increase in carrier density at lower temperatures. As the mobility limiting factor in the low temperature domain is dominated by ionized impurities, the increase in carrier concentration may be a result of ionization events in the crystal. However, the asymmetry of the mobility plots are likely to be affected by additional mobility limiting events as well, such as electron-electron interactions and neutral impurities. The Zn-rich sample has a maximum carrier mobility of 216.76 cm<sup>2</sup>/(Vs) at 119 K, compared to a maximum 46.37 cm<sup>2</sup>/(Vs) at 140 K for the stoichiometric sample. Although comparable TdH measurements on ZnSnN<sub>2</sub> could not be found in the literature, mobilities above 70 cm<sup>2</sup>/(Vs) is in general considered exceptional for ZnSnN<sub>2</sub> thin films.

The electrical results indicate that the carrier density can be improved by non-stoichiometric growth. It is evident, however, that the carrier density is still far too high for any practical solar absorbing applications. This coupled with the fact that maintaining superior crystal quality is a challenge for non-stoichiometric ZnSnN<sub>2</sub> films, suggest that further optimization of the growth process is necessary to obtain the targeted electrical properties.

### 5.2.3 Optical Properties

UV-VIS photospectrometry was conducted on the non-stoichiometric ZnSnN<sub>2</sub> thin films deposited on P-implanted ZnO and *c*-Al<sub>2</sub>O<sub>3</sub> to measure the transmittance- and direct reflectance properties of the thin films. The resulting data was used to estimate the optical band gap of the material by Tauc analysis. The absorption coefficient ( $\alpha(h\nu)$ ) of the different thin films was plotted as a function of photon energy,  $h\nu$ , presented in figure 5.14. An extrapolation of the linear region in the graphs yields an estimate of  $E_g$ . The estimated band gaps are 1.9 eV, 1.5 eV and 1.4 eV for samples  $A_{NS, cap}$ ,  $B_{NS, cap}$  and  $C_{NS, cap}$ , respectively. In the context of reduced carrier concentration between the stoichiometric and non-stoichiometric films, an apparent redshift in absorption onset can be observed. This shift may be attributed to a reduced Burstein-Moss shift [21, 22], as the redshift corresponds well with reduced carrier concentrations obtained by Hall effect measurements. A change in crystal structure could also be the source of this trend, as we were unable to confirm the crystal structure of the non-stoichiometric samples through XRD analysis. The disruption of  $\sim 1.4$  eV is an instrumental feature caused by a change of source in the instrument.

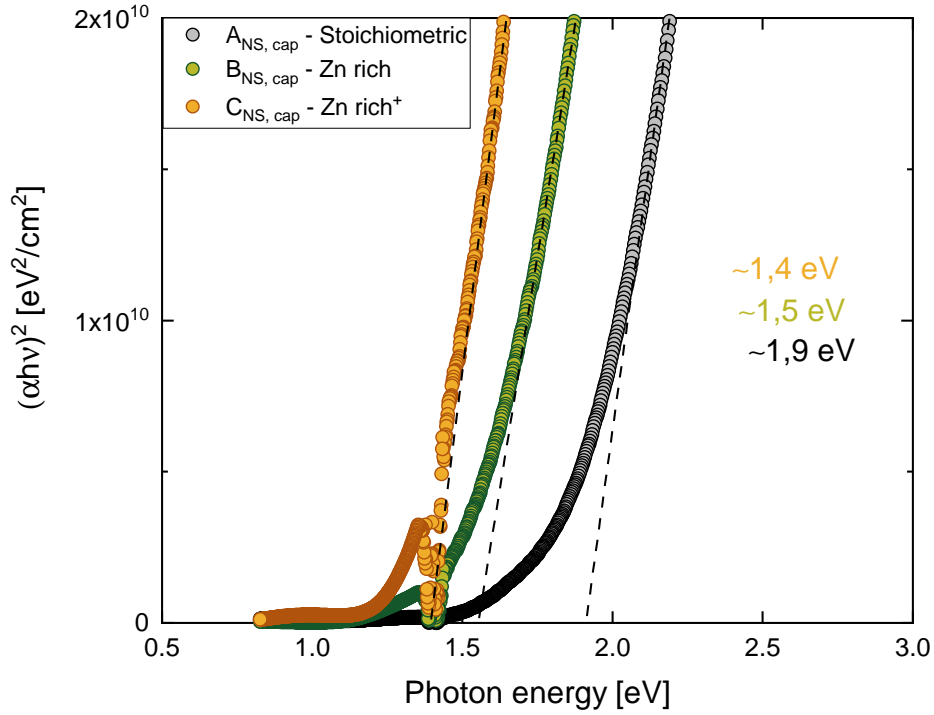


Figure 5.14: Tauc-plot of the measured transmittance and direct reflectance for capped non-stoichiometric  $\text{ZnSnN}_2$ . Notice how the shift towards lower  $E_g$  correspond with reduced carrier density.

### 5.3 Charge carrier control by Lithium Doping

The prevailing route for reduced carrier concentration in  $\text{ZnSnN}_2$  is non-stoichiometric growth, as discussed in section 5.2. Unintentional donor doping by O-incorporation during growth has also been discussed, see section 4.1. However, the measures taken to reduce this unintentional doping have not resulted in a significant reduction in carrier concentration. A conventional route for electrical control in semiconductors is doping. By doping  $\text{ZnSnN}_2$  with shallow acceptors, the acceptors may act as compensating defects, effectively reducing the charge carrier concentration. Li has been identified as a shallow acceptor in  $\text{ZnSnN}_2$  [18], and therefore, Li-doped  $\text{ZnSnN}_2$  thin films were deposited on Si, P-implanted ZnO and  $c\text{-Al}_2\text{O}_3$ . A Zn-target doped with 1 wt.%, that is  $\sim 8.69$  at.% Li, was employed in order to incorporate Li in the  $\text{ZnSnN}_2$  films during growth. All samples were deposited with a 6N nitrogen supply, the oxygen supply completely disconnected from the cluster system and a  $\text{Si}_3\text{N}_4$  capping layer deposited *in-situ*. A series similar to that presented in section 5.2 was deposited, creating a stoichiometric sample, and three samples of increasing Zn content. Because structural analysis by SEM EDS is complicated through the addition of a capping layer, a series was deposited on Si substrates without a capping layer, purely for compositional characterization. The subsequent films deposited with capping layers were assumed to be of similar stoichiometry.

## 5.3.1 SIMS

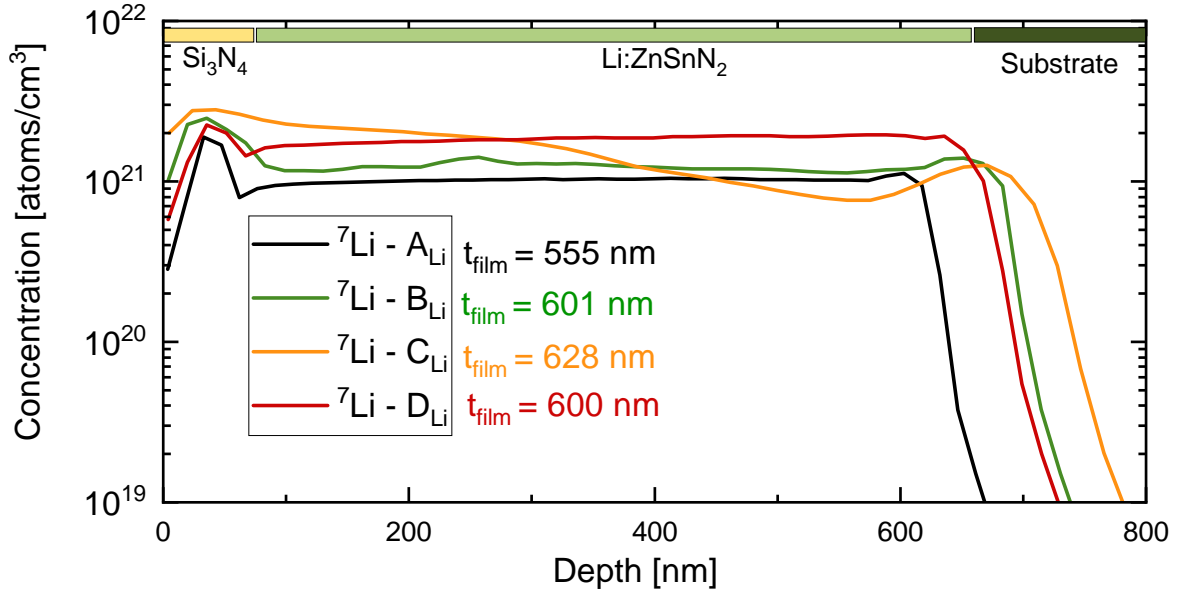


Figure 5.15: Plot displaying the Li concentration of samples  $A_{\text{Li}}$ ,  $B_{\text{Li}}$ ,  $C_{\text{Li}}$  and  $D_{\text{Li}}$  as a function of depth, obtained through SIMS measurements.

To evaluate whether or not Li was incorporated successfully in the  $\text{ZnSnN}_2$  thin films, SIMS measurements, conducted by Prof. Vines, were performed on the samples. SIMS depth profiles of  ${}^7\text{Li}$  are presented in figure 5.15. The variations in the Li signal up to  $\sim 50$  nm from the surface can be interpreted as the capping layer, while the Li-doped  $\text{ZnSnN}_2$  material can be identified as the plateau ranging from  $\sim 70$  nm outwards, and the substrate surface is therefore at the depth in which the signal decrease rapidly. This allows for a precise measurement of thin film thickness. The thin film thicknesses are denoted  $t_{\text{film}}$  in figure 5.15. A Li-implanted  $\text{ZnSnN}_2$  sample was used as a reference to convert the SIMS signal into absolute concentrations of Li. The Li-distribution profiles presented in figure 5.15 are fairly uniform throughout the thin films for all samples, except  $C_{\text{Li}}$ .  $C_{\text{Li}}$  has a gradually decreasing Li profile as a function of film depth, but the reason for this distribution is not clear. It could be due to instabilities of the plasma during depositions, but this is not confirmed. The Li content seems to increase slightly throughout the deposition series, with the stoichiometric sample,  $A_{\text{Li}}$ , displaying the lowest intensity, and  $D_{\text{Li}}$  the highest, which follows the Zn-content in the films, as expected.

## 5.3.2 Structural Analysis

The structural properties of the Li-doped  $\text{ZnSnN}_2$  thin films were investigated by XRD analysis. Thin films deposited on P-implanted ZnO substrates were investigated. A wide  $\theta/2\theta$  survey scan was conducted for all four samples of the series, presented in figure 5.16.

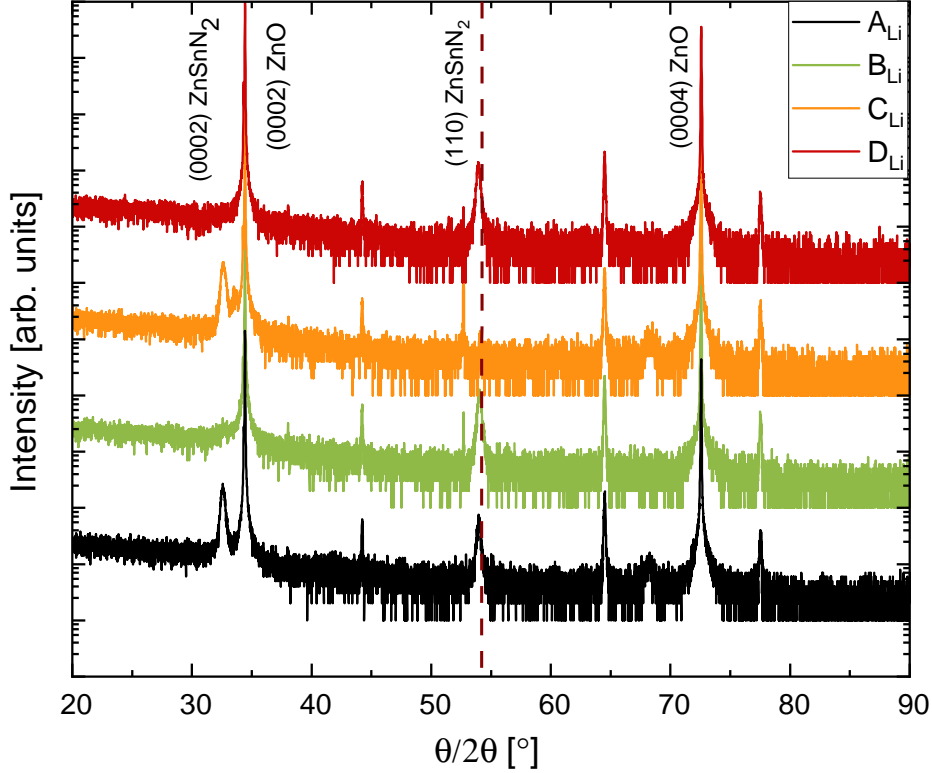


Figure 5.16:  $\theta/2\theta$  survey scan of the Li-doped series. The (110) Bragg reflection of wurtzite  $\text{ZnSnN}_2$  is marked with a dashed line.

The measured crystal quality is lower compared to the  $\text{ZnSnN}_2$  epilayers presented in section 5.1. In particular, samples  $A_{\text{Li}}$  and  $C_{\text{Li}}$  exhibit a Bragg reflection at  $\sim 32.6^\circ$ , which may be attributed to the (0002) plane of wurtzite  $\text{ZnSnN}_2$ . The signals are low in intensity, however, and are fairly broad with FWHM values of  $0.4^\circ$ , indicating low crystallinity. Sample  $C_{\text{Li}}$  exhibits a feature of  $\sim 33.4^\circ$ , apparent in a high resolution  $\theta/2\theta$  scan presented in figure A.1 found in appendix A, the origin of which is uncertain, as metallic Zn and Sn, nor  $\text{Zn}_3\text{N}_2$  or  $\text{Sn}_3\text{N}_4$  has any lattice planes corresponding to this reflection. The entire series displays an emerging shoulder on the (0002) reflection of the ZnO substrate, fairly consistent over the series at  $\sim 34.25^\circ$ . The  $\theta/2\theta$  survey scan reveals a Bragg reflection at  $\sim 54.0^\circ$ , for samples  $A_{\text{Li}}$ ,  $B_{\text{Li}}$  and  $D_{\text{Li}}$  possibly related to the (110) plane of wurtzite  $\text{ZnSnN}_2$ , situated at  $54.2^\circ$  [39]. Determination of this peak is difficult however, as both cubic  $\text{Sn}_3\text{N}_4$  and cubic  $\text{Zn}_3\text{N}_4$  has Bragg reflections in the vicinity of  $54^\circ$ , located at  $52.58^\circ$  and  $52.93^\circ$ , respectively [70], [71]. As this series is Zn-rich, the presence of  $\text{Sn}_3\text{N}_4$  seems unlikely. If this reflection is indeed related to the (110) plane of  $\text{ZnSnN}_2$ , this might imply that Li-incorporation causes a change in growth direction, a feature that should be explored further.

To summarise the  $\theta/2\theta$  scans of the Li-doped series; there are two reflections of interest, located at  $32.6^\circ$  and  $54.25^\circ$ , respectively. These reflections might imply that wurtzite  $\text{ZnSnN}_2$  and/or cubic  $\text{Zn}_3\text{N}_4$  is present in the films. Presently there is insufficient evi-

ence in order to conclude with growth of hexagonal wurtzite  $\text{ZnSnN}_2$  thin films. Even if wurtzite  $\text{ZnSnN}_2$  is present in the films, the low intensities and high FWHM of the reflections at  $32.6^\circ$  indicate poor crystal quality, and a direct comparison between this series and the stoichiometric  $\text{ZnSnN}_2$  epilayers presented in section 5.1 is not feasible.

### 5.3.3 Electrical Properties

The Li-doped series was grown in order to reduce the charge carrier concentration, thus electrical characterization of the  $\text{ZnSnN}_2$  is of particular interest. The introduction of shallow acceptors could potentially lower the carrier density to a suitable level for solar cell purposes [18]. Li-doped  $\text{ZnSnN}_2$  thin films deposited on  $c\text{-Al}_2\text{O}_3$  and P-implanted ZnO substrates were measured by both room temperature- and temperature dependent Hall effect. Temperature-dependent Hall effect measurements measure the temperature dependency of charge carriers in  $\text{ZnSnN}_2$ , and can therefore give indications of the effects of extrinsic defects within the energy range measured. The room temperature Hall measurements are presented in figure 5.17 (a, b).

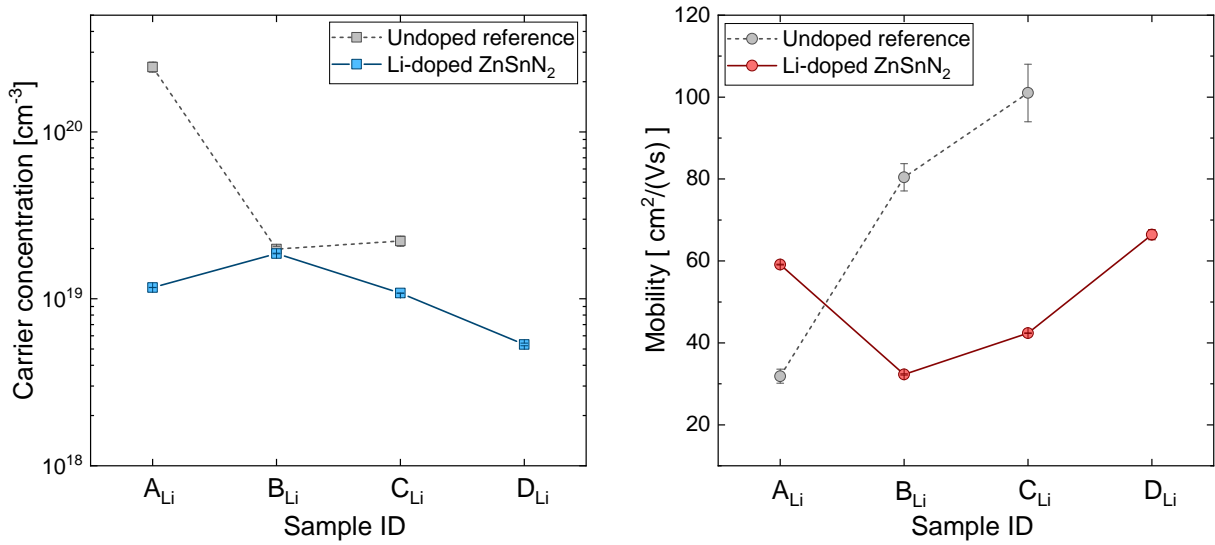


Figure 5.17: Results from room temperature Hall effect measurements displaying plots of a) carrier density and b) carrier mobility of the Li-doped  $\text{ZnSnN}_2$  films compared to undoped films of similar composition from the non-stoichiometric series discussed in section 5.2.

From figure 5.17, there is an evident reduction in carrier density for sample A<sub>Li</sub>, of  $1.16 \times 10^{19} \text{ cm}^{-3}$ , compared to an undoped reference, A<sub>NS,cap</sub>. Although a significant reduction in carrier concentration can be observed for the stoichiometric sample (A<sub>Li</sub>) compared to the reference sample, the effects of Li-doping do not follow the same trend as the undoped samples. There is an apparent decreasing trend throughout the series, however, with a slight decrease in carrier density for samples B<sub>Li</sub>, C<sub>Li</sub> and D<sub>Li</sub>. This relates well to the measured Li-concentrations presented in figure 5.15, but can also

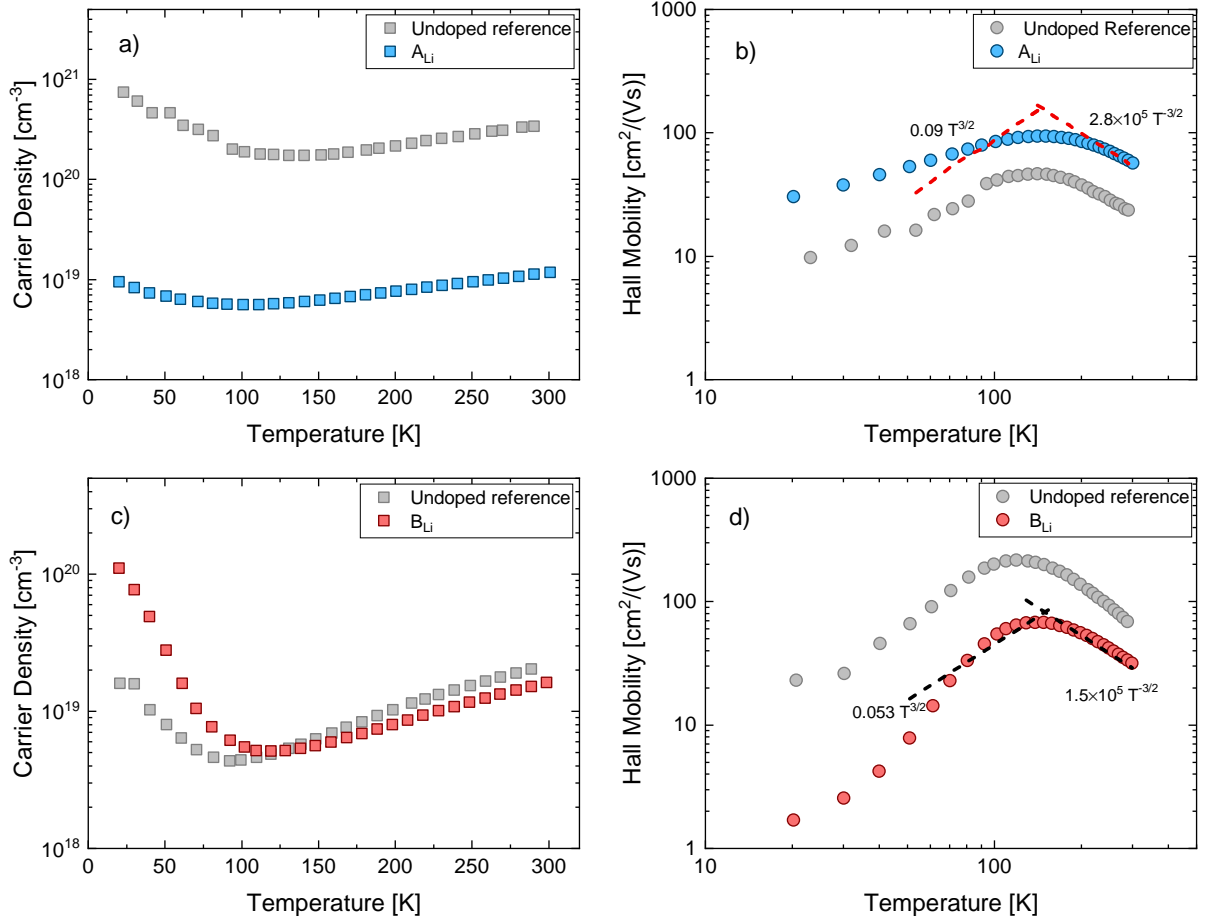


Figure 5.18: Temperature dependency of a) carrier density and b) carrier mobility in sample  $A_{Li}$  and c) carrier density and d) carrier mobility in sample  $B_{Li}$  compared with measurements of undoped reference samples. The dashed lines in the mobility plots are fits to illustrate the  $T^{\frac{3}{2}}$  and  $T^{-\frac{3}{2}}$  dependency of the low- and high-temperature domains, respectively.

be related to the increased Zn-content in the films, as discussed for the undoped non-stoichiometric samples. The mobilities measured at room temperature is presented in figure 5.17 (b). The mobility of sample  $A_{Li}$  is higher than the undoped reference sample. The mobility is reduced from sample  $A_{Li}$  to sample  $B_{Li}$ , a behaviour opposite of that displayed by the undoped films, which has an increasing trend in carrier mobility with increasing Zn content. This increasing trend is recognized in samples  $B_{Li}$ ,  $C_{Li}$  and  $D_{Li}$ , where the Zn content increase further.

To evaluate how the electrical properties of the Li-doped series vary with temperature, TdH measurements of the samples were conducted. A series of measurements were performed in a temperature range of 20 K - 300 K. The results of these measurements are presented in figure 5.18. Significant sample heating due to high resistivities prevented reliable TdH measurements for samples  $C_{Li}$  and  $D_{Li}$ . The carrier concentration profiles of the Li-doped samples are similar to the non-stoichiometric samples, presented in fig-

ure 5.13 (a) and (c), with a decreasing trend as the temperature increase. The decrease is most notable in sample  $B_{Li}$ , with a dramatic decrease in carrier concentration until  $T \sim 120$  K. As the temperature increase further the carrier concentration increase, as expected due to thermal excitation of electrons. Due to the implementation of Li, and thus possible  $Li_{Zn}$  acceptors, if on a substitutional Zn-site, a sudden drop in carrier density at a certain temperature could have been an indication of the activation energy of said defect. No such behaviour can be observed from figure 5.18. The carrier concentration of sample  $A_{Li}$  is one order of magnitude lower compared to its undoped reference sample. The carrier reducing effect of Li-doping is less evident for sample  $B_{Li}$ , compared to an undoped reference sample, as seen in figure 5.18 (c). The temperature-dependent mobility of sample  $A_{Li}$  is consistently higher and more symmetrical than its undoped reference. The temperature-dependent mobility of sample  $B_{Li}$  is consistently lower than its reference sample. As was the case for the non-stoichiometric samples, the temperature-dependent mobilities has a distinct asymmetry. This asymmetry is most pronounced for sample  $B_{Li}$ , further indicating a relationship with the high carrier concentration for low temperatures. The reduced mobility of  $B_{Li}$  compared to its undoped reference may be explained by an increase in ionized impurities caused by increased acceptor compensation. However, the increased mobility in  $A_{Li}$  can not be explained by the introduction of acceptors

### 5.3.4 Optical Properties

The introduction of Li, and possibly  $Li_{Zn}$  acceptors, has reduced the carrier concentration. The optical properties of the Li-doped series were thus evaluated through transmittance and direct reflectance measurement, utilizing UV-VIS spectrophotometry. The resulting data is presented as a Tauc plot in figure 5.19. The resulting graph shows a redshift in the absorption onset of  $ZnSnN_2$ , compared to the undoped reference samples, with sample  $C_{Li}$  as an outlier. The observed redshift may be explained by a reduced Burstein-Moss effect [21, 22], caused by the reduced carrier density. The discrepancy of  $C_{Li}$  might be attributed to the abnormal Li-distribution confirmed by SIMS measurements, presented in figure 5.15. The data presented in figure 5.19 is measurements done on P-implanted ZnO substrates. Measurements conducted on  $ZnSnN_2$  grown on  $c-Al_2O_3$  substrates (which can be found in appendix B) inhabits the same behaviour. Hence, faults in the experimental setup are unlikely to be the cause of this disagreement. Moreover, the shift cannot be explained by the Burstein-Moss effect as the carrier density of sample  $C_{Li}$  is comparable to the rest of the Li-doped samples. It might be explained by structural differences, however, as sample  $C_{Li}$  is the only sample in the Li-doped series that did not display a reflection at  $54^\circ$  in the  $\theta/2\theta$  scan in figure 5.16. This is purely speculative, and the cause of this feature remains uncertain.

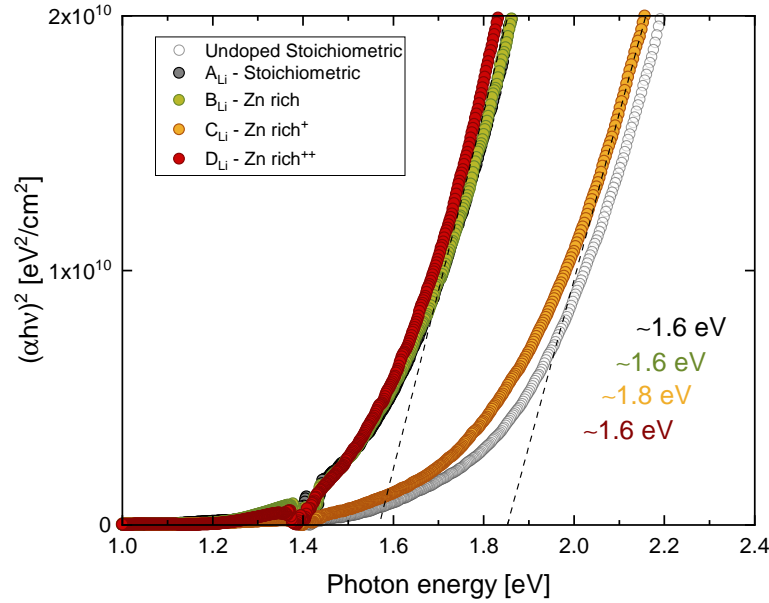


Figure 5.19: Tauc plot of Li-doped series deposited on P-implanted ZnO. Band gap estimates are based on linear extrapolation of the linear region of the absorption onset.

## Summary

From the presented results it is evident that stoichiometric wurtzite  $\text{ZnSnN}_2$  can be grown heteroepitaxially on ZnO substrates, which allows for possible implementation in existing III-nitride systems. However, measured carrier concentrations  $>10^{20}\text{cm}^{-3}$  for the stoichiometric samples imply that carrier reducing measures has to be taken for the material to be fit for solar cell applications. Non-stoichiometric growth, i.e. Zn-rich films, reduced the carrier concentrations to some extent. However, the crystal quality of the non-stoichiometric films was reduced significantly, hence a comparison between the non-stoichiometric and stoichiometric films are difficult. Li-doping of  $\text{ZnSnN}_2$  was successful, and reduced the carrier concentrations of the films. However, we were not able to reproduce the superior crystal quality of the stoichiometric series in the Li-doped samples. The results presented in this chapter indicate that  $\text{ZnSnN}_2$  may be suitable as a tandem cell material. There is a clear trend between reduced charge carrier concentration and estimated optical band gap, a feature that may be explained by a reduced Burstein-Moss effect.

# Chapter 6

## Conclusion

Stoichiometric ZnSnN<sub>2</sub> thin films were grown with a heteroepitaxial relationship to N-implanted (0002) ZnO substrates. Extensive XRD analysis including  $\theta/2\theta$ -,  $\omega$ - and  $\phi$ -scans were employed to investigate the structural properties of the samples.  $\theta/2\theta$  peak position implies an interplanar spacing of  $c = 0.554$  nm. Evaluation of  $\omega$  peak FWHM of the (0002) reflection was used to estimate the upper limit screw threading dislocation density,  $\rho_s = 1.9 \times 10^7$  cm<sup>-2</sup>.  $\phi$ -scans of the stoichiometric ZnSnN<sub>2</sub> films show a six-fold rotational symmetry in the crystal, confirming a wurtzite crystal structure. Topographical analysis of the sample surface through AFM revealed surface pits, a feature typical of nitride films. The optical properties of the ZnSnN<sub>2</sub> were investigated through transmittance and diffuse reflectance measurements. Tauc analysis and the Kubelka-Munk method yielded approximations of  $E_g \sim 1.6$  eV - 1.7 eV, respectively. Room temperature Hall effect measurements of the stoichiometric series confirmed carrier densities  $> 10^{20}$  cm<sup>-3</sup> for all samples, possibly related to O<sub>N</sub>- and Sn<sub>Zn</sub>- donor defects. The corresponding Hall mobilities lie in the range between  $\sim 12$  - 13 cm<sup>2</sup>/(Vs).

Two non-stoichiometric series were developed to lower the carrier concentration of the material by creating Zn-rich ZnSnN<sub>2</sub> films. One of the series was capped with a Si<sub>3</sub>N<sub>4</sub> layer *in-situ* to prevent surface oxidation, possibly lowering the formation of O<sub>N</sub>-donors. It is evident from XRD analysis, however, that the off-stoichiometry compromises the structural properties of the material, and wurtzite ZnSnN<sub>2</sub> could not be confirmed for any of the samples comprising this series. Room temperature Hall effect measurement of the non-capped samples implies a significant reduction in charge carriers caused by the increased Zn-content, ranging from  $3.5 \times 10^{20}$  cm<sup>-3</sup> for the stoichiometric film to  $1.7 \times 10^{19}$  cm<sup>-3</sup> for the Zn-rich films. Temperature dependent Hall effect measurements showed that the stoichiometric and Zn-rich samples have a decreasing trend in carrier density with increasing temperature. The carrier concentration increase again as the temperature goes above  $\sim 100$  K. The origin of this behaviour is unclear. The optical properties of the capped non-stoichiometric series yielded  $E_g$  estimates of 1.9 eV, 1.5 eV and 1.4 eV for the stoichiometric, Zn-rich and Zn-rich<sup>+</sup> samples, respectively. A probable origin of this redshift is the increased Zn-content and thus decreased carrier concentration, reducing the Burstein-Moss effect.

The third, and last series presented in this work, was deposited with a Li-doped Zn-target, resulting in Li-doped ZnSnN<sub>2</sub> thin films. SIMS data confirms a uniform Li-depth profile for all samples, increasing throughout the series. A Bragg reflection located at 54°, not apparent in any previous scans performed on ZnSnN<sub>2</sub>, was observed for samples A<sub>Li</sub>, B<sub>Li</sub> and C<sub>Li</sub>. This peak may correspond to the (110) plane of ZnSnN<sub>2</sub>, and could indicate a change in growth direction caused by the implementation of Li in ZnSnN<sub>2</sub>. A carrier reducing effect is evident in the Li doped ZnSnN<sub>2</sub>, with room temperature carrier concentration of  $1.16 \times 10^{19} \text{cm}^{-3}$  in the stoichiometric sample, compared to the undoped reference of  $3.4 \times 10^{20} \text{cm}^{-3}$ . The carrier density has a slight increase for the Zn-rich sample, a decreasing trend is apparent for the Zn-rich<sup>+</sup> and Zn-rich<sup>++</sup> samples, in good agreement with the Li-concentrations determined by SIMS measurements. The temperature dependence of the carrier density is similar to that observed in the non-stoichiometric series. The carrier density decrease as the temperature increase to  $T \sim 120$  K. From 120 K - 300 K, the carrier density increase steadily for both the stoichiometric and Zn-rich Li-doped samples. Temperature-dependent mobility plots display a behaviour similar to that observed in the non-stoichiometric series. The mobilities increase with increasing temperature, from 20 K - 150 K, where phonon scattering effects limit the mobility of the material. The mobility curve is asymmetrical, with a steeper increase in the low-temperature region. Estimated band gaps are 1.6 eV, 1.6 eV, 1.8 eV and 1.6 eV for the stoichiometric, Zn-rich, Zn-rich<sup>+</sup> and Zn-rich<sup>++</sup> samples, respectively. A shift in absorption onset compared to the stoichiometric series is evident, possibly related to an effective reduction in carrier concentration due to Li incorporation (for the stoichiometric sample) as well as increasing Zn-content (for the non-stoichiometric samples).

We have demonstrated that stoichiometric ZnSnN<sub>2</sub> can be grown with single crystalline quality by reactive co-sputtering employing HiPIMS and RF sputtering sources. Through non-stoichiometric growth and Li-doping, we have confirmed that the electrical and optical properties of the material can be controlled. Therefore, further material exploration should be conducted in order to optimize the material for solar cell applications.

## Suggestions for further work

This work has investigated the structural, electrical and optical properties of ZnSnN<sub>2</sub> thin films grown by reactive co-sputtering with HiPIMS and RF-sputtering sources in a nitrogen atmosphere. The material has been explored in the context of potential solar cell applications, specifically as a top cell material in a tandem solar cell configuration. A challenge of ZnSnN<sub>2</sub> in this regard, is the highly *n*-type nature of the native material, and reducing the carrier density further, while increasing the mobility should be a priority in further work.

---

As the non-stoichiometric films suffered from reduced crystal quality, a direct comparison to the single crystalline stoichiometric series was difficult. Further process development should be considered in order to investigate the native properties of non-stoichiometric wurtzite  $\text{ZnSnN}_2$  films.

This work has shown that the carrier concentrations of the  $\text{ZnSnN}_2$  thin films can be reduced through Li-doping. It is unclear, however, to what degree this reduction was caused by non-stoichiometry or the introduction of Li, as the  $\text{ZnSnN}_2$  was doped through the utilisation of a Li doped Zn-target employed at the HiPIMS. Thus, the Li concentration was directly related to the Zn-concentration, creating non-stoichiometric films in the doping process. The FLEXTURA cluster system allows for co-sputtering of 5 sources simultaneously, therefore it is possible to install a Li-doped Zn-target at a separate source while maintaining a pure Zn-target at the HiPIMS source. This allows for greater control of the Li concentrations in the finished films while maintaining a stoichiometric cation relationship.

Similarities in band gap and crystal structure between the III-nitride and Zn-IV-nitride semiconductors allows for a wide range of possible exploration of the two material groups [10]. A potential  $\text{ZnGe}_{1-x}\text{Sn}_x\text{N}_2$  alloy should be developed, and a possible band bowing effect as a function of Ge/Sn ratio should be explored. Similar studies on III-nitride alloys has been successful, i.e. Wu *et al.* grew wurtzite  $\text{In}_{1-x}\text{Ga}_x\text{N}$  through molecular beam epitaxy (MBE) and reported a band gap bowing between  $\sim 0.8$  eV and  $\sim 1.7$  eV, with  $x = 0.0 - 0.5$  [73].



# Appendices



# Appendix A

## Structural Analysis

This appendix includes XRD scans not presented in the final thesis.

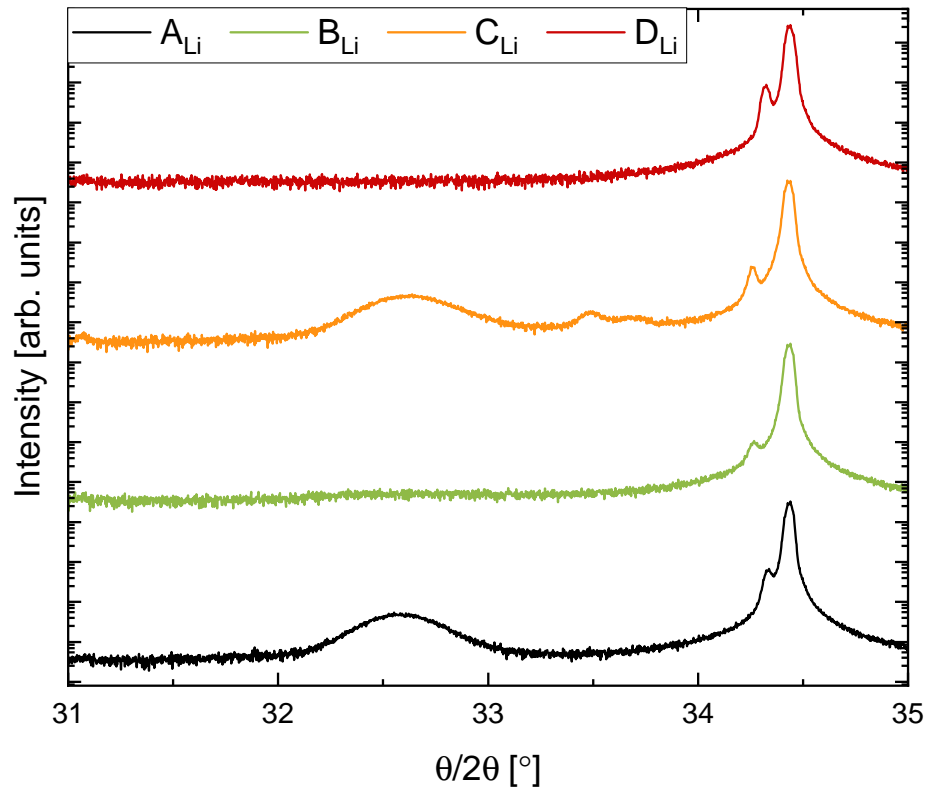


Figure A.1: High resolution  $\theta/2\theta$  around the (0002) Bragg reflections of hexagonal  $\text{ZnSnN}_2$  ZnO.

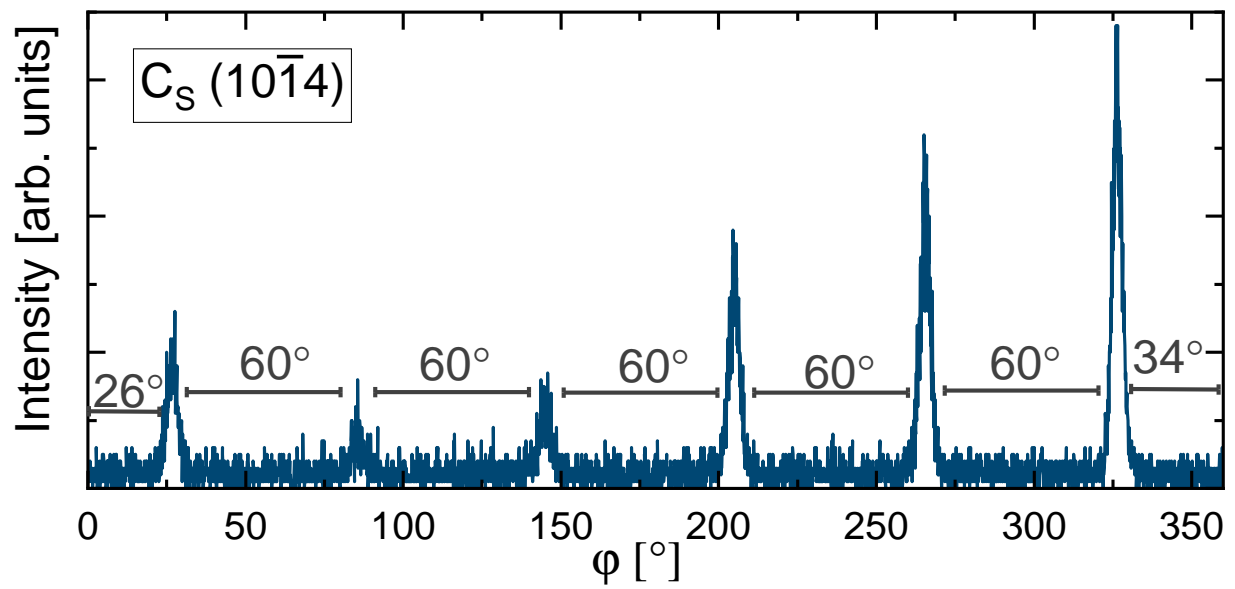


Figure A.2: Phi scan displaying six fold rotational symmetry of the  $(10\bar{1}4)$  reflection of wurtzite  $ZnSnN_2$ .

# Appendix B

## Optical Analysis

This appendix includes Tauc plots not presented in the final thesis.

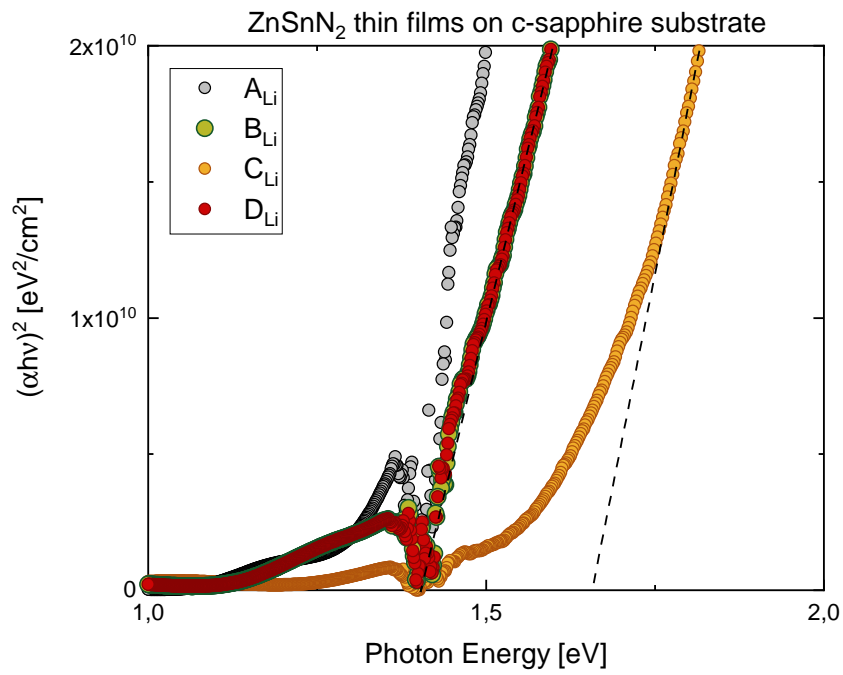


Figure B.1: Tauc plot of the Li-doped series deposited on *c*-Al<sub>2</sub>O<sub>3</sub>.



# Bibliography

- [1] P. Hemmer, *Faste stoffers fysikk*. Trondheim: Tapir, 1987.
- [2] C. Kittel, *Introduction to solid state physics*. Hoboken, N.J: Wiley, 8th ed. ed., 2005.
- [3] R. J. D. Tilley, *Understanding Solids: The Science of Materials*. Somerset: Wiley, 2. Aufl. ed., 2013.
- [4] D. J. Griffiths, *Introduction to quantum mechanics*. Cambridge: Cambridge University Press, 2nd ed. ed., 2017.
- [5] B. G. Streetman, *Solid state electronic devices*. Always learning, Boston, Mass: Pearson, 7th ed., global ed. ed., 2016.
- [6] S. A. Campbell, *Fabrication engineering at the micro- and nanoscale*. The Oxford series in electrical and computer engineering, New York: Oxford University Press, fourth edition. ed., 2013.
- [7] J. A. Venables, *Introduction to surface and thin film processes*. Cambridge: Cambridge University Press, 2000.
- [8] J. Nelson, *The physics of solar cells*. London: Imperial College Press, 2003.
- [9] S. Nakamura, T. Mukai, and M. Senoh, “Candela-class high-brightness InGaN/AlGaN double-heterostructure blue-light-emitting diodes,” *Applied Physics Letters*, vol. 64, no. 13, pp. 1687–1689, 1994.
- [10] P. C. Quayle, K. He, J. Shan, and K. Kash, “Synthesis, lattice structure, and band gap of ZnSnN<sub>2</sub>,” *MRS Communications*, vol. 3, no. 3, pp. 135–138, 2013.
- [11] L. Lahourcade, N. C. Coronel, K. T. Delaney, S. K. Shukla, N. A. Spaldin, and H. A. Atwater, “Structural and optoelectronic characterization of RF sputtered ZnSnN<sub>2</sub>,” *Advanced Materials*, vol. 25, no. 18, pp. 2562–2566, 2013.
- [12] N. Feldberg, J. D. Aldous, W. M. Linhart, L. J. Phillips, K. Durose, P. A. Stampe, R. J. Kennedy, D. O. Scanlon, G. Vardar, R. L. Field, T. Y. Jen, R. S. Goldman, T. D. Veal, and S. M. Durbin, “Growth, disorder, and physical properties of ZnSnN<sub>2</sub>,” *Applied Physics Letters*, vol. 103, no. 4, p. 042109, 2013.

- [13] D. D. Le, T. S. Ngo, J. H. Song, and S. K. Hong, "Epitaxial Growth of Bandgap Tunable ZnSnN<sub>2</sub> Films on (0001) Al<sub>2</sub>O<sub>3</sub> Substrates by Using a ZnO Buffer," *Cryst. Growth Des.*, vol. 18, pp. 1385–1393, 2018.
- [14] V. S. Olsen, V. Øversjøen, D. Gogova, B. Pécz, A. Galeckas, J. Borgersen, K. Karlsen, L. Vines, and A. Kuznetsov, "ZnSnN<sub>2</sub> in Real Space and k-Space: Lattice Constants, Dislocation Density, and Optical Band Gap," *Advanced Optical Materials*, DOI: <https://doi.org/10.1002/adom.202100015>, no. 2100015, 2021.
- [15] D. Gogova, V. S. Olsen, C. Bazioti, I.-H. Lee, O. y. Prytz, L. Vines, and A. Y. Kuznetsov, "High electron mobility single-crystalline ZnSnN<sub>2</sub> on ZnO (0001) substrates," *CrystEngComm*, vol. 22, no. 38, pp. 6268–6274, 2020.
- [16] A. Fioretti, A. Zakutayev, H. Moutinho, C. Melamed, A. Norman, M. Al-Jassim, E. Toberer, and A. Tamboli, "Combinatorial insights into doping control and transport properties of zinc tin nitride," *Journal of materials chemistry*, pp. 1–13, 04 2015.
- [17] S. Chen, P. Narang, H. A. Atwater, and L.-W. Wang, "Phase stability and defect physics of a ternary ZnSnN<sub>2</sub> semiconductor: First principles insights," *Advanced Materials*, vol. 26, no. 2, pp. 311–315, 2014.
- [18] N. Tsunoda, Y. Kumagai, A. Takahashi, and F. Oba, "Electrically Benign Defect Behaviour in Zinc Tin Nitride Revealed from First Principles," *Physical Review Applied*, vol. 10, p. 011001, 2018.
- [19] A. Punya, T. R. Paudel, and W. R. L. Lambrecht, "Electronic and lattice dynamical properties of II-IV-N<sub>2</sub> semiconductors," *physica status solidi c*, vol. 8, no. 7-8, pp. 2492–2499, 2011.
- [20] A. Punya, W. R. L. Lambrecht, and M. Van Schilfgaarde, "Quasiparticle band structure of Zn-IV-N<sub>2</sub> compounds," *Physical review. B, Condensed matter and materials physics*, vol. 84, no. 16, 2011.
- [21] E. Burstein, "Anomalous Optical Absorption Limit in InSb," *Physical review*, vol. 93, no. 3, pp. 632–633, 1954.
- [22] T. S. Moss, "The Interpretation of the Properties of Indium Antimonide," *Proceedings of the Physical Society. Section B*, vol. 67, pp. 775–782, oct 1954.
- [23] T. D. Veal, N. Feldberg, N. F. Quackenbush, W. M. Linhart, D. O. Scanlon, L. F. J. Piper, and S. M. Durbin, "Band gap dependence on cation disorder in ZnSnN<sub>2</sub> solar absorber," *Advanced Energy Materials*, vol. 5, no. 24, pp. 1–5, 2015.
- [24] P. C. Quayle, E. W. Blanton, A. Punya, G. T. Junno, K. He, L. Han, H. Zhao, J. Shan, W. R. L. Lambrecht, and K. Kash, "Charge-neutral disorder and polytypes in heterovalent wurtzite-based ternary semiconductors: The importance of the octet rule," *Physical review. B, Condensed matter and materials physics*, vol. 91, no. 20, 2015.

- [25] R. B. Heller, J. McGannon, and A. H. Weber, "Precision Determination of the Lattice Constants of Zinc Oxide," *Journal of Applied Physics*, vol. 21, no. 12, pp. 1283–1284, 1950.
- [26] L. Liu and J. Edgar, "Substrates for gallium nitride epitaxy," *Materials Science & Engineering R-reports - MAT SCI ENG R*, vol. 37, pp. 61–127, 04 2002.
- [27] M. Peters, J. C. Goldschmidt, P. Loeper, B. Gross, J. Upping, F. Dimroth, R. Wehrspohn, and B. Blasi, "Spectrally-Selective Photonic Structures for PV Applications," *Energies (Basel)*, vol. 3, no. 2, pp. 171–193, 2010.
- [28] D. Lundin, T. Minea, and J. T. Gudmundsson, *High Power Impulse Magnetron Sputtering : Fundamentals, Technologies, Challenges and Applications*. Elsevier, 2019.
- [29] J. I. Goldstein, *Scanning Electron Microscopy and X-Ray Microanalysis*. New York, NY: Springer New York : Imprint: Springer, 4th ed. 2018. ed., 2018.
- [30] B. Rogers, *Nanotechnology: understanding small systems*. Mechanical engineering series, Boca Raton, Fla: CRC, 3rd ed. ed., 2015.
- [31] G. Gilliland, "Photoluminescence spectroscopy of crystalline semiconductors," *Materials science & engineering. R, Reports : a review journal*, vol. 18, no. 3-6, pp. 99–354, 1997.
- [32] V. S. Olsen, *Functional properties and band gap engineering of ZnO-GaN alloys*. PhD thesis, University of Oslo, Oslo, 2020.
- [33] J. A. Thornton, "Influence of apparatus geometry and deposition conditions on the structure and topography of thick sputtered coatings," *Journal of vacuum science & technology*, vol. 11, no. 4, pp. 666–670, 1974.
- [34] D. Lundin and K. Sarakinos, "An introduction to thin film processing using High-power Impulse Magnetron Sputtering," *Journal of materials research*, vol. 27, no. 5, pp. 780–792, 2012.
- [35] K. Sarakinos and J. Alami and S. Konstantinidis, "High power pulsed magnetron sputtering: A review on scientific and engineering state of the art," *Surface and Coatings Technology*, vol. 204, no. 11, pp. 1661–1684, 2010.
- [36] C. Bazioti, V. S. Olsen, A. Y. Kuznetsov, L. Vines, and O. . Prytz, "Formation of N<sub>2</sub> bubbles along grain boundaries in (ZnO)<sub>1-x</sub>(GaN)<sub>x</sub>: nanoscale STEM-EELS studies," *Physical Chemistry Chemical Physics: PCCP*, vol. 22, no. 7, pp. 3779–3783, 2020.
- [37] T. Roychowdhury, D. Shah, V. Jain, D. I. Patel, B. Dodson, W. Skinner, J. N. Hilfiker, S. J. Smith, and M. R. Linford, "Multi-instrument characterization of HiPIMS and DC magnetron sputtered tungsten and copper films," *Surface and interface analysis*, vol. 52, no. 7, pp. 433–441, 2020.

- [38] M. Samuelsson, D. Lundin, J. Jensen, M. A. Raadu, J. T. Gudmundsson, and U. Helmerson, "On the film density using high power impulse magnetron sputtering," *Surface & coatings technology*, vol. 205, no. 2, pp. 591–596, 2010.
- [39] C. Xing-Min, W. Bo, Y. Fan, Z. Jun-Jie, V. Karthikeyan, W. Fan, M. Xiu-Fang, X. Yi-Zhu, Z. Dong-Ping, F. Ping, and R. V.A.L., "Fabricating ZnSnN<sub>2</sub> with co-sputtering," *Surface and Coatings Technology*, vol. 359, pp. 169–174, 2019.
- [40] B. D. Viezbicke, S. Patel, B. E. Davis, and D. P. Birnie, "Evaluation of the Tauc method for optical absorption edge determination: ZnO thin films as a model system: Tauc method for optical absorption edge determination," *Physica Ptatus Solidi (b)*, vol. 252, no. 8, pp. 1700–1710, 2015.
- [41] E. O. Kane, "Band tails in semiconductors," *Solid-state electronics*, vol. 28, no. 1-2, pp. 3–10, 1985.
- [42] J. K. Katahara and H. W. Hillhouse, "Quasi-fermi level splitting and sub-bandgap absorptivity from semiconductor photoluminescence," *Journal of applied physics*, vol. 116, no. 17, p. 173504, 2014.
- [43] F. T. Johra and W.-G. Jung, "Effect of light-ions implantation on resistivity of *gan* thin film," *Electronic materials letters*, vol. 10, no. 4, pp. 699–702, 2014.
- [44] Y. Wang, T. Ohsawa, X. Meng, F. Alnjiman, J.-F. Pierson, and N. Ohashi, "Suppressing the carrier concentration of zinc tin nitride thin films by excess zinc content and low temperature growth," *Applied Physics Letter*, vol. 115, 2019.
- [45] K. K. Chinnakutti, V. Panneerselvam, and S. T. Salammal, "Ba-acceptor doping in ZnSnN<sub>2</sub> by reactive RF magnetron sputtering; (002) faceted Ba-ZnSnN<sub>2</sub> films," *Journal of Alloys and Compounds*, vol. 855, 2021.
- [46] H. Morkoc, *Nitride semiconductor devices: fundamentals and applications*. Weinheim: Wiley-VCH, 2013.
- [47] A. M. Stoneham, "Non-radiative transitions in semiconductors," *Reports on progress in physics*, vol. 44, no. 12, pp. 1251–1295, 1981.
- [48] J. Iveland, L. Martinelli, J. Peretti, J. S. Speck, and C. Weisbuch, "Direct measurement of auger electrons emitted from a semiconductor light-emitting diode under electrical injection: Identification of the dominant mechanism for efficiency droop," *Phys. Rev. Lett.*, vol. 110, p. 177406, Apr 2013.
- [49] S. R. Kurtz, J. F. Klem, A. A. Allerman, R. M. Sieg, C. H. Seager, and E. D. Jones, "Minority carrier diffusion and defects in InGaAsN grown by molecular beam epitaxy," *Applied Physics Letters*, vol. 80, no. 8, pp. 1379–1381, 2002.
- [50] G. Coletti, D. Macdonald, and D. Yang, "Role of impurities in solar silicon," in *Advanced Silicon Materials for Photovoltaic Applications*, pp. 79–125, Chichester, UK: John Wiley & Sons, Ltd, 2012.

- [51] S. O. Kucheyev, J. S. Williams, C. Jagadish, J. Zou, C. Evans, A. J. Nelson, and A. V. Hamza, "Ion-beam-produced structural defects in ZnO," *Phys. Rev. B*, vol. 67, p. 094115, Mar 2003.
- [52] C. Romanitan, I. Mihalache, O. Tutunaru, and C. Pachiou, "Effect of the lattice mismatch on threading dislocations in heteroepitaxial GaN layers revealed by x-ray diffraction," *Journal of alloys and compounds*, vol. 858, p. 157723, 2021.
- [53] M. A. Moram, R. Oliver, M. J. Kappers, and C. J. Humphreys, "The spatial distribution of threading dislocations in gallium nitride films," *Advanced Materials*, vol. 21, no. 38-39, pp. 3941–3944, 2009.
- [54] C. G. Dunn and E. F. Kogh, "Comparison of dislocation densities of primary and secondary recrystallization grains of Si-Fe," *Acta metallurgica*, vol. 5, no. 10, pp. 548–554, 1957.
- [55] D. Gogova, D. Siche, A. Kwasniewski, M. Schmidbauer, R. Fornari, C. Hemmingsson, R. Yakimova, and B. Monemar, "HVPE GaN substrates: Growth and characterization," *Physica Status Solidi. C*, vol. 7, no. 7-8, pp. 1765–1759, 2010.
- [56] M. Moram and M. Vickers, "X-ray diffraction of III-nitrides," *Reports on Progress in Physics*, vol. 72, p. 036502, 03 2009.
- [57] M. Barchuk, M. Motylenko, G. Lukin, O. Patzold, and D. Rafaja, "Effect of screw threading dislocations and inverse domain boundaries in GaN on the shape of reciprocal-space maps," *Journal of applied crystallography*, vol. 50, no. 2, pp. 555–560, 2017.
- [58] I. Horcas, R. Fernandez, J. M. Gomez-Rodriguez, J. Colchero, J. Gomez-Herrero, and A. M. Baro, "WSxM: a software for scanning probe microscopy and a tool for nanotechnology," *Review of Scientific Instruments*, vol. 78, no. 1, pp. 013705–013705, 2007.
- [59] F. Lofaj, M. Kabatova, M. Klich, D. Vana, and J. Dobrovodsky, "The comparison of structure and properties in DC magnetron sputtered and HiPIMS W-C:H coatings with different hydrogen content," *Ceramics International*, vol. 45, no. 7, Part B, pp. 9502–9514, 2019. A selection of papers presented at CIMTEC 2018.
- [60] B. Heying, E. J. Tarsa, C. R. Elsass, P. Fini, S. P. DenBaars, and J. S. Speck, "Dislocation mediated surface morphology of GaN," *Journal of Applied Physics*, vol. 85, no. 9, pp. 6470–6476, 1999.
- [61] T. Hino, S. Tomiya, T. Miyajima, K. Yanashima, S. Hashimoto, and M. Ikeda, "Characterization of threading dislocations in GaN epitaxial layers," *Applied Physics Letters*, vol. 76, no. 23, pp. 3421–3423, 2000.
- [62] G. El-Zammar, W. Khalfaoui, T. Oheix, A. Yvon, E. Collard, F. Cayrel, and D. Alquier, "Surface state of GaN after rapid-thermal-annealing using AlN cap-layer," *Applied Surface Science*, vol. 355, pp. 1044–1050, 2015.

- [63] W. K. Hyoun and H. K. Nam, "Preparation of GaN films on ZnO buffer layers by RF magnetron sputtering," *Applied surface science*, vol. 236, no. 1-4, pp. 192–197, 2004.
- [64] L. Zhao, K. Yang, Y. Ai, L. Zhang, X. Niu, H. Lv, and Y. Zhang, "Crystal quality improvement of sputtered AlN film on sapphire substrate by high-temperature annealing," *Journal of materials science. Materials in electronics*, vol. 29, no. 16, pp. 13766–13773, 2018.
- [65] I. S. Khan, K. N. Heinselman, and A. Zakutayev, "Review of ZnSnN<sub>2</sub> semiconductor material," *Journal of Physics: Energy*, vol. 2, no. 3, p. 32007, 2020.
- [66] D. C. Hamilton, E. Arca, J. Pan, S. Siol, M. Young, S. Lany, and A. Zakutayev, "Electron scattering mechanisms in polycrystalline sputtered zinc tin oxynitride thin films," *Journal of applied physics*, vol. 126, no. 3, p. 35701, 2019.
- [67] P. Kubelka and F. Munk, "An article on optics of paint layers," *Z. Tech. Phys.*, vol. 12, no. 593, 1931.
- [68] P. Makula, M. Pacia, and W. Macyk, "How To Correctly Determine the Band Gap Energy of Modified Semiconductor Photocatalysts Based on UV-VIS Spectra," *The Journal of Physical Chemistry Letters*, vol. 9, pp. 6814–6817, 2018.
- [69] X.-M. Cai, B. Wang, F. Ye, K. Vaithinathan, J.-J. Zeng, D.-P. Zhang, P. Fan, and V. Roy, "Tuning the photoluminescence, conduction mechanism and scattering mechanism of ZnSnN<sub>2</sub>," *Journal of alloys and compounds*, vol. 779, pp. 237–243, 2019.
- [70] M. Z. Ansari, P. Janicek, D. K. Nandi, K. Palka, S. Slang, D. H. Kim, T. Cheon, and S.-H. Kim, "Influence of post-annealing on structural, optical and electrical properties of tin nitride thin films prepared by atomic layer deposition," *Applied Surface Science*, vol. 538, 2021.
- [71] F. Zong, H. Ma, W. Du, J. Ma, X. Zhang, H. Xiao, F. Ji, and C. Xue, "Optical band gap of zinc nitride films prepared on quartz substrates from a zinc nitride target by reactive rf magnetron sputtering," *Applied Surface Science*, vol. 252, no. 22, pp. 7983–7986, 2006.
- [72] D. C. Look and R. J. Molnar, "Degenerate layer at GaN/sapphire interface: Influence on Hall-effect measurements," *Applied Physics Letters*, vol. 70, no. 25, pp. 3377–3379, 1997.
- [73] J. Wu, W. Walukiewicz, K. M. Yu, J. W. Ager, E. E. Haller, H. Lu, and W. J. Schaff, "Small band gap bowing in In<sub>1-x</sub>Ga<sub>x</sub>N alloys," *Applied physics letters*, vol. 80, no. 25, pp. 4741–4743, 2002.